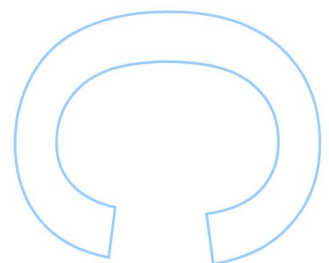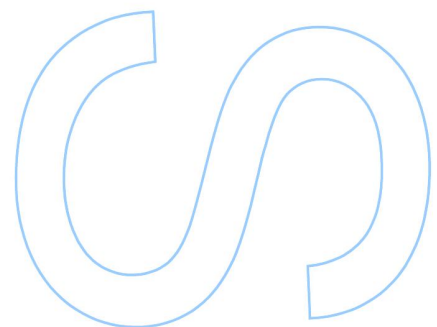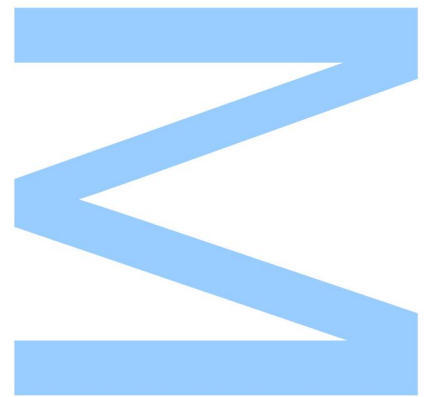# Search for top quarks accompanied by missing energy in hadronic topologies at the ATLAS experiment

José Ricardo Campos Cruz de Carvalho Correia
Mestrado em Física
Departamento de Física e Astronomia
2016

Orientador
Dr. Nuno Filipe da Silva Fernandes de Castro

U.PORTO
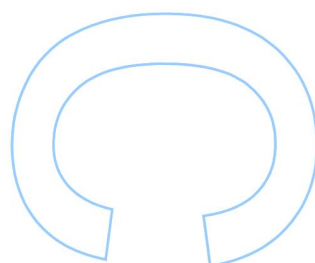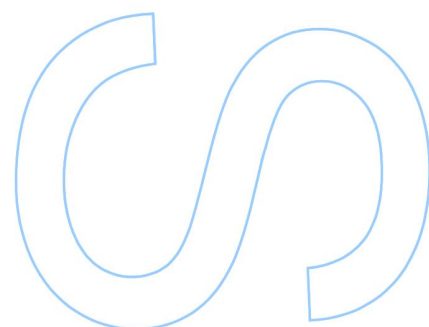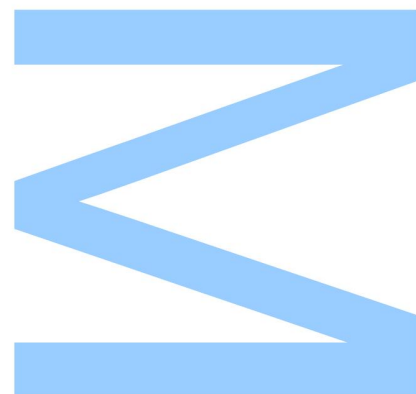
FC FACULDADE DE CIÊNCIAS
UNIVERSIDADE DO PORTO

Todas as correções determinadas pelo júri, e só essas, foram efetuadas.

O Presidente do Júri,

Porto, _____/_____/_____

"Fools rush in where angels fear to tread"

<div style="text-align: right;">

Alexander Pope, An Essay on Criticism

</div>

Acknowledgements

Abstract

The standard model of particle physics is one of the most successful frameworks in the entirety of physics, having correctly predicted the existence of several particles, such as the Higgs boson or the τ neutrino. However, despite its successes, it falls short of being a complete description of fundamental interactions, offering, for example, no explanation for dark matter phenomena or a solution to the hierarchy problem. A few models that address the shortcomings of the standard model, predict a heavy vector-like top quark, and a few others predict a massive scalar resonance, capable of decaying into invisible new fermions. Since these end up being kinematically similar, it is entirely possible to devise a search sensitive to both models (the one striking difference being the presence of at least one jet in the forward regions of the detector, for the heavy quark model).

In this thesis one presents a hunt to find these particles, by focusing on a vector-like top quark that decays into a highly boosted top quark (which will decay hadronically) and a Z boson (which further decays into a pair of neutrinos, invisible to the detector). In order to do so, one uses 2015 data (with a total integrated luminosity of 3.2 fb^{-1}) obtained at the ATLAS detector, one of the experiments of the record-breaking (highest centre-of-mass energy to date, ie. $\sqrt{s} = 13$ TeV) Large Hadron Collider.

Due to the similarities between the considered models, a signal region for vector-like top is devised alongside a signal region for the resonant model (in this case, without any forward jet requirement). In addition, a control region enriched in $t\bar{t}$ is described.

In order to delineate the aforementioned regions, limit setting is used. By doing so, we obtain a preliminary upper expected 95% C.L. exclusion limit on the cross-section of 0.45 pb without applying any forward jet requirement, and a limit of 0.32 pb when the forward demand cut is applied.

Resumo

O modelo padrão da física de partículas é uma das teorias mais bem sucedidas na história da física, tendo conseguido prever a existencia de várias particulas como o bosão de Higgs ou o neutrino tauónico. No entanto, não fornece uma descrição completa das interacções fundamentais, não oferecendo, por exemplo, nenhum candidato de matéria escura ou uma solução para o problema da heirarquia. Assim sendo, foram propostos diversos modelos que tentam remediar as falhas do modelo padrão, alguns dos quais prevêm a existência de um quark top pesado e vectorial, ou então a existência de uma resonância escalar que produz um fermião invisível. Uma vez que os dois casos anteriores são cinemáticamente semelhantes (à excepção da existência de pelo menos um jacto 'forward' no caso do quark vectorial), é inteiramente possível desenvolver uma pesquisa sensível aos dois modelos.

Nesta tese é descrito o ínicio de uma pesquisa por estas particulas, centrada no quark top vectorial, na qual o mesmo decay para um quark top de momento transverso elevado (que por sua vez decai hadronicamente) e para um bosão Z (que decai para um par de neutrinos, invisíveis ao detector). Para o fazer, foram utilizados dados obtidos em 2015 pela experiência ATLAS (dados esses com luminosidade total integrada de 3.2 fb^{-1}), um dos detectores do recordista "Large Hadron Collider" (maior energia de centro de massa até à data de $\sqrt{s} = 13$ TeV).

Devido às semelhanças existentes entre modelos, uma região de sinal para o modelo de quark vectorial é proposta, assim como uma região para o modelo resonante (neste segundo caso, sem requerimento nenhum em jactos 'forward'). Uma região de control rica em processos $t\bar{t}$ também é delineada.

Para ser possível delinear as regiões de sinal supra mencionadas, foi necessário calcular os limites superiores de exclusão de secção eficaz. Assim, obtém-se um limite de exclusão 95% C.L. de 0.45 pb sem aplicar nenhuma exigência no número de jactos 'forward', e um limite de exclusão de secção eficaz de 0.32 pb quando o requerimento de jactos 'forward' é aplicado.

Contents

List of Tables

List of Figures

List of abbreviations

ATLAS A Toroidal LHC ApparatuS

BSM Beyond the Standard Model

CERN European Origanization for Nuclear Research

CL Confidence Level

CMS Compact Muon Solenoid

CPT Central Trigger Processor

DONUT Direct Observation of the NU Tau

EM Electromagnetic

GRL Good runs list

HLT High-Level Trigger

IBL Insertable B-Layer

L1 Level-1 (Trigger)

LHC Large Hadron Collider

NPA New Physics Analysis

QCD Quantum ChromoDynamics

RoI Region of Interest

SCT Semi-Conductor Tracker

SM Standard Model

TRT Transition Radiation Tracker

VEV Vacuum Expected Value

VLQ Vector-Like Quark

WLCG Worldwide LHC Computing Grid

WP Working point

Chapter 1

Introduction

1.1 Current panorama of Particle Physics

Throughout the latter half of the 20th Century a series of experimental and theoretical breakthroughs have enabled the physics community to devise the standard model (SM) of particle physics. This framework attempts to describe and classify the interactions of the most fundamental constituents of nature. From a theory point-of-view, it is a self-consistent non-Abelian gauge symmetry based construct (more specifically a global Poincarè symmetry is assumed for all fields, and locally $SU(3)_c \times SU(2)_L \times U(1)_Y$ gauge symmetry). It can be divided into three sectors:

1. Electroweak sector, whose first description was brought forth in [1], based upon the $SU(2)_L \times U(1)_W$ gauge symmetry provides a unified description of the electromagnetic and the weak force. It can be described by the following Lagrangian, before symmetry breakage (and without the higgs terms, considered in the Higgs sector instead),

$$
\begin{aligned}
\mathcal{L}_{EW} &= i \sum_{\psi} \bar{\psi} \gamma^{\mu} D_{\mu} \psi - \frac{1}{4} \mathcal{W}_a^{\mu\nu} \mathcal{W}_{\mu\nu}^a - \frac{1}{4} \mathcal{B}^{\mu\nu} \mathcal{B}_{\mu\nu} \\
&= \sum_{\psi} \bar{\psi} \gamma^{\mu} (i\partial_{\mu} - g' \frac{1}{2} Y_W B_{\mu} - g \frac{1}{2} \vec{\sigma} \cdot \vec{W}_{\mu}) \psi - \frac{1}{4} \mathcal{W}_a^{\mu\nu} \mathcal{W}_{\mu\nu}^a - \frac{1}{4} \mathcal{B}^{\mu\nu} \mathcal{B}_{\mu\nu},
\end{aligned}
\tag{1.1}
$$

where σ are the Pauli matrices (generators of $SU(2)_L$ Lie algebra [1], whose eigenvalues correspond to weak isospin), γ_{μ} are the Dirac matrices, generators of the

---

[1] Meaning the Pauli matrices obey the following commutation and anticommutation relations,

$$
[\sigma_a, \sigma_b] = 2i\epsilon_{abc}\sigma_c; \quad \{\sigma_a, \sigma_b\} = 2\delta_{ab}I
\tag{1.2}
$$

FCUP | 19
Search for top quarks accompanied by missing energy in
hadronic topologies at the ATLAS experiment

Clifford algebra $\mathscr{C}_{1,3}$ (R)[2], D_μ is the covariant derivative associated with $SU(2) \times U(1)$, ψ correspond to fermionic fields, Y_W is the weak hypercharge (generator of $U(1)_W$), B_μ is the $U(1)_W$ gauge field, W_μ are $SU(2)_L$ gauge boson fields and g and g' are the electroweak copling constants, related to electronic charge, $|e|$, as $e = g\cos\theta_w = g'\sin w$, where θ_w is the weak mixing angle, $\mathcal{W}^a_{\mu\nu}$ and $\mathcal{B}_{\mu\nu}$ are the field strength tensors for weak isospin and weak hypercharge fields;

2. Quantum Chromodynamics Sector (QCD), responsible for explaining the interactions between quarks and gluons (strong force), uprooted by the $SU(3)_c$ symmetry, as envisioned by [2, 3, 4, 5] with the following Lagrangian

$$
\begin{aligned}
\mathcal{L}_{QCD} &= i\bar{u}D'_\mu\gamma^\mu u + i\bar{d}D'_\mu\gamma^\mu d + h.c. + \frac{1}{4}\mathcal{G}_a^{\mu\nu}\mathcal{G}^a_{\mu\nu} \\
&= i\bar{u}(\partial_\mu - ig_s G^a_\mu T^a)\gamma^\mu u + i\bar{d}(\partial_\mu - ig_s G^a_\mu T^a)\gamma^\mu d + h.c. + \frac{1}{4}\mathcal{G}_a^{\mu\nu}\mathcal{G}^a_{\mu\nu},
\end{aligned}
\tag{1.6}
$$

where D'_μ is the covariant derivative associated with $SU(3)$, u and d denote up and down type quarks, T_a are the generators of $SU(3)_c$'s Lie algebra, G^a_μ are the gluon fields, $\mathcal{G}^{\mu\nu}_a$ correspond to the gluon field strength tensor and g_s is the QCD coupling constant.

3. Higgs sector, proposed by [6, 7, 8] and incorporated in the Electroweak sector by [9], wherein the $SU(2)_L$ doublet Higgs field is defined by

$$
\phi = \begin{pmatrix} \phi^+ \\ \phi^0 \end{pmatrix} = \sqrt{\frac{1}{2}}\begin{pmatrix} \phi_1 + i\phi_2 \\ \phi_3 + i\phi_4 \end{pmatrix},
\tag{1.7}
$$

which, when evaluated in its vaccuum state, and as soon as a small fluctuation around this minima appears becomes

---

where ϵ is the Levi-Civitta symbol, δ is the Kroenecker delta and I is the identity matrix. The Pauli matrices are,

$$
\sigma_1 = \begin{pmatrix} 0 & 1 \\ 1 & 0 \end{pmatrix} \quad \sigma_2 = \begin{pmatrix} 0 & -i \\ i & 0 \end{pmatrix} \quad \sigma_3 = \begin{pmatrix} 1 & 0 \\ 0 & -1 \end{pmatrix}
\tag{1.3}
$$

[2]Meaning the γ matrices obey the following anti-commutation relation:

$$
\{\gamma^\mu, \gamma^\nu\} = -2\eta^{\mu\nu}I_4
\tag{1.4}
$$

and in the Weyl basis take the form,

$$
\gamma^0 = \begin{pmatrix} 0 & I_2 \\ I_2 & 0 \end{pmatrix} \quad \gamma^k = \begin{pmatrix} 0 & \sigma^k \\ -\sigma^k & 0 \end{pmatrix}
\tag{1.5}
$$

where σ^k are the Pauli matrices, and I_2 the 2×2 identity matrix.

$$\phi = \sqrt{\frac{1}{2}}\left[\begin{pmatrix} 0 \\ v \end{pmatrix} + \begin{pmatrix} 0 \\ h \end{pmatrix}\right], \tag{1.8}$$

where v is the vacuum expected value (VEV) of the scalar field and h a small perturbation. The VEV is related to parameters of the $V(\phi)$ potential: λ and μ ($\lambda > 0$ for a minimum to exist; $\mu^2 < 0$ after symmetry breaking, and $\mu^2 > 0$ before) by means of $v = (-\mu^2/2\lambda)^{1/2}$. The Lagrangian relevant to the Higgs Mechanism is given by

$$\mathcal{L}_{Higgs-EW} = (D_\mu\phi)^*(D_\mu\phi) - \mu^2\phi^\dagger\phi - \lambda(\phi^\dagger\phi)^2, \tag{1.9}$$

where the last two terms correspond to the potential $V(\phi)$, the first term describes the interaction between the Higgs and electroweak gauge bosons and the covariant derivative D_μ is associated with $SU(2)_L$. With the previous Lagrangian and the Higgs field behaviour described above, $W^\pm$ and Z bosons acquire mass. This result is a consequence of the Goldstone theorem[3]. The Higgs gives mass to fermions by means of Yukawa interactions, such as described by,

$$\mathcal{L}_{Higgs-fermions} = (\bar{u}_L\lambda_u u_R + \bar{d}_L\lambda_d d_R)\phi^0 + (\bar{u}_L\lambda_d d_R - d_L\lambda_u u_R)\phi^+ + h.c.. \tag{1.10}$$

The SM is thusly constitued by the following families of particles:

1. Leptons, spin-1/2 particles that do not interact by means of the strong force;

2. Quarks, spin-1/2 particles that undergo interactions with all fundamental forces;

3. Gauge Bosons, spin-1 particles that arise as quantized gauge fields;

4. Scalar Boson, the Higgs boson, a remnant of breaking electroweak symmetry spontaneously, i.e. it corresponds to the one degree of freedom that does not mix with any gauge boson after symmetry breaking.

SM representations of each gauge group under which spin-1, spin-0 and spin-1/2 fields can be found in tables 1.1 and 1.2.

The SM has been successful in correctly postulating the existence of several particles that were later observed experimentally, such as the top quark (1995, by the

---

[3]Goldstone Theorem [10]: it asserts that, by spontaneously breaking continuous symmetry, massless scalars degrees of freedom arise (aptly named Goldstone bosons). Their number is equal to the number of broken generators, as such, by going from $SU(3)_c \times SU(2)_L \times U(1)_W$ to $SU(3)_c \times U(1)_W$, three Goldstone bosons appear, which end up promoting (by way of mixing) massless gauge bosons to massive gauge bosons.

	G_μ	B_μ	W_μ	ϕ
$SU(3)_c$	8	1	1	1
$SU(2)_L$	1	1	3	2
$U(1)_Y$	0	0	0	1/2

Table 1.1: Representations of each SM gauge group under which spin-1 fields (G_μ, B_μ, W_μ), and spin-0 field (ϕ) transform.

	u_L, d_L	u_R	d_R	l_L, ν_L	l_R
$SU(3)_c$	3	3	3	1	1
$SU(2)_L$	2	1	1	2	1
$U(1)_Y$	1/6	2/3	-1/3	-1/2	-1

Table 1.2: Representations of each SM gauge group under which spin-1/2 fields transform.

Tevatron experiment at Fermilab [11, 12]), the tau neutrino (2000, DONUT experiment at Fermilab [13]), and, more recently, the Higgs boson (2012, at the ATLAS and CMS experiment at CERN's LHC [14]).

However, there are still phenomena currently unexplained by the SM, thus making it fall short of being a complete description of fundamental interactions. Examples of shortcomings of this paradigm, would include: failure to account for gravitation (the fourth fundamental force), not containing any explanation for the accelerated expansion of the Universe (i.e. no dark energy candidates), not providing any viable dark matter candidate and failure to explain the large discrepancy between the strength of the weak force and gravitation (hierarchy problem).

The hierarchy problem has another consequence. If the Higgs field VEV is not of the order of 246 GeV, both the $W^\pm$ and Z bosons could not have masses of the order of 80 and 90 GeV, respectively. And, if one adds the necessary corrections to the square of the Higgs mass, one would obtain a result of the order of 10^{18} GeV (Planck scale), a result of divergent terms associated with loop diagrams (see figure 1.1a)). This is in direct contradiction with the experimental observation. To evade this behaviour one would need some fine-tuning / almost-cancellation that would yield the correct mass. Or, theories Beyond the Standard Model (BSM), if experimentally verified, can provide the solution to this problem (for instance 1.1b)).

Another issue with the SM, would be the number of free parameters. Upon writing the full Lagrangian, one finds that the SM assumes at least 19 parameters (for example, quark and non-neutrino lepton masses, gauge couplings for the three SM gauge

FCUP | 22
Search for top quarks accompanied by missing energy in
hadronic topologies at the ATLAS experiment

groups, the VEV, the Higgs mass, quark mixing angles), whose values can only be experimentally constrained. Weather there is an underlying hidden symmetry, which explains these parameters, remains to be seen.
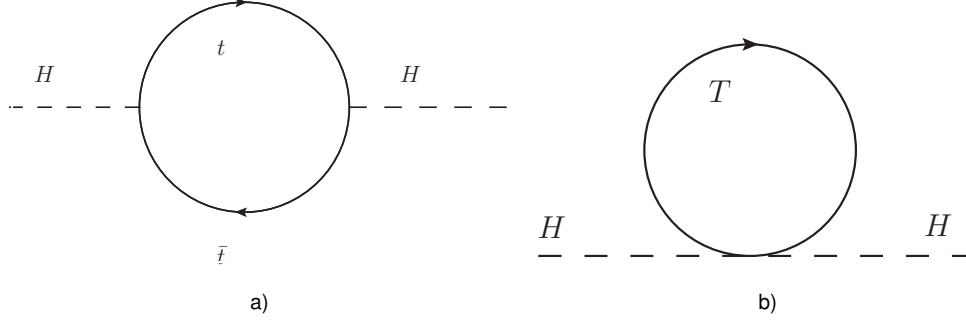
Figure 1.1: An example of a loop diagram that contributes to problematic corrections of the Higgs Mass a), and an example of a loop diagram where the introduction of particle originating from BSM models, T, helps cancel troublesome terms, in b). Note: all diagrams in this thesis were drawn with [15].

1.2 Vector-like quarks

Choosing a five-dimensional representation of the γ_μ Clifford Algebra, for it to be invariant under Lorentz group transformations, it is necessary to introduce a new "gamma" matrix. In essence one ends up with,

$$\gamma^5 = -i\gamma^0\gamma^1\gamma^2\gamma^3, \tag{1.11}$$

which allows for the definition of projection operators,

$$P_L = \frac{1}{2}(1 - \gamma_5); \ P_R = \frac{1}{2}(1 + \gamma_5), \tag{1.12}$$

that, when applied to a generic bi-spinor ψ, result in eigenstates with eigenvalues (chirality) +1 (Right-Handed) or -1 (Left-Handed), respectively,

$$\psi_L = \frac{1}{2}(1 - \gamma_5)\psi; \ \psi_R = \frac{1}{2}(1 + \gamma_5)\psi, \tag{1.13}$$

where $\psi = \psi_L + \psi_R$. If one looks at the usual SM quarks, one can see differing $SU(2)$ quantum numbers depending on whether we consider the right or the left-handed chirality. Since left-handed particles are doublets and right-handed ones are singlets, this essentially means they will couple differently to gauge fields, and this is translated in the fact that one can define only a one-handed charged current for SM Quarks,

$$\begin{aligned} j^\mu &= j_L^\mu + j_R^\mu \\ &= \bar{u}_L \gamma^\mu d_L + 0, \end{aligned} \tag{1.14}$$

This chiral nature also means, that a Dirac mass term is therefore not gauge invariant,

$$-m\bar{\psi}\psi = -m(\bar{\psi}_L\psi_R + \bar{\psi}_R\psi_L), \tag{1.15}$$

and, as such, a Yukawa coupling to the Higgs is necessary to bestow mass upon SM quarks.

Several new physics models predict the existence of chiral invariant (vector-like) heavy quarks (first delineated in [16], also present in [17, 18, 19, 20]). For vector-like quarks (VLQ), both Left and Right components have exactly the same weak isospin numbers (ie. transform the same way under $SU(2)$). As a consequence, one can now write a charged current with both left and right-handed components,

$$\begin{aligned} j^\mu &= j_L^\mu + j_R^\mu \\ &= \bar{u}_L \gamma^\mu d_L + \bar{u}_R \gamma^\mu d_R. \end{aligned} \tag{1.16}$$

As for the mass one doesn't require the Higgs anymore, a simple Dirac mass term suffices,

$$\mathcal{L}_M = -M\bar{\psi}\psi. \tag{1.17}$$

There are several theoretical models which predict VLQ's, such as composite Higgs models (where instead of having only an extended Higgs sector, heavier quarks appear as resonances of bound states [21, 22]), little Higgs variants (where partners of SM quarks appear from larger group representations [23, 24]), non-minimal supersymmetry [25], etc.

It would be inefficient to develop an experimental search for each of these models to look for VLQ's. Instead, one could establish an analysis based on an effective model, that encompassed common ground (in terms of final states, for instance) shared amongst all these models. An example of an effective Lagrangian (from [20]) would be:

$$
\begin{aligned}
\mathcal{L}_{VLQ} = k_T \Bigg\{ & \sqrt{\frac{\zeta_i \xi_W^T}{\Gamma_W}} \frac{g}{\sqrt{2}} [\bar{T}_{L/R} W_\mu^+ \gamma^\mu d_{L/R}^i] + \sqrt{\frac{\zeta_i \xi_Z^T}{\Gamma_Z}} \frac{g}{2c_W} [\bar{T}_{L/R} Z_\mu \gamma^\mu u_{L/R}^i] \\
& - \sqrt{\frac{\zeta_i \xi_H^T}{\Gamma_H}} \frac{M}{v} [\bar{T}_{L/R} H u_{L/R}^i] \Bigg\} \\
+ k_B \Bigg\{ & \sqrt{\frac{\zeta_i \xi_W^B}{\Gamma_W}} \frac{g}{\sqrt{2}} [\bar{B}_{L/R} W_\mu^- \gamma^\mu u_{L/R}^i] + \sqrt{\frac{\zeta_i \xi_Z^B}{\Gamma_Z}} \frac{g}{2c_W} [\bar{B}_{L/R} Z_\mu \gamma^\mu d_{L/R}^i] \\
& - \sqrt{\frac{\zeta_i \xi_H^B}{\Gamma_H}} \frac{M}{v} [\bar{B}_{L/R} H d_{L/R}^i] \Bigg\} \\
+ k_X \Bigg\{ & \sqrt{\frac{\zeta_i}{\Gamma_W}} \frac{g}{\sqrt{2}} [\bar{X}_{L/R} W_\mu^+ \gamma^\mu u_{L/R}^i] \Bigg\} + k_Y \Bigg\{ \sqrt{\frac{\zeta_i}{\Gamma_W}} \frac{g}{\sqrt{2}} [\bar{Y}_{L/R} W_\mu^- \gamma^\mu d_{L/R}^i] \Bigg\}.
\end{aligned}
\tag{1.18}
$$

Where four new vector-Like fermions are present, the T (with charge = +2/3), B (charge = -1/3), the X (charge = +5/3) and the Y (charge = -4/3), ζ's describe the couplings to standard model quarks, ξ 's to the vector and scalar bosons, and Γ''s are decay widths. There are several assumptions which uproot this effective model:

1. A SM Higgs is assumed: this effectively imposes mixing with standard quarks through Yukawa-type interactions involving a $SU(2)_L$ doublet, and in turn limits the number of vector-like multiplets one can have: 2 singlets, 3 doublets and 2 triplets. This essentially reads that custodial symmetry is upheld, as, even in models with Composite sector, one will still retain $\rho \approx 1$;

2. Mixing with SM quarks (as described in [17, 18]), also occurs through vector gauge bosons. In all cases this mixing is chiral: new singlets and triplets can mix with standard model left-handed doublets, while new doublets only mix with right-handed standard model quarks;

These considerations effectively restrict VLQ's to the multiplets presented in table 1.3.

	Singlets	Doublets	Triplets
	T, B	(X, T) (T, B) (B, Y)	(X, T, B) (T, B, Y)
$SU(3)_c$	3	3	3
$SU(2)_L$	1	2	3
$U(1)_Y$	2/3, -1/3	7/6, 1/6, -5/6	2/3, -1/3

Table 1.3: VLQ weak isospin multiplets and their possible representations.

An interesting consequence of mixing with SM quarks, is the natural appearance
of flavour changing neutral currents (FCNC), which are heavily surpressed in the SM
(Glashow-Illiapoulous-Maiani mechanism, presented on [26]), and provide for a rich
phenomenology to explore (ie. a myriad of open channels, if one considers both the
production and decay of these new quarks).

Singlet	Decay modes	Doublet	Decay modes
T	Ht , W^+b , tZ	(X, T)	W^+t , tZ , Ht
B	Hb , W^-t , Zb	(B, Y)	W^-b , Hb , Zb
X	W^+t	(T, B)	Ht , W^-t , tZ
Y	W^-b		

Table 1.4: VLQ decay isospin singlets and doublets, and possible decay modes under the assumption of the small
mixing approximation.

VLQ's can decay into an H, Z or W boson acompanied by a SM quark. Decays into
third generation quarks are preferred (due to naturalness driven arguments). Also, de-
pending on whether or not the VLQ we are considering is an isosinglet or an isodoublet,
this means some decay channels will be either surpressed or dominant. An example
would be the predominance of decay mode W^+b when considering a singlet T, however
non-existant if one considers a doublet (T B), as can be seen on table 1.4 and figure
1.2.

When it comes to production mechanisms, one can posit at least two for VLQ's,

1. Model independent pair-production, where a pair of VLQ's is produced via QCD
   (see figure 1.3);

2. Model dependent chiral single production, where a single VLQ is produced via
   electroweak interactions (see figure 1.4).

Another difference between these two production mechanisms: single-production is
expected to be dominant for higher VLQ masses, at $s = \sqrt{13}$ TeV, while for lower
masses, the opposite happens. This is evident by looking at production cross-section
for each mechanism across a range of masses (figure 1.5).

The purpose of this Thesis is to search for a singly produced vector-like top partner
(T), that specifically decays into a top and Z boson ($T \rightarrow Zt$) while targeting the final
state where the top decays hadronically (results in a boosted top topology), and the Z
decays to a pair of neutrinos (large amounts of $\not{E}_T$). The reasoning for choosing this
final state is as follows: even though it has the second largest relative Branching Ratio
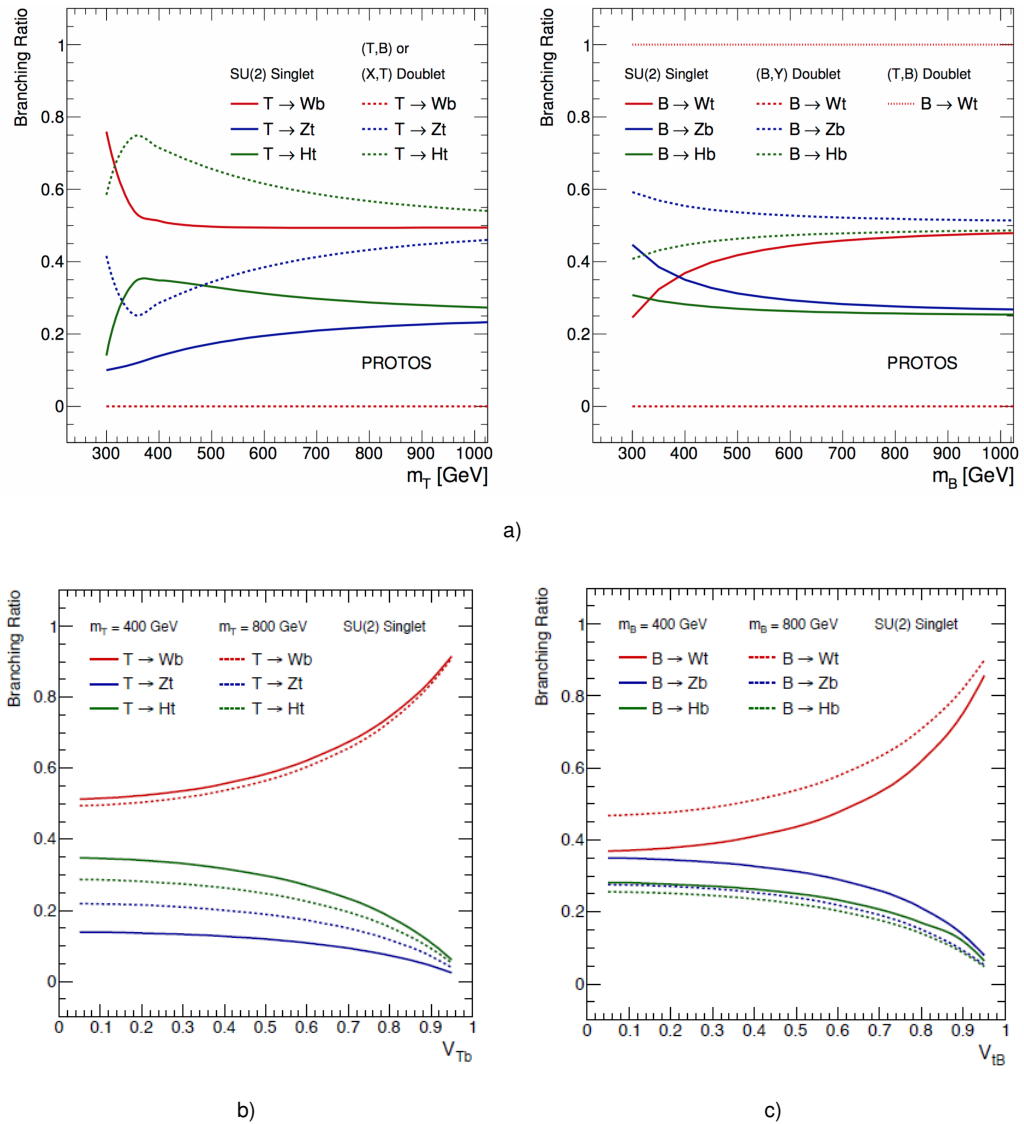
Figure 1.2: Branching ratios in the small mixing approximation (for small values of couplings to SM quarks, branching ratios remain constant for a given VLQ mass; this approximation is no longer valid for high coupling values, as BR exhibit a dependence on the couplings themselves[27]) of T quarks at the left-hand side pane of a) and of vector-like B (B) at right-hand side pane of a), for different mass hypothesis. Below, the two plots that justify the small mixing approximation, at b) and c). All were generated using PROTOS [28]. The upper panes were taken from [29],and the lower ones from [27].
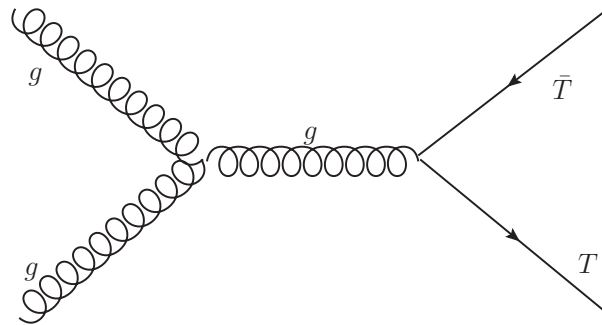
Figure 1.3: Feynman diagram of s-channel pair production of vector-like top (T) partners;
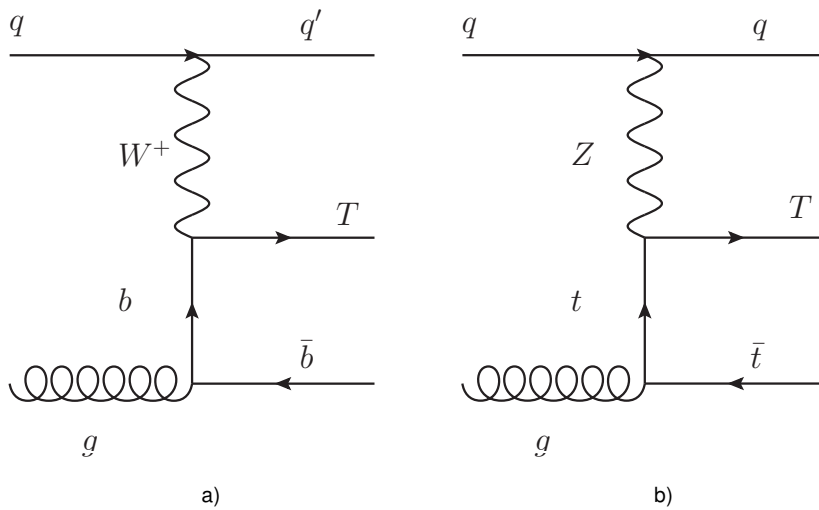
Figure 1.4: t-channel single production through either the vertex with W^+, a) or with Z boson, b).
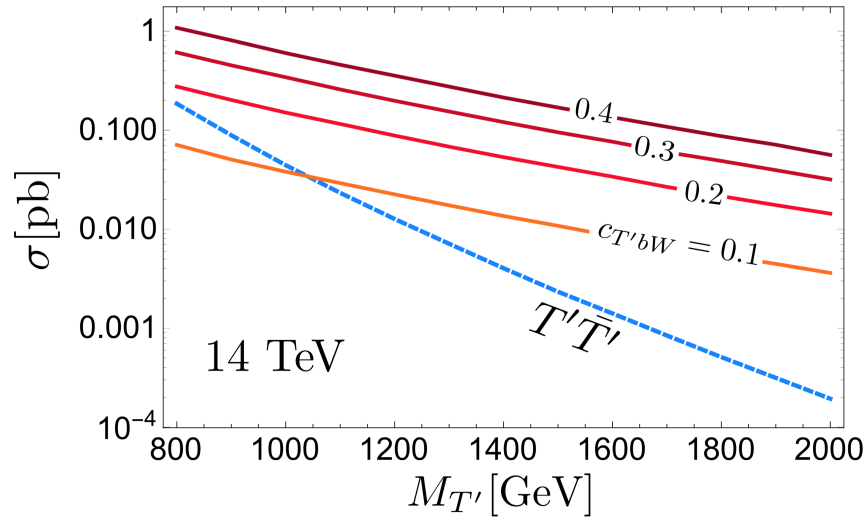
Figure 1.5: Cross-section vs. vector-like top Mass for pair production (dashed blue line) and single production with differing coupling constants (for the coupling to W^+ and b). Taken from [30].

($\sim$ 14 %, as can be seen on [30]) with respect to Zt, it allows for elimination of QCD background by cutting on $\not{E}_T$ (which cannot be easily eliminated were one to consider $T \to Z_{had}t_{had}$). A caveat: it does not allow for the reconstruction of a Z boson.

1.3 Single-top quark accompanied by missing energy

Before moving on, it would be imperative to consider any other models wich predict similar final states and could, in principle be targetted by this analysis. For example, mono-top effective models also allow for a signature compatible with a boosted top topology and a large $\not{E}_T$.

There are two kinds of mono-top effective models: resonant and non-resonant. In the first type, a coloured Scalar resonance, with charge of +2/3, aptly named S, promptly decays into a top quark and an invisible (to the detector), neutral, spin 1/2 colour singlet named f_{met} (as can be seen in figure 1.6). They were first proposed in [31] and the first general effective Lagragian appeared in [32]. A sample Lagrangian [32, 33] would be,

$$\mathcal{L}_{Res} = \epsilon^{\alpha\beta\gamma} S_\alpha \bar{d}^{i,c}_{\beta,R} (a^q_{res})_{i,j} d^j_{\gamma,R} + S\bar{u}^k_R (a^{1/2}_{res})_k f_{met} + h.c., \qquad (1.19)$$

where $(a^q_{res})_{i,j}$ and $(a^{1/2}_{res})_k$ are coupling matrices, describing the coupling to either a pair of anti-quarks or to a top quark and an invisible fermion, respectively..From a theoretical standpoint, several models can predict behaviour compatible with Resonant mono-top.

Examples would include: R-parity violating supersymmetry (where S is a stop quark, and f_{met} is the lightest neutralino [34]), Leptoquark models (leptoquark decays into anti-neutrino and top [35]), or even hylogenesis (a model purporting anti-baryonic Dark Matter [36]).
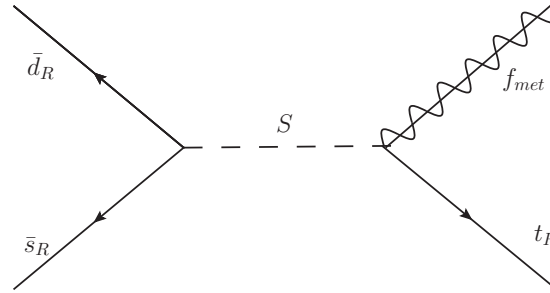
Figure 1.6: Feynman diagram for the s-channel process in which two down type quarks produce a short-lived spin-0 boson which promptly decays into an invisible fermion and a top quark.

In the latter type of mono-top model, non-resonant, an up quark changes flavour, through a neutral current, into a top quark (again, a type of process heavily suppressed in the SM), emitting an invisible, neutral, colour singlet, vector boson v_{met}. This process, unlike the Resonant one, can occur in both the s-channel and t-channel (as can be seen on figures 1.7a) and 1.7b)). A sample Lagrangian [32, 33] would be,

$$\mathcal{L}_{Non-Res} = (a_{non-res})_{i,j}(v_{met})_\mu \bar{u}_R^i \gamma^\mu u_R^j + h.c.. \tag{1.20}$$

Examples of theoretical models that linchpin this process would include R-parity conserving supersymmetry (if one takes into account the cascade production of a neutralino pair [37]), a model proposed to explain forward-backward asymmetry(where two Majorana invisible fermions and a top quark result from a leptoquark and one of the invisible fermions [38]) and even other models where a boson state promptly decays into a pair of neutral stable particles [39].

Of course, in order to fully ascertain the possibility of developing an analysis for both fully hadronic singly-produced T and mono-top, it is imperative to understand kinematic differences/similarities between all models.

1.4   Experimental state of the art

The search strategy for VLQ's applied by the ATLAS experiment at CERN, pertaining to 2012 data, consisted in hunting for different decays of a VLQ (at different final states),
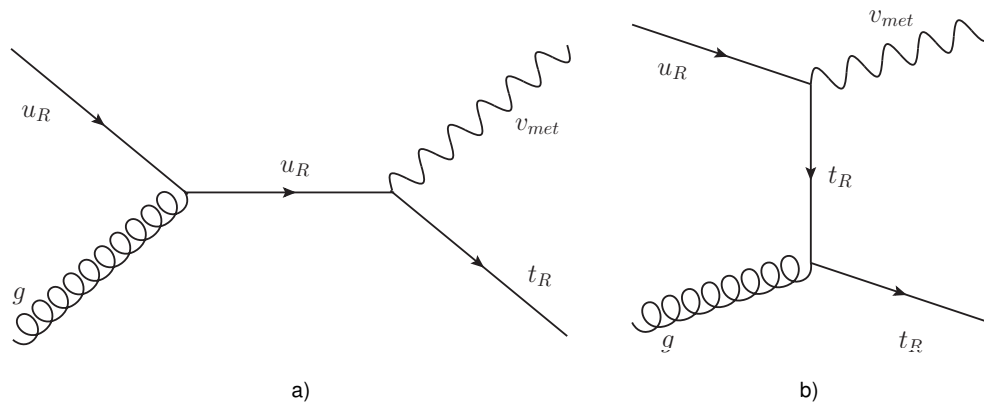
Figure 1.7: Feynman diagrams for the s- and t-channel, respectively 1.7a) and 1.7b), where an up-quark changes flavour neutrally, into a top quark, hereby producing an invisible spin-1 boson.

and then summarising the myriad analysis into a 2D limit plot.

When it comes to pair production it can be seen that no significant excess from the SM background is present either when considering a pair of T's, as in 1.8a), or when considering a pair of B's, 1.8b). The harshest observed limits imposed that masses up to 855 GeV were excluded for a T in a doublet (T,B), and up to 800 GeV for the singlet [29]; for B masses up to 755 GeV considering a (B,Y) doublet, [41], and up to 735 GeV in the singlet case, [29].

As for singly-produced VLQ's, observed exclusion limits rule out the existence of a T singlet with mass up to 0.95 TeV, should one assume a composite Higgs model as the theoretical prediction [42]. Assuming a single-production of a B by means of a heavy vector gluon, yields an observed limit of 2.0 TeV on the gluon mass, should one assume it is double the B mass, the small mixing approximation and a coupling $c(bW) = 1.0$, [43]. Most efforts opted to only impose upper limits on cross-sections multiplied by branching ratios or on mixing and coupling parameters, due to single-production being model-dependent (case in point the analysis at [41] set observed exclusion limits on the cross-section times BR in the range $0.09 - 0.83$ pb, while [44] establishes them at $0.11 - 5.13$ pb). In the case of [41] an interpretation of the limits according to the composite higgs model parameters is also established.

In terms of mono-top searches, ATLAS efforts were concentrated on the leptonic final state. No significant deviations from SM behaviour were reported, as the observed 95% CL limits exclude the possibility of an invisible boson (characteristic of the non-resonant model) up to masses of 657 GeV (under the assumption that $a_{non-res} = 0.2$), and the existence of an invisible fermion (signature of the resonant model) up to masses
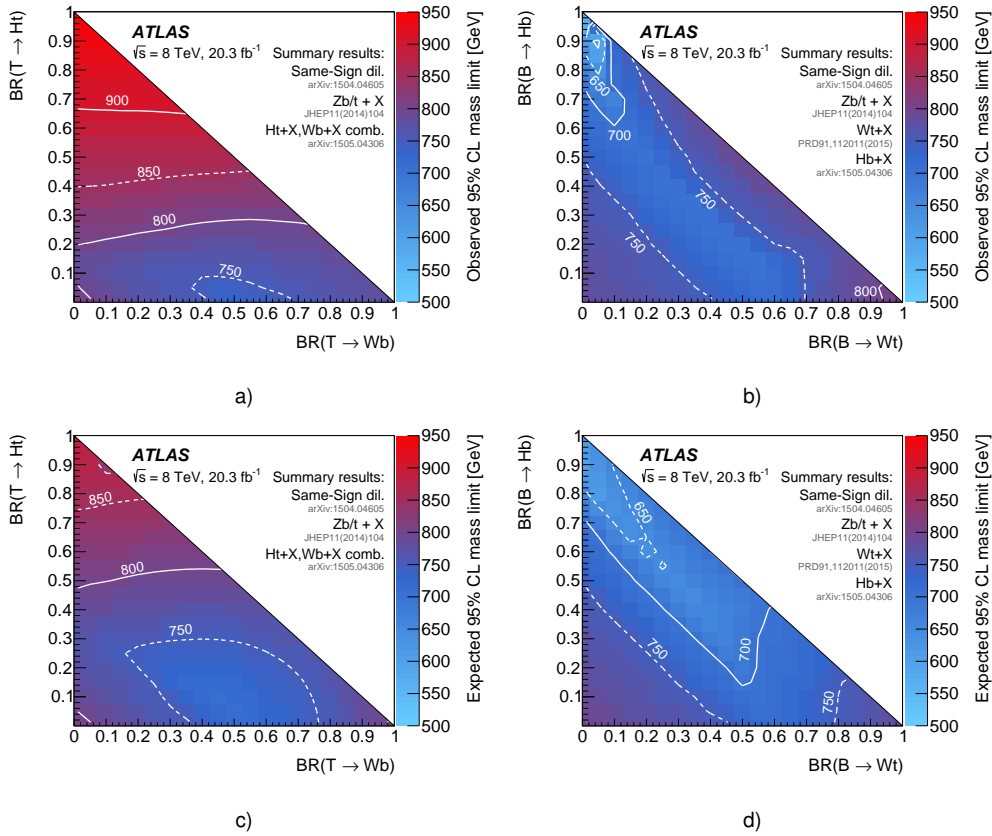
Figure 1.8: Observed lower exclusion limits at 95% Confidence Levels (CL), for pair-produced T, a), and B, b); and expected lower exclusion limits for pairs of T's, c), and B's, d). Mass exclusions for each analysis are sequentially overlaid, and the strongest limit at each bin is shown. Only $Ht + X$ and $Wb + X$ limits are combined, for T only. Plots obtained from [40].

a)

b)
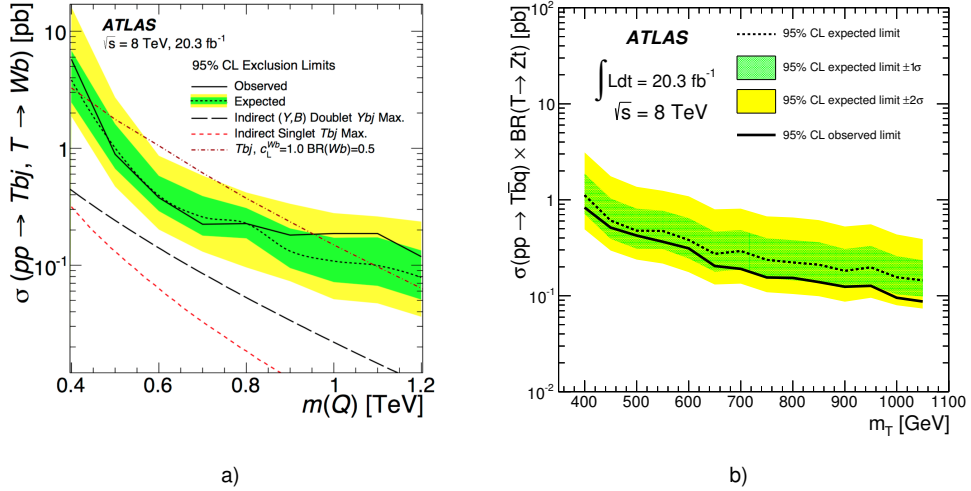
Figure 1.9: Observed and expected limits for cross-section times the branching ratio of the single-production of a Wb decaying Q quark, which, when interpreted as a T in the context of the composite Higgs model, can be used to set an upper limit of 0.95 TeV on the mass of T at a). The observed and expected limits obtained by the analysis focusing on the $T \to Zt$ decay present at b). Figures taken from [42] and [41], respectively.
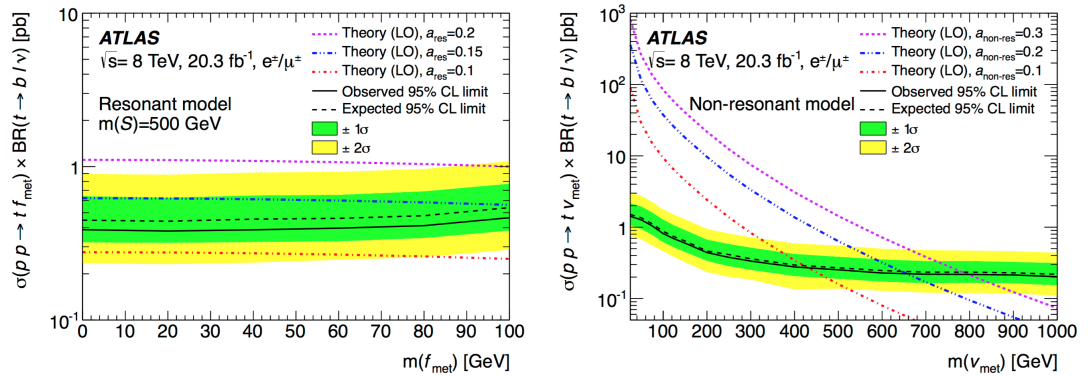
Figure 1.10: Expected and observed exclusion limits for the resonant mono-top model, a), and for non-resonant, b), indicating the $m(f_{met})$ (assuming $m(S) = 500$ GeV) as being excluded up to 100 GeV, and that of $m(v_{met})$, as excluded up to 657 GeV.
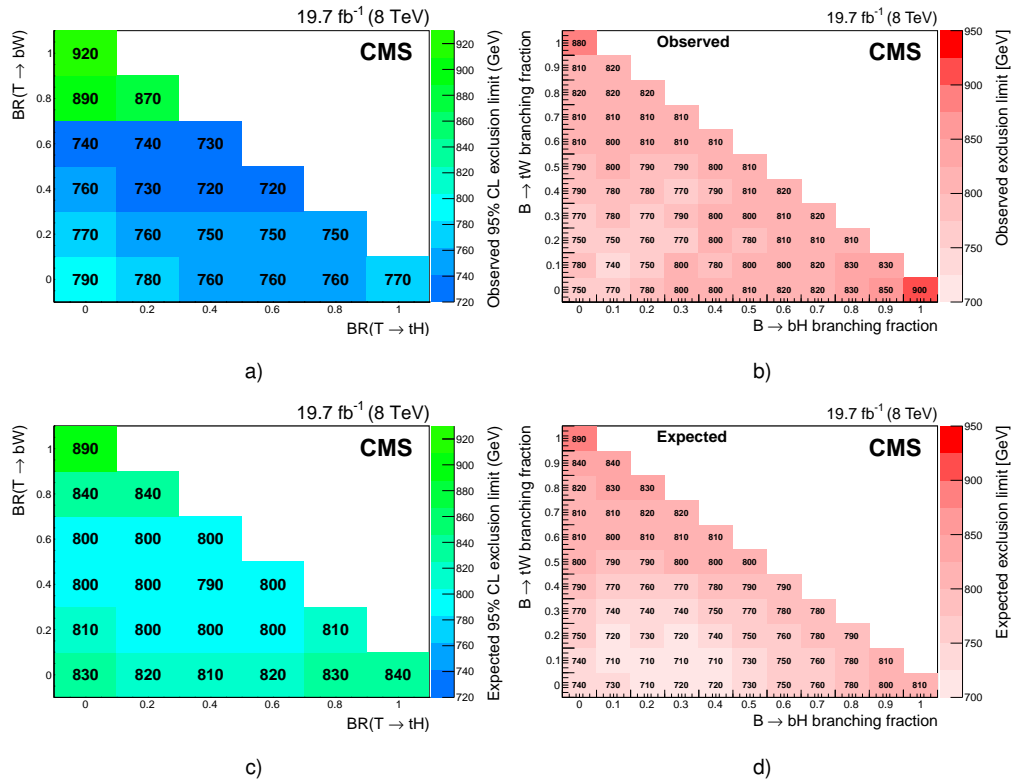
Figure 1.11: Observed combined exclusion limits at 95% Confidence Levels (CL), for pair-produced T, a), and B, b); and expected combined exclusion limits for pairs of T's, c), and B's, d). Figures from [45].

FCUP | 34
Search for top quarks accompanied by missing energy in
hadronic topologies at the ATLAS experiment

of 100 GeV (assuming a scalar resonance with mass of 500 GeV and $a_{res} = 0.15$).

From the CMS experiment, results based on 2012 data denote no significant deviation from background behaviour. In terms of pair production of T's, the harshest observed limits obtained exclude up to a mass of 920 GeV, [46], and for pairs of B's, masses up to 900 GeV, [47]. The search strategy is similar to the ATLAS one, seeking to first study each decay mode separately, but then combine the limits, and recast into a triangular plot.

Single production wasn't considered with data from 2012, however there exist results based on 2015 data. An example would be the analysis concerning the decay into Zt [48], under the small mixing approximation, for a coupling strength of $c(bW) = 1$, wherein the observed cross-section limit is established at the range $0.97 - 0.16$ pb for a T singlet, with masses excluded up 1350 GeV. Observed limits are also obtained for the doublet hypothesis ($0.14 - 0.60$ pb), and for both singlet ($0.17 - 0.68$ pb) and doublet ($0.30 - 1.27$ pb) B. Another analysis ($T \to Wb$, at [49]), set upper bounds on observed cross-sections up to 2.03 pb, and mass exclusion up to 1700 GeV, under the assumption of the small mixing approximation and a coupling $c(bW) = 1.0$. An interpretation for Y quarks (part of a doublet) is also considered.

Again, no deviation from background processes was seen, either in pair or in single production.
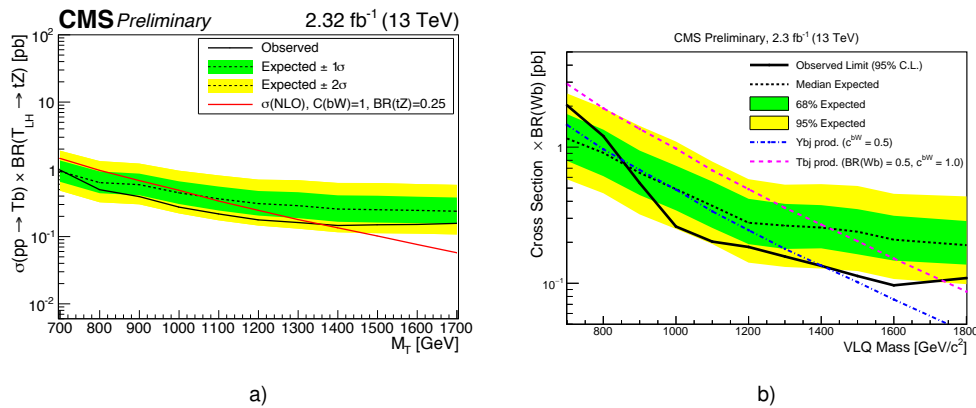
Figure 1.12: The Observed and expected limits on cross-secction times branching ratio for different masses of T, considering either the decay $T \to Zt$ or $T \to Wb$. Taken from [48] and [49], respectively.

On the mono-top domain, based on 2012 data, the observed lower limits impose an exclusion of a scalar invisible particle, of masses up to 330 GeV, and of the invisible vector boson, up to 650 GeV, as can be seen on [50]. Both limits are obtained for non-resonant mono-top, with the assumption that an invisible complex doublet scalar could

be produced in alternative to the invisible vector. These searches are conducted in the hadronic channels, unlike the ATLAS ones. A more recent exclusion limit, based on 2015, from the preliminary result at [51], excludes the existance of an invisible vector boson up to 1100 GeV. No deviations from SM behaviour are observed.
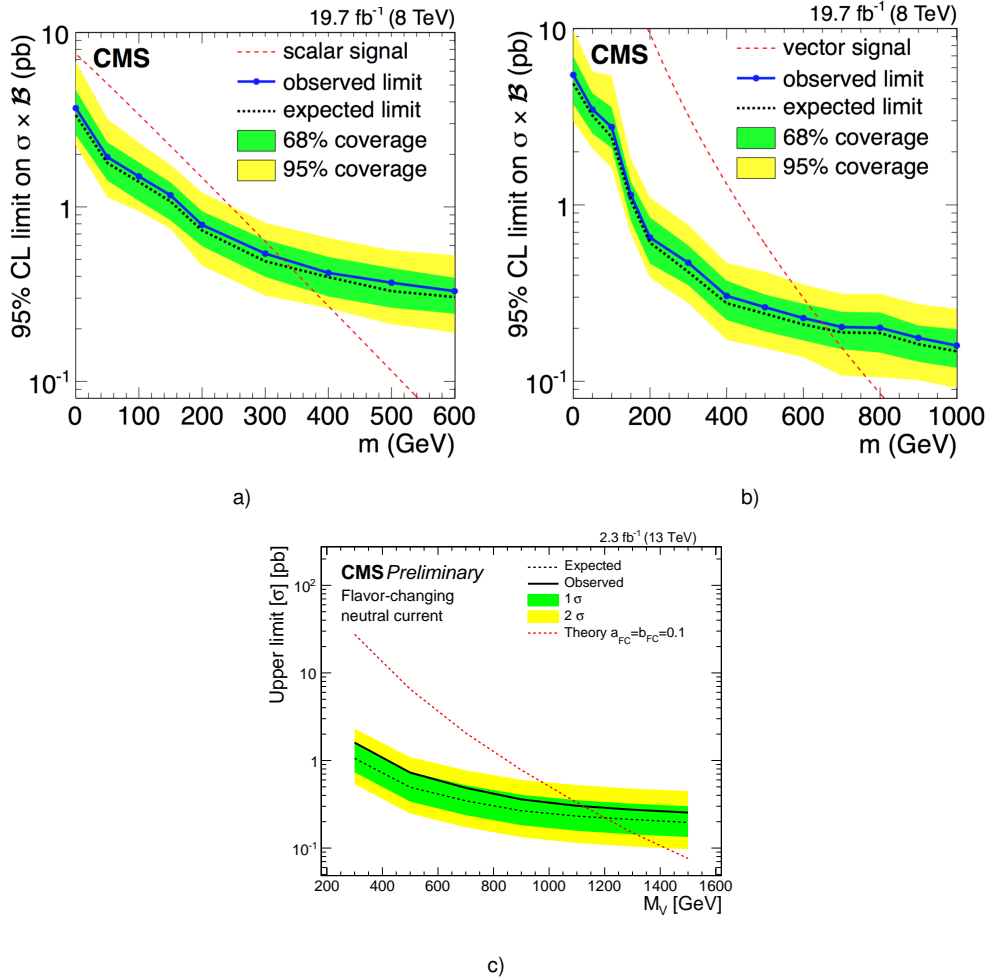
Figure 1.13: Observed lower limits, for mono-top non-resonant assuming an invisible scalar, a), and an invisible vector, b) based on 2012 data. At c) the preliminary exclusion limit fot mono-top non-resonant, based upon 2015 data. First two figures taken from [50], while the last one is taken from [51].

Chapter 2

Experimental setup

2.1 Large hadron collider

The Large Hadron Collider (LHC) is a record-breaking particle accelerator built by the European Organisation for Nuclear Reasearch (CERN), housed in the Franco-Swiss border, near the Alpes. It is currently the largest (27 km circumference) and most powerful accelerator, capable of opperating at an energy of 13 TeV. It houses several detectors wherein accelerated beams collide. Now, depending on the experiment/detector, the purpose woud be to investigate the aftermarth of proton-proton collisions, and from this to confirm (or deny) the existence of particles predicted by several new physics models or even improve upon existing measurements.
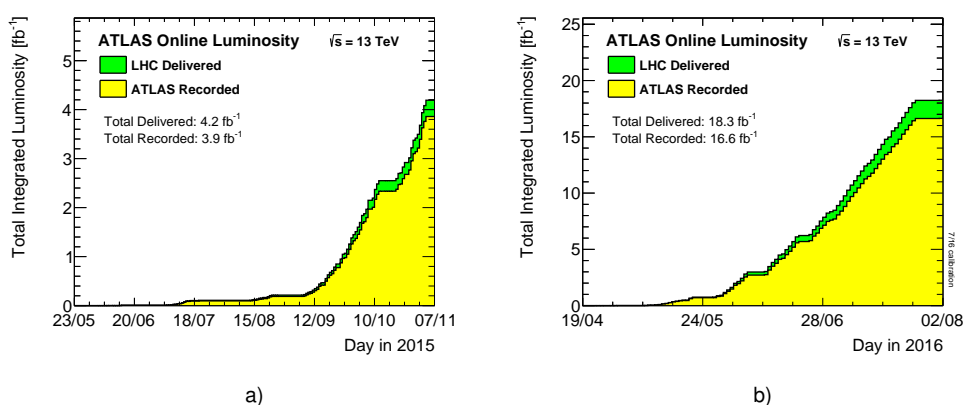
Figure 2.1: The total integrated luminosity observed by the ATLAS detector on a day-by-day basis, throughout the period corresponding to June to November of 2015 on a), and throughout April to August 2016 at b). Taken from [52].

The LHC has had one successful operations phase (where the existence of the elusive Higgs boson was confirmed in 2012), at $\sqrt{s} = 8$ TeV, from 2009 to 2013, de-

nominated Run 1. Beginning in 2015, the LHC is undergoing a second operations phase (Run-2), and as such is presently colliding protons at $\sqrt{s} = 13$ TeV. The data to be used throughout this thesis, was obtained during the Run-2 phase, throughtout 2015 and corresponds to an integrated luminosity of 3.21 fb^{-1}.

2.2 ATLAS detector

The detector wherein this data was collected is named "A Toroidal LHC ApparatuS" (ATLAS) thusly named due to the large eight air-core superconducting toroidal magnets. Such magnets, in conjuntion with the inner solenoid magnet produce a curvature on resulting particles, thus enabling measurements of particle momenta, either in the inner detector and in the Muon Spectrometer, respectively.

The symmetrical nature of the detector makes the usage of cylindrical coordinates natural. In this case, should one consider the z-axis as being parallel to the beam-pipe, the y-axis pointing upwards and x as perpendicular to both, the coordinate system boils down to: an azimuthal angle ϕ, defined as an angle in the XY plane (also known as the transverse plane, due to being perpendicular to the beam axis), and a pseudo-rapidity, $\eta = -log[tan(\theta/2)]$, where θ is the angle with the positive (anti-clockwise direction) z-axis. Momentum confined to the XY plane is denoted p_T, the transverse momentum, and defined as $p_T = \sqrt{p_x^2 + p_y^2}$.

ATLAS can be subdivided into the following sections:

1. Inner detector system, whose main job is to track charged particles precisely; it can be further subdivided into three layers:

   (a) Pixel detector, composed of approximately 80 million readout channels (47000 pixels per module and around 1744 modules). Such a high count is necessary to ensure precise tracking in close proximity to the interaction point (this is the innermost layer of the inner detector). Each module is comprised of a slab of silicon, which acts as the detecting material. In the barrel region, the pixel detector is composed of four separate layers, the two innermost ones are named B-layer and Insertable B-Layer (IBL). The IBL was not present during initial operation of the LHC, it is a planned upgrade in order to future-proof the detector against damage and irreparable failure occuring in the innermost B-Layer, and for ensuring adequate performance during proposed higher luminosities. It also has the added benefit of increased tracking, b-tagging and vertexing performance. More details about the IBl can found at [53];

FCUP | 38
Search for top quarks accompanied by missing energy in
hadronic topologies at the ATLAS experiment

(b) Semi-conductor tracker (SCT), which is the middle component of the inner detector, has a similar design to the pixel detector, however instead of minute pixels, it uses narrow strips of Silicon. This makes it ideally suited to cover larger areas, such as, for instance, the XY-plane (at cost of having lower precision when compared to the pixel Detector).

(c) Transition radiation tracker (TRT), where the goal is to combine transition radiation detection with a straw tracker, as such the straws are filled with a gas - to be ionized when a particle passes by - and, in between the straws, there exist materials with varying refraction indices. Since the probability of generating transition radiation is higher for highly relativistic particles, and for lighter ones, dominant signals will, most likely, correspond to electrons and positrons. The TRT is the outermost layer of the inner detector.
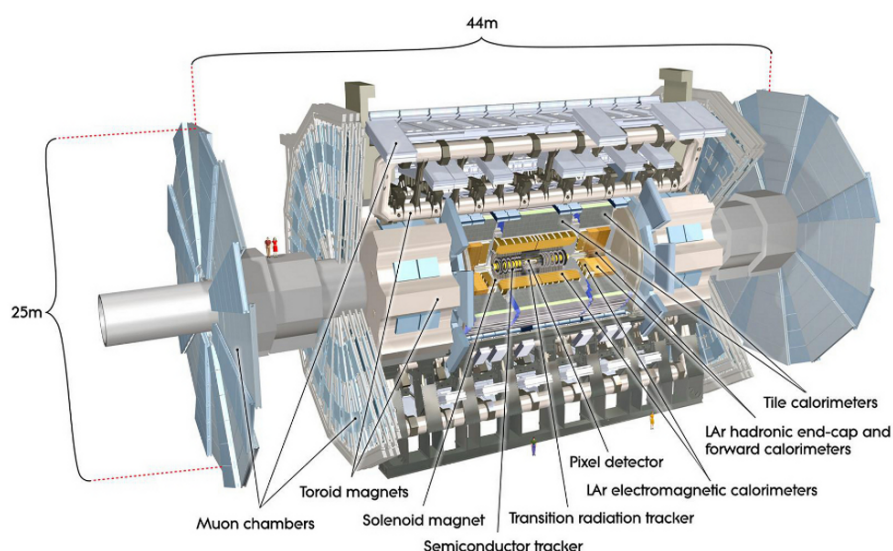
Figure 2.2: An overview of the ATLAS detector, taken from [54].

2. Calorimeters, their primary function is to measure the energy from outbound particles (photons, electrons, jets, $\not{E}_T$[1]) by absorption. It lies between the inner detector and the Muon Spectrometer. There are three types of calorimeters:

(a) Electromagnetic, this innermost calorimeter absorbs energy only from particles that interact through electromagnetic means (such as photons, elec-

---

[1]Before a given collision, there is no net momentum in the transverse direction. After beams collide, if a net amount of transverse momentum is present it is thus indicative of unaccounted momenta, known as missing transverse energy, denoted $\not{E}_T$. This quantity is commonly associated with particles that evade detection by the detector.
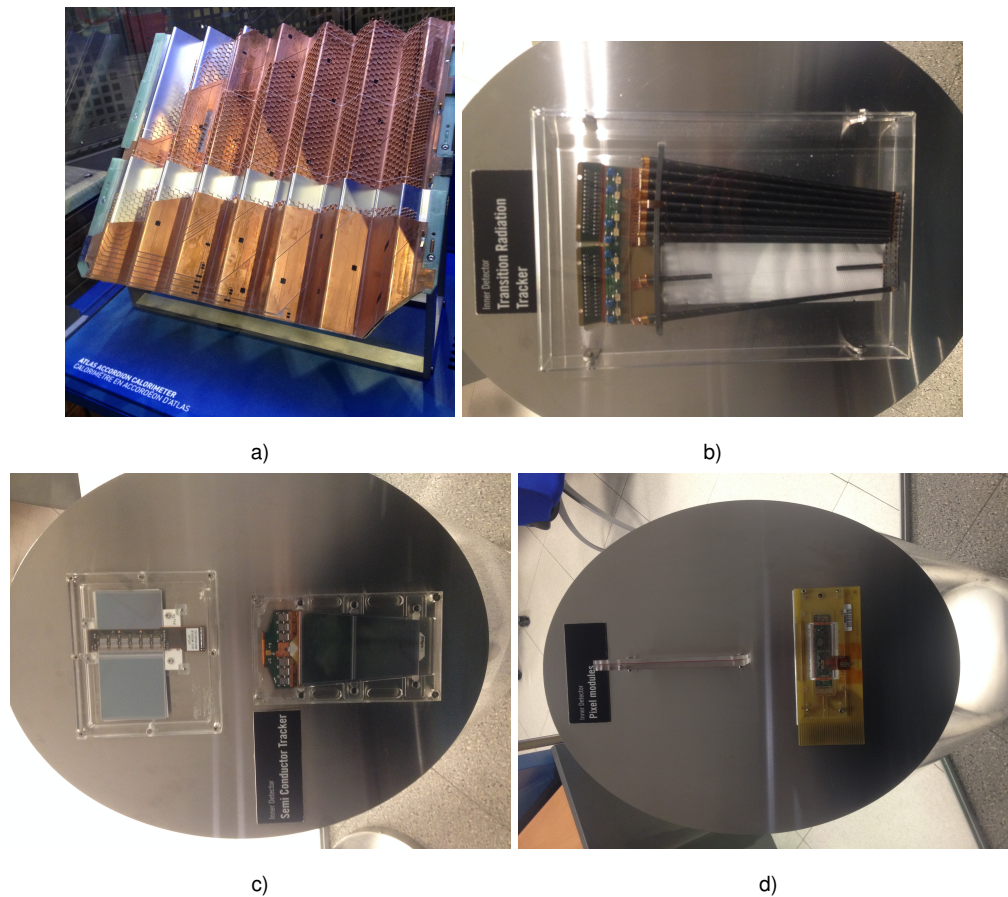
Figure 2.3: A few parts from the Hadronic Calorimeter, a), and from the inner detector including: the transition radiation tracker, b), the semi-conductor tracker, c) and the pixel detector, d).

trons). Yielding information about the angular position of each energy deposit (ie. both pseudorapidity and, η and azimuthal angle, ϕ) and particle identification (by looking at the resulting shower caused by the interaction between an outgoing particle and the detection material, for example, bremsstrahlung and the creation of electron-positron pairs). It is comprised of accordion shaped Lead/Stainless Steel electrodes that act as absorbing materials, dipped in Liquid Argon, which acts as a sampling material. It covers both the endcap (covering $1.4 < \eta < 3.2$), the barrel (located at $|\eta| < 1.4$) and the forward regions (positioned at $3.1 < |\eta| < 4.9$) of the detector;

(b) Hadronic, absorbs energy from particles that left an imprint on the Electromagnetic Calorimeter and interact through the strong force (thus leaving, in the hadronic colorimeter, the remnants of strongly decaying particles and possibly some $\slashed{E}_T$). It features two different sets of materials for two different

regions of the detector: steel as energy-absorbing coupled with scintillating tiles as the sample material for the barrel ($|\eta| < 1.0$), and copper or tungsten as absorbers and liquid argon as a sampler, for the endcap ($1.5 < |\eta| < 3.2$) and forward region ($3.1 < |\eta| < 4.9$).

3. Muon Spectrometer, the outermost layer of the ATLAS detector, marks one of the major differences between ATLAS and CMS (it is a separate stand-alone tracker of muons, which CMS doesn't possess). It is similar in function to the inner detector, however, much larger in size, of lower spatial resolution and with a different magnetic field configuration (toroidal vs. solenoid). Very few particles, other than the aforementioned muons and neutrinos, are expected to reach this part of the detector (as most particles have been stopped at the calorimeter), and thus leave an imprint upon it. It can be subdivided into a barrel ($|\eta| < 1.4$) and an end-cap ($1.1 < |\eta| < 2.8$).

A more detailed description of the ATLAS detector can be found at [55].

2.3 Trigger system

During the first phase of operations of the LHC collisions of proton bunches took place in ATLAS, at a rate of 20 MHz (bunch spacing 50ns). In the second phase, collisions took place at double the rate 40 MHz (bunch spacing 25ns). Having these many collisions produces a gigantic amount of data, however, due to the limitations of hardware, both in terms of data throughput and in terms of storage, it is unfeasible to keep all events. There is then a need for a system, which based on a number of criteria, can decide which events are physically relevant, and therefore to be kept, in real-time. These rapid decision making systems are known as triggers.

Triggers acomplish this by checking high-p_T physics objects, such as muons, electrons, taus, large $\not{E}_T$ and jets [2] against a variety of interesting physics signatures, where a list of criteria for the acceptance of an event is found.

In ATLAS, triggers can be subdivided into two categories: a software high-level trigger (HLT), and a hardware trigger (named Level 1, L1). The L1 triggers can be subdivided into three components: the calorimeter trigger (which processes input from both

---

[2]A stream of clustered collimated particles. They can be constructed using energy depositions in both calorimeters cells (topological clusters), in which case they are known as calorimeter jets, or from clustering particle tracks from the inner detector, thus providing track jets.
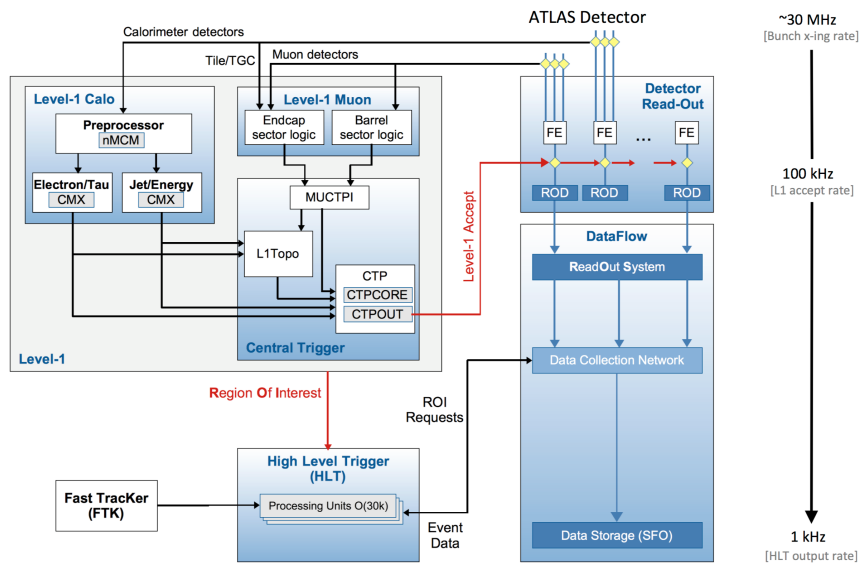
Figure 2.4: A flowchart detailing the ATLAS Run-2 trigger system as found in [56, 57].

calorimeters - EM and hadronic - and outputs trigger signals to the central trigger processor, CPT), the muon trigger (where inputs from the end-cap and barell regions of the muon detectors are processed) and central trigger components (where for example, the L1 topo system performs topological selections - such as, for instance, a requirement on an invariant mass, on sum of transverse momenta, angular distributions, etc; all information for both L1 subsystems ends up at the CTP and are used to provide regions of interest - RoI's). As for the HLT's they are now grouped into a single event farm responsible for object reconstruction (whereas previously, in Run-1 they were subdivided in a Level-2 trigger and an event filter - responsible for ensuring full event reconstruction), providing lower complexity and more shared resources. In terms of event rates, one ends up going from 40 MHz (inputs to L1 trigger), to 100 kHz (outputs of L1 trigger) and, at the and, 1 kHz (HLT output rate).

More information about the ATLAS Run-2 trigger system can be found at [56, 57], whereas about the original design more details can be found at [58, 59].

2.4 Worldwide LHC computing grid

The LHC is capable of generating an annual amount of data of around 30 Petabytes. In order to store, process and distribute these vast quantities of data non-centrally, the Worldwide LHC Computing Grid (WLCG) was created. It is currently the largest

computing grid, being a joint effort of 170 computing centers in at least 42 countries, as
of 2015.
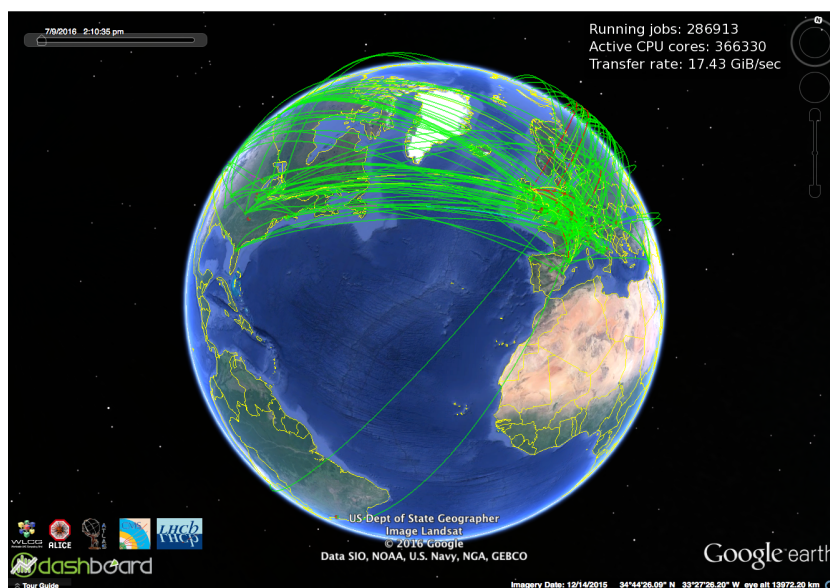
Figure 2.5: The WLCG operating all over the globe during the afternoon of the 9th of July, 2016; Image obtained using
a Google Earth Dashboard from [60].

The infrastructures that comprise the WLCG can be divided into four tiers: the Tier-
0, which is CERN's computing centre at CERN, and the Wigner Research Center for
Physics in Budapest, have a dedicated connection to the counting room (where data
pours in from all the detectors and a first attempt at reconstruction is made); Tier-1,
includes 13 academic institutions, where data sent from CERN is sent and stored (in
fact even raw subsets of data are sent, instead of only processed data, thus making
Tier-1 sites backup repositories); Tier-2 are universities and research institutions, where
a sufficient amount of data, and the necessary computing resources for an analysis are
made available; and Tier-3 nodes are local clusters and individual computers.

Further details about the WLCG can be found in the Technical Design Report, at
[61].

Chapter 3

Parton level studies

In order to ascertain the possibility of developing an analysis to cover the three distinct models that envisioned a final state with hadronic top and invisible particles, one of the tasks undertaken in the beginning of this thesis was to develop a parton level (only gleaming at parton interactions, without simulating hadronization and even detectors) comparison of the three, using simulated samples.
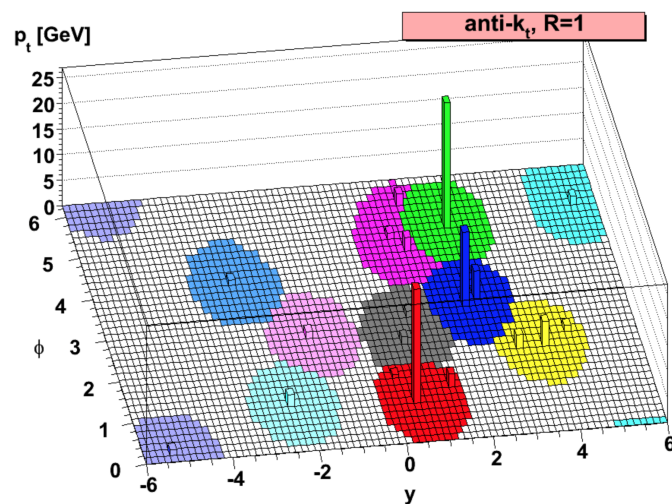
Figure 3.1: The spatial distribution of the p_T of jet constituents, for jets obained using the anti-k_t algorithm. Note the characteristic conical shape. Plot taken from [62].

The jets used in this study were formed from feeding generated particles into a jet clustering algorithm known as anti-k_t[62]. This algorithm is sequential in nature and works by repeatedly recombining the closest constituents according to some distance

FCUP | 44
Search for top quarks accompanied by missing energy in
hadronic topologies at the ATLAS experiment

measure. The most usual distance measure is denoted the splitting scale,

$$d_{ij} = \min(p_{Ti}^{2p}, p_{Tj}^{2p})\frac{\Delta R_{ij}^2}{R^2}$$

where, p_{Ti} is the transverse momentum of constituent i, p is a parameter (which, for anti-k_t algorithms is established to be $p = -1$), $\Delta R_{ij} = \sqrt{\Delta\eta_{ij} + \Delta\phi_{ij}}$ is the angular separation of the two constituents, and R denotes the radius parameter.

A quick overview of the modus operandi of the anti-k_t algorithm involves iteratively computing d_{ij}, and comparing it to $d_{iB} = p_{Ti}^{2p}$: if d_{ij} is smaller, recombine constituents i and j, otherwise, if d_{iB} is smaller, accept i as a final state jet. Since the distance scales are inversely proportional to p_T's this essentially means that d_{ij}'s between soft (low p_T) particles is large, when compared to the d_{ij} between a soft and a hard particle. The consequence of this, is that soft particles have tendency to cluster with hard ones, instead of amongst themselves (and will naturaly give rise to conically shaped jets, as can be seen in figure 3.1). It can accept as seed several types of objects, not being restricted to generated particles. For example it can even accept jets with a small radius (for instance with $R = 0.4$) and form large-R jets (with $R = 1.0$), as was performed in this study.

a)   b)
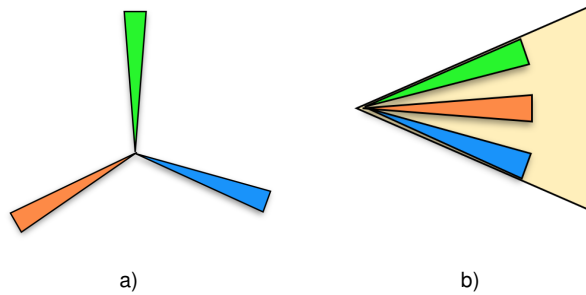
Figure 3.2: The three subjets resultant from hadronic top quark decays, when one assumes the top quark at rest, in 3.2a) (representative of the non-boosted regime), and when the top quark has a high p_T, at 3.2b) and, as a consequence, a fat jet emerges (boosted regime).

This work was developed in collaboration with Sonja Bartkowski from TU Dortmund, using samples provided by Dennis Sperlich from Humboldt-Universitat Zu Berlin (single T) and by Johannes Erdmann from TU Dortmund (monotop).

Now, in single T we expect a boosted top topology (where high p_T top quarks decay hadronically into three highly "collimated" subjets, which appear as a wide large-R jet, as can be seen in figure 3.2b)), a high component of $\not{E}_T$ (due to the Z boson decaying into a pair of neutrinos) and at least one forward jet ($2.5 < |\eta| < 4.5$), as predicted by [30].

a)

b)

c)

d)

e)
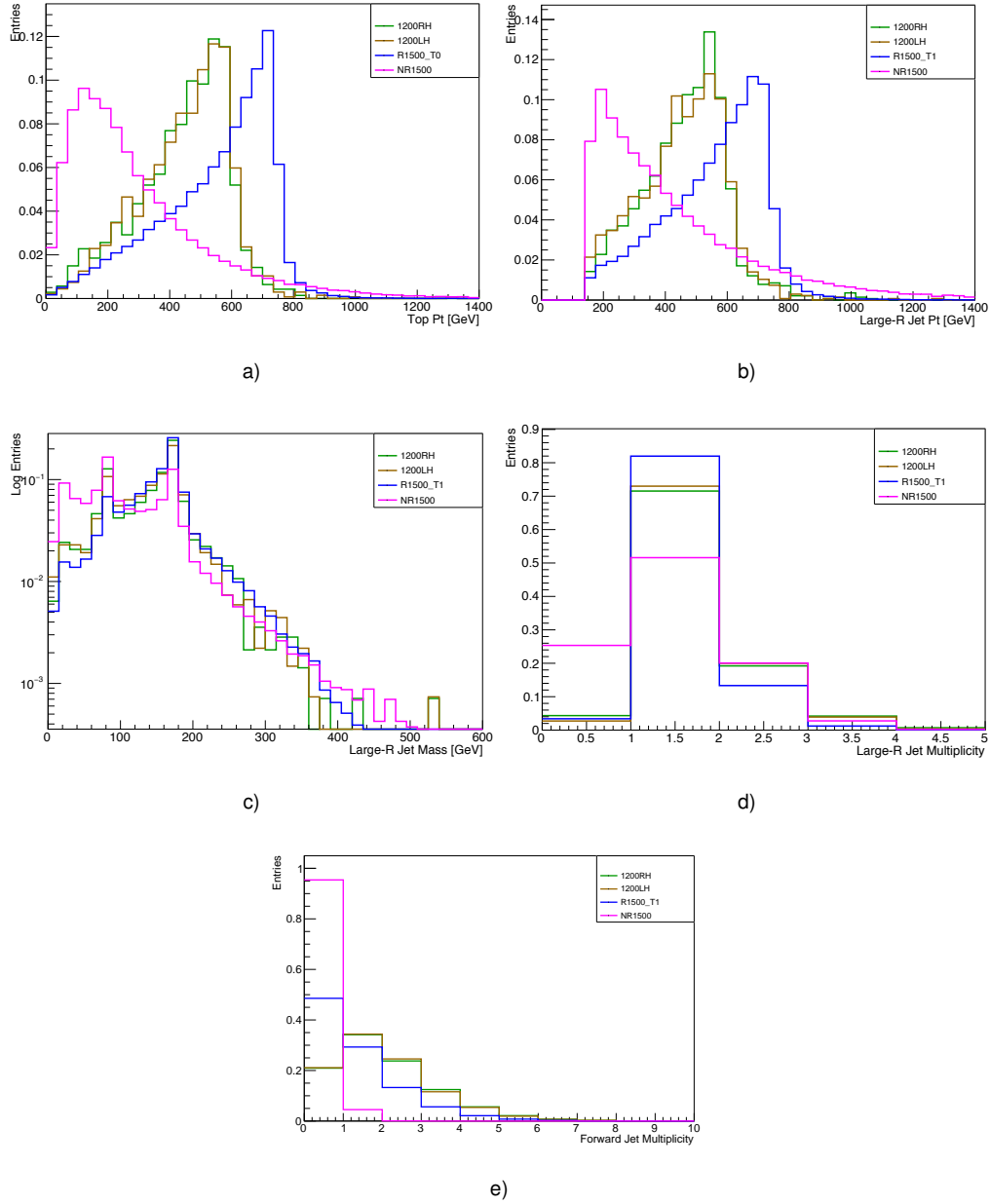
Figure 3.3: Some plots, where the p_T of a top quark, 3.3a), the p_T of Large-R jets, 3.3b), the Large-R jet mass, 3.3c), the Multiplicity of Large-R jets, 3.3d), and the Multiplicity of small-R jets forward Jets, 3.3e). The Green and Brown Solid Lines indicate single T with a mass of 1200 GeV, with Right-Handed and Left-Handed chirality, respectively. As for mono-top, blue indicates the resonant Model where the scalar Resonance S takes a mass of 1500 GeV and the invisible Fermion a mass of 50 GeV; the pink line showcases non-resonant, where v_{met} has a mass of 1500 GeV.

FCUP | 46
Search for top quarks accompanied by missing energy in
hadronic topologies at the ATLAS experiment

For mono-top resonant and non-resonant, one can expect the forward jet requirement to not be applicable (momentum fractions of incoming partons are of the same order, thus there will be a preference for no forward jet). In terms of the appearance of a boosted top, one can expect it to appear for resonant but not for non-resonant (decay of a massive particle vs a FCNC, respectively).

The predictions regarding the presence of a boosted top topology in both the resonant and single T are confirmed from looking at the similar shapes present in 3.3a) and 3.3b). Also evidenced by these plots, is the fact that the non-resonant model does not incur in such boosted behaviour, and can no longer be considered for this analysis. Also as predicted, single T models favour the appearance of at least one forward jet, while both mono-top models favour mostly zero forward jets (3.3e)).

In conclusion, we can develop an analysis targeting both mono-top resonant and single T as they are kinematically similar, exploring the possibility of differentiating between the two signals by means of a forward jet cut (3.3e)). Non-resonant mono-top will not be considered.

Chapter 4

Building blocks of an analysis

The main purpose of an analysis is to confirm or deny either one of two hypothesis: having only the existence of SM processes (known as background), or signal (the particle we are searching for) together with background. In conclusion, if there exists a deviation from SM behaviour, one has effectively detected a particle. Or maybe, some type of bias was introduced that caused such an excess (after all, staticians and researchers are also, first and foremost, human beings, and thus not impervious to biasing errors).

A type of bias that can occur, will happen if the experimentalist, despite his best efforts, unwittingly and/or unknowingly introduces a slight preference of data to fit into either one of the two hypothesis. In order to avoid this, one can attempt to have a series of demands designed to boost the dominance of the signal over background, but without using data (this series of requirements define a "signal region"). And only when one has enough confidence in the correct modelling of signal and backgrounds, can one remove the metaphorical blind-fold and have a look at data. This technique, of selectively ignoring data in the signal region until background processes are properly modelled, is known as "blinding".

In the previous paragraph, correct background modelling was introduced as a requirement for unblinding. This is so, as the inclusion of too many processes (or the omission) can also be a source of bias (if for instance, the disagreement between data and background is caused not by signal, but by some missing/extra SM process). Or, what if one of the backgrounds was improperly modelled? In order to avoid this pitfall, one can define a number of demands for the main sources of background processes unblinded (denominated control regions) and every time data is in good agreement with the sum of background processes, the less likely it is for the previous biases to exist.

Before having a look at the signal and background selections that comprise this

FCUP | 48
Search for top quarks accompanied by missing energy in
hadronic topologies at the ATLAS experiment

analysis, it is important to define the type of objects to be used and the pre-selection applied.

4.1 Object definition and pre-selection

The singular high-level trigger to be used in this analysis is denominated the "HLT_xe70" trigger ("xe" refers to the physics object used to output a trigger decision, in this case, the missing transverse energy, $\not{E}_T$, and 70 refers to a $\not{E}_T > 70$ GeV requirement). All events that do not pass the aforementioned trigger decision are discarded.

The objects to be used throughout this thesis include: three types of hadronic jets, $\not{E}_T$, muons and electrons.

Firstly, small-R calorimeter jets, which are clustered from energy depositions in topological clusters using the anti-k_t algorithm with a radius parameter of $R = 0.4$. They are required to obey the following criteria: $p_T > 25$ GeV, and $|\eta| < 2.5$. Small-R jets with $2.5 < |\eta| < 4.5$ are also used, and identified as forward jets. A jet cleaning procedure is applied, where jets created identified as possibly coming from detector defects are discarded. In addition there must be jets resultant from noise bursts in calorimeters. The small-R jet closest to an electron, within a radius of $\Delta R = 0.2$ is to be discarded. No jets are allowed to have at least two tracks close ($\Delta R < 0.4$) to a muon.

Next up, the large-R jets. These jets are also clustered from information in topological clusters with the anti-k_t, however they use a larger radius parameter $R = 1.0$. They are required to obey the following criteria: $p_T > 300$ GeV, $m > 50$ GeV and $|\eta| < 2.0$. In tandem with the anti-k_t clustering algorithm the jets undergo a trimming [1] procedure. Large-R jets likely to contain a hadronically decaying top-quark are marked as top-tagged (the respective algorithm being described in 4.3.1).

The last type of jets used are track jets. Reconstructed also using the anti-k_t algorithm, however with different inputs (charged particle tracks from the inner detector), and an even smaller radius parameter $R = 0.2$. They are required to have $p_T > 10$ GeV and $|\eta| < 2.5$. Track jets likely to contain a b-quark are identified as b-tagged (further details in 4.3.1).

The missing transverse energy ($\not{E}_T$), is the unaccounted energy from the p_T vector sum of three other physics objects, such as muons, electrons and jets assuming the

---

[1] An algorithm applied in tandem with anti-k_t clustering that demands that, for each subjet of a given jet, only subjets that obey $p_{Ti}/p_T^{jet} < f_{cut}$ are to be kept, where p_{Ti} is the transverse momentum of a subjet, p_T^{jet} the transverse momentum of the parent jet and f_{cut} is a parameter. This provides selective removal of soft radiation, thus ensuring better event reconstruction [63].

FCUP | 49
Search for top quarks accompanied by missing energy in
hadronic topologies at the ATLAS experiment

total initial p_T to be null. To ensure $\not{E}_T$ is constructed from the best possible candiates, its calculation is performed after the calibration of each physics object.

Electron candidates are constructed from EM calorimeter depositions matched to charged tracks from the inner detector. They are required to have a $p_T > 25$ GeV and $|\eta| < 2.47$. Isolation criteria are applied to the calorimeter depositions and to the charged tracks, wherein for a variable $\Delta R/p_T$ sized cone (each attempting to satify a given efficiency) around each given candidate, no other reconstructed electrons are allowed. When it comes to electron identification, the medium likelihood based multivariate method described at [64] is applied. Electrons that share an inner detector track with a muon are not allowed. After the electron-jet proximity requirement above, electrons close to the remaining jets (within a radius of $\Delta R = 0.4$) are to be rejected.

Muons are reconstructed by combining information from both the muon spectrometer and the inner detector. They must satisfy $p_T > 25$ GeV and $|\eta| < 2.5$. Isolation criteria are the same as those for electrons. Muons are required to pass the medium quality criteria present at [65]. In addition to the muon-jet overlap criteria above, muons close to jets with more than two tracks (within a radius of $\Delta R = 0.4$) are to be rejected. When it comes to a preselection, events were required to acquiesce to the following demands:

1. Data events must be in the good runs list (GRL): there exists a a list of runs compiled by the data quality and combined performance groups, where each subsystem in a luminosity block has a group of flags describing the quality of physics objects (jets, muons, etc.). The GRL corresponds to a subset of that list where flags of each subsystem are required to be "good";

2. At least one primary vertex (a physical Interaction Point of the particle collision) per event;

3. A minimum $\not{E}_T$ of 200 GeV, since the aforementioned trigger is fully efficient only above this threshold, as can be seen in figure 4.1;

4. At least one large-R jet;

5. At most one muon and at most one electron;
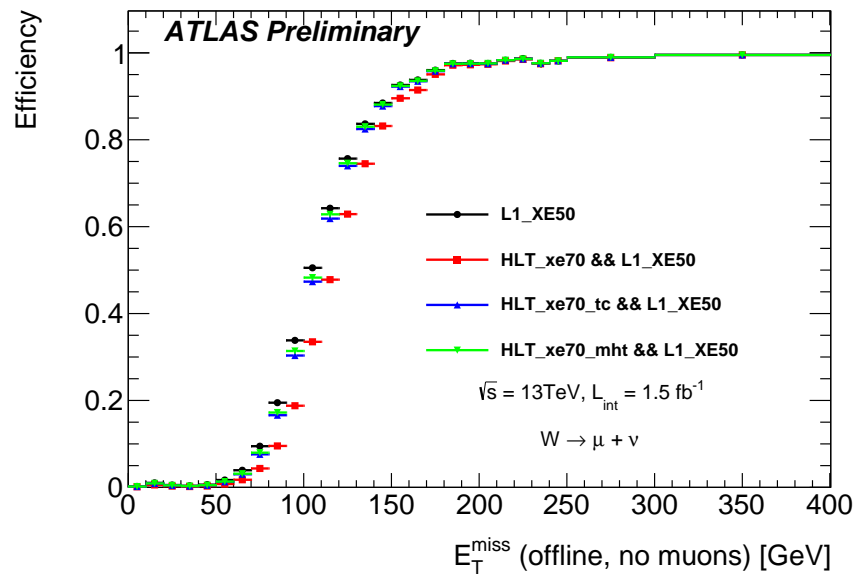
Figure 4.1: The HLT_xe70 Trigger turn-on curve for data (after events pass a selection meant to single out $W \rightarrow \mu + \nu$; and where missing is reconstructed either from jets, electron, photons, or just from jets, _mht, or from topological clusters, _tc). The plot was taken from [66].

4.2   Samples used

In order to accurately model the background events, different simulated samples were used. In terms of background samples the most dominant in the signal region contained processes with top quark pair production (hereby monikered for convinience as $t\bar{t}$; generated by POWHEG-BOX[67] interfaced through PYTHIA[68] to provide hadronization), processes resulting in a vector boson and jets, with different minimum p_T of the vector boson (marked in plots as $W + jets$ and $Z + jets$; generated with SHERPA[69]), and processes resulting in a single top quark (generated by POWHEG-BOX[67], interfaced through PYTHIA[68]).

Also included (and pictured as "Other", in all plots from now on) are samples described the production of a pair of top quarks associated with a vector boson (generated with SHERPA[69]), a pair of top quarks and a Higgs boson and di-boson (obtained with POWHEG-BOX[67] interfaced with PYTHIA[68]), samples enriched in events capable of producing Z bosons associated with a Higgs (generated by MADGRAPH_AMC@NLO[70] interfaced with PYTHIA[68]) or associated with a single top quark (HERWIG [71])

In term of signal samples, single production T (right- and left-handed, separately) events were generated by Dennis Sperlich from Humboldt-Universitat zu Berlin, using MADGRAPH interfaced through PYTHIA[68] using both two production vertices: either

through the coupling to a Z boson, or a W boson. Throughout this thesis, we've chosen to focus solely on the signal corresponding to the left-handed single T produced by the W boson vertex.

4.3 Roots of the analysis

4.3.1 Towards a signal region

a)

b)

c)
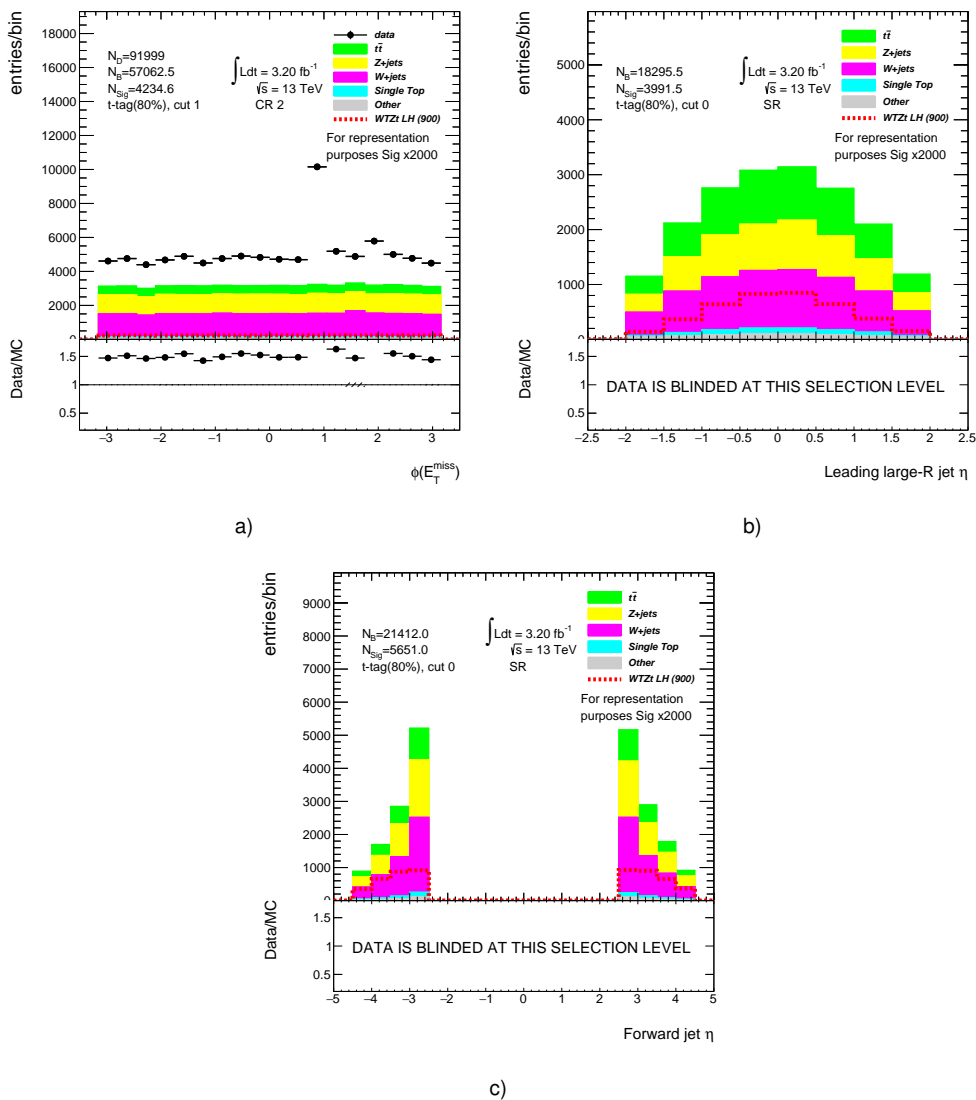
Figure 4.2: The distribution of $\phi(\not{E}_T)$ in a), the η of the large-R jets used throughout this analysis in b) and the η of forward jets, in c).

At the beginning of this chapter, we mentioned trying to find deviations in data from SM behaviour, that can potentially be described by our signal. It's possible to implement a series of demands, with the express intent of weeding out background events and become able to more easily see (possible) signal events. In order to do so, a basic selection was first envisioned (table 4.1). From then on the statistical correlations between variables of interest were studied, thus allowing to predict which new requirements to implement.

1	0-lepton
2	Reject $\phi(\not{E}_T) \notin [0.7, 1.3]$ or $\phi(\not{E}_T) \notin [1.8, 2.2]$
3	$\not{E}_T > 200$ GeV
4	1 b-tagged Track Jet (70% efficiency)
5	1 top-tagged Large-R Jet (50/80% efficiency)

Table 4.1: A short overview of the basic selection.

The first demand in the basic selection demands exactly zero leptons (our signal is fully hadronic and so this demand will help clean out background processes with a preference for leptonic events). Afterwards, one rejects events in the regions with $\phi(\not{E}_T) \notin [0.7, 1.3]$ or with $\phi(\not{E}_T) \notin [1.8, 2.2]$. This is due to an anomalous behaviour ("spikes" in data for both $\phi(\not{E}_T)$ and for $\phi(jets)$) occuring whenever jets hit dead calorimeter cells (by doing so, the energy of said jet is incorrectly read, causing a higher than normal $\not{E}_T$ in the opposite direction in the XY plane, and since the trigger used for this analysis is a $\not{E}_T$ trigger thus causing the "spikes" seen in 4.2a)). The jet cleaning requirement applied in section 4.1, seems to alleviate the issue somewhat, but it does not solve the problem completely. The $\phi(\not{E}_T)$ threshold is a temporary solution until there is a better way of treating the problem, with minimal impact on signal. The solution to this quandary is currently being investigated.

Next up, a requirement on $\not{E}_T$. For the basic selection study, the $\not{E}_T$ was kept a minimum (ie. $\not{E}_T \geq 200$ GeV). In order to have a description of all possible backgrounds, a data-driven multijet estimate is being implemented by Sonja Bartkowski of TU Dortmund. As such, the possibility of raising this demand to 300 GeV (in order to reduce multijet background) was taken into account when performing variations of the signal region. It is not, at this point, entirely clear if keeping the minimum threshold at either 200 or 300 GeV would yield a better limit.

Afterwards, it is requested that only events with exactly one b-tagged track jet (70%
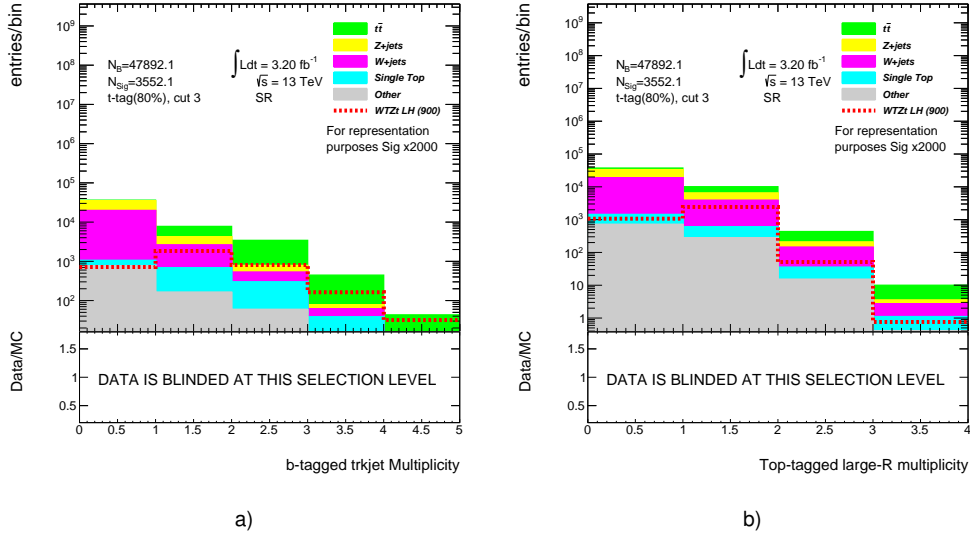
Figure 4.3: Plots showing the multiplicity of b-tagged track jets (before the demanding exactly one b-tag) and the multiplicity of top-tagged large-R jets (prior to requiring one top-tagged large-R jet), in a) and b), respectively.

working point - WP) are to be kept. The advantages of using track jets for b-tagging, instead of the more typical Calorimeter jets, include, for instance, a higher angular resolution in a busy environment (which our analysis is bound to have: boosted topology) and a lower sensitivity to pile-up, as outlined in [72]. The b-tagger used is the mv2c20 algorithm (makes use of multivariate methods to separate between b-jets from light and c-jet background [73]).

The last request of the basic selection is the demand of exactly one top-tagged large-R jet. The Top-tagging algorithm utilizes regularised requirements on two variables variables with little to no statistical correlation (as seen in 4.5a) and 4.5b)):

1. Large-R Jet Mass, corresponding to the invariant mass of calibrated large-R jets;

2. N-subjettiness Ratio τ_{32}, where $\tau_{32} = \tau_3/\tau_2$, and τ_N is the N-subjettiness of a large-R jet, which is defined as,

$$\tau_N = \frac{1}{d_0} \sum_k p_{Tk} \times \min(\delta R_{1k}, ...\delta R_{Nk}), \tag{4.1}$$

with p_{Tk} as the transverse momentum of constituent k, ΔR_{ik} is the distance between subjet i and constituent k and $d_0 = \sum_k p_{Tk} \times R$, where R is the jet radius parameter. The main purpose of the N-subjettiness is to express how well a given jet can be described by N or fewer subjets (the lower τ_N, the higher the probability of a given jet to be well described by N subjets). Thusly, asking for lower values of

FCUP | 54
Search for top quarks accompanied by missing energy in
hadronic topologies at the ATLAS experiment
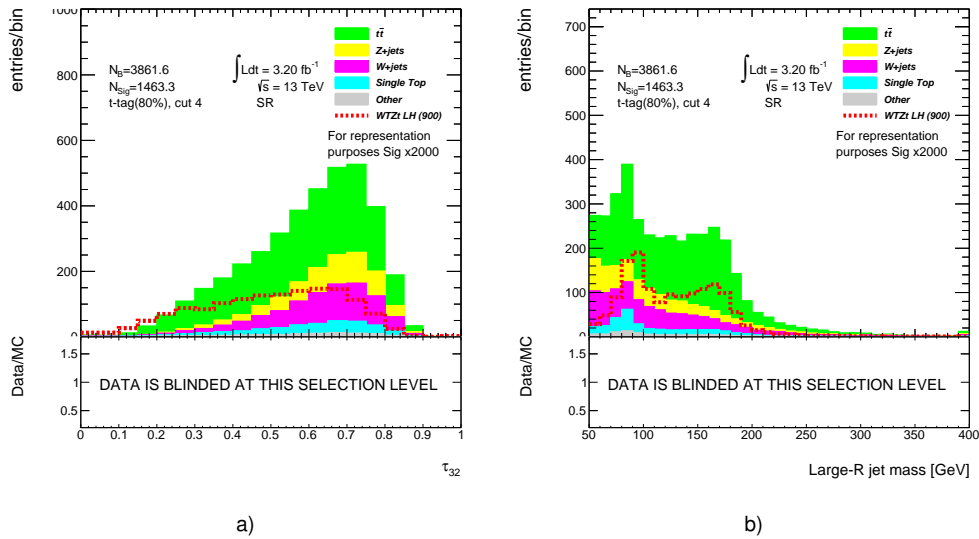
Figure 4.4: The two variables used for top-tagging: the N-subjettiness ratio τ_{32} in a), and the large-R jet mass in b).

the ratio τ_{32} equates to having a preference for events well-described by a three-pronged jet substructure.

Top-tagging using these two variables was first outlined in [75], and subsequently updated to $\sqrt{s} = 13$ TeV, in [74]. The regularised requirements are obtained by considering large-R jets in discrete p_T's and then trying to find what thresholds, at a given top-tagging efficiency (50 or 80%), would produce the best background rejection[2]. After having the optimal demands at each p_T, a curve can be drawn and afterwards, curve fitting can be used to produce a smooth curve, representative of the regularised requirement.

Since it was not clear which top-tagging WP would produce a better signal region, both 50 and 80% efficiencies were studied. A more definitive answer as to which one to use, will be attained in 4.5. In principle, a more stringent top-tagging (50%), would yield higher signal and $t\bar{t}$ purity, though at the price of loss of statistics. This can be see both in the yield tables, 4.2, and in the plots in 4.6, 4.10 and 4.11. The top-tagged large-R jet mass plots in 4.6 denote the major difference between the two efficiencies, as one can see a larger percentage of events at the mass peak corresponding to the W boson (partially boosted) at 80%, while at 50%, top-mass peak has a much higher concentration of events (fully boosted regime).

After the basic selection was implemented, one needed to look for new demands

---

[2]In [75] signal is tantamount to processes that generate hadronically decaying top quarks (for instance, $t\bar{t}$), and background is composed of multijet events;

Basic Selection (50% top-tagging)	Yields $\sqrt{s} = 13$ TeV, $\int \mathcal{L}dt = 3.2$ fb^{-1}
WTZt LH (900)	0.35 ± 0.01
$t\bar{t}$	968.72 ± 9.96
$Z + jets$	134.54 ± 4.55
$W + jets$	169.76 ± 4.48
Single Top	68.93 ± 1.56
Other	24.81 ± 0.83
Total bkg.	1366.76 ± 11.96
Basic Selection (80% top-tagging)	Yields $\sqrt{s} = 13$ TeV, $\int \mathcal{L}dt = 3.2$ fb^{-1}
WTZt LH (900)	0.64 ± 0.01
$t\bar{t}$	1605.99 ± 12.76
$Z + jets$	330.72 ± 5.60
$W + jets$	401.51 ± 5.80
Single Top	160.10 ± 2.38
Other	54.03 ± 1.46
Total bkg.	2552.35 ± 15.35

Table 4.2: Yield tables at basic selection level for the samples used in this analysis, either by using the 50 (left-hand-side table) or 80% (right-hand-side table) top-tagging working point.
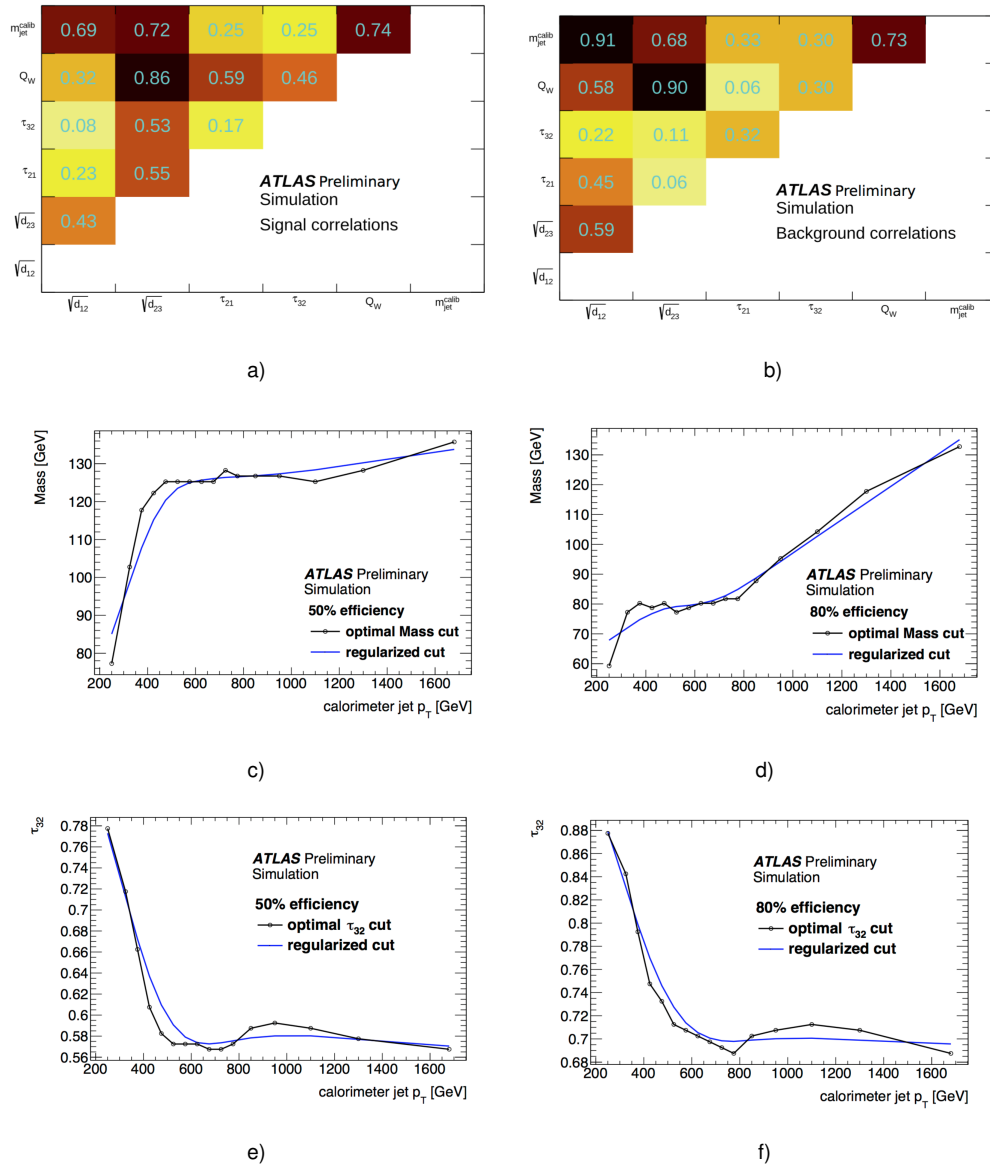
Figure 4.5: In a) and b) are present the correlations matrices for signal and background, displaying how correlated amongst themselves are the N-subjettiness ratios τ_{32} and τ_{12}, the splitting scales $\sqrt{d_{12}}$ and $\sqrt{d_{21}}$, the calibrated large-R jet mass, and the minimum dijet mass, from the three subjets, Q_w. The optimal mass (in c)) and d) for 50 and 80% top-tagging WP's, respectively) and tau_{32} (in e)and f), for both 50 and 80% efficiencies) requirements alongside their regularised versions, over a range of large-R jet p_T's. All figures taken from [74].

that diminished the main background's ($t\bar{t}$ processes) importance, while impacting the signal as little as possible. A demand that could be added to both the mono-top and the single production T selections would be the rejection of events where there is a small azimuthal angle between the leading Top-tagged Large-R jet and $\not{E}_T$ (ie. reject events
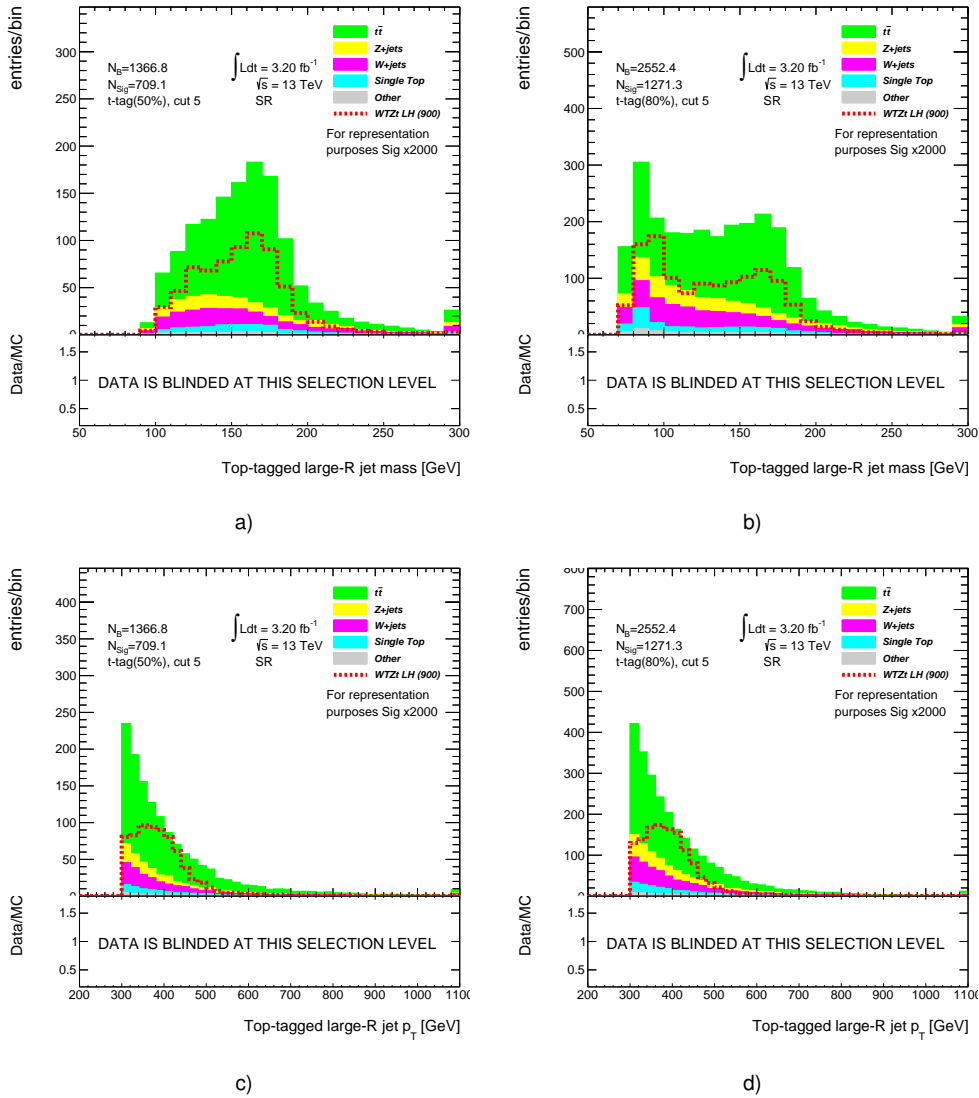
Figure 4.6: Plots showcasing the top-tagged large-R jet mass after applying either 50 or 80% top-tagging requirement in a) and b), respectively. Below each of the previous plots can be found the corresponding p_T distributions, in c) and d).

with $\Delta\phi(leading\ top - tagged\ largeR\ jet, \not{E}_T) < \pi/2)$ as evidenced by the plot in 4.7a). A forward jet requirement (at least one forward jet) is added only when considering single production of vector-like T, while no such requirement for mono-top.

As for the next two requirements, they were devised by trying to ascertain statistical correlations between variables. The two (uncorrelated) variables chosen were an azimuthal angle between $\not{E}_T$ and the closest small-R calorimeter jet, $\Delta\phi(smallR\ jet;\ \not{E}_T)$,

FCUP | 58
Search for top quarks accompanied by missing energy in
hadronic topologies at the ATLAS experiment
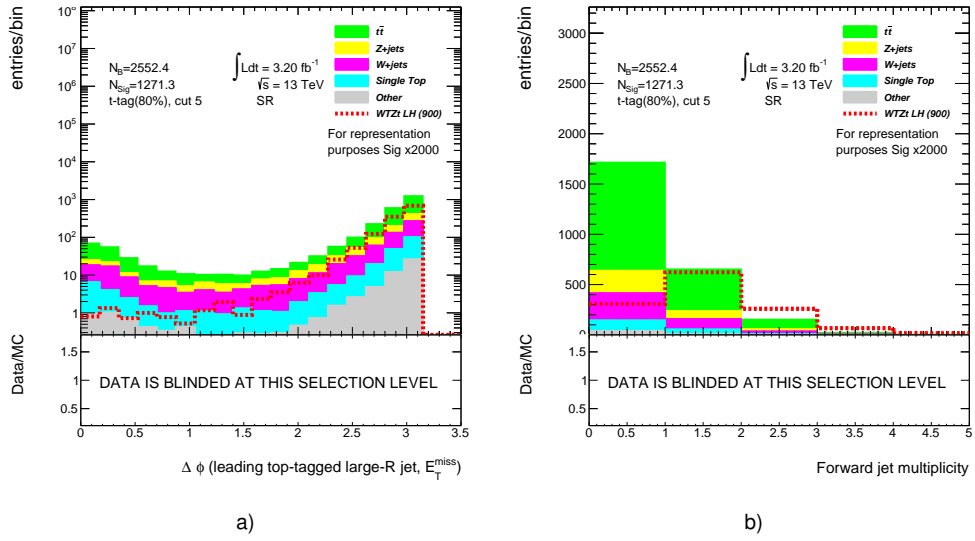
Figure 4.7: The distribution of the azimuthal angle between the leading top-tagged large-R jet and $\not{E}_T$ in a), and the forward jet multiplicity in b).

and an asymmetry defined as,

$$\Omega = \frac{\not{E}_T - p_{Tj1}}{\not{E}_T + p_{Tj1}} \tag{4.2}$$

where, p_{Tj1} is the transverse momentum of the leading top-tagged large-R jet.
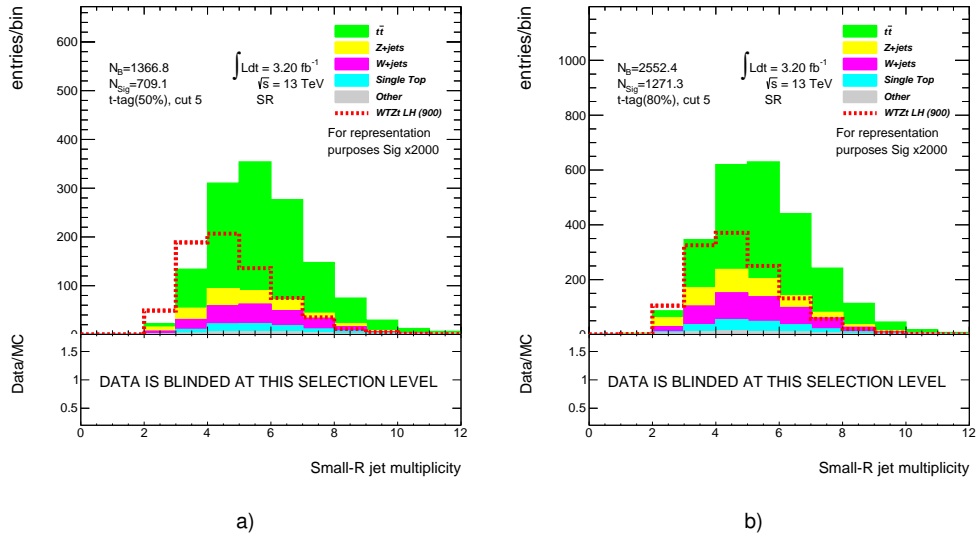
Figure 4.8: Small-R jet multiplicity after either the 50% or 80% top-tagging requirement, in a) and b), respectively.

The main idea is to reject events with low values of Ω (a consequence of $t\bar{t}$ being unable to provide large-R jets quite as boosted as the ones found in signal, and a
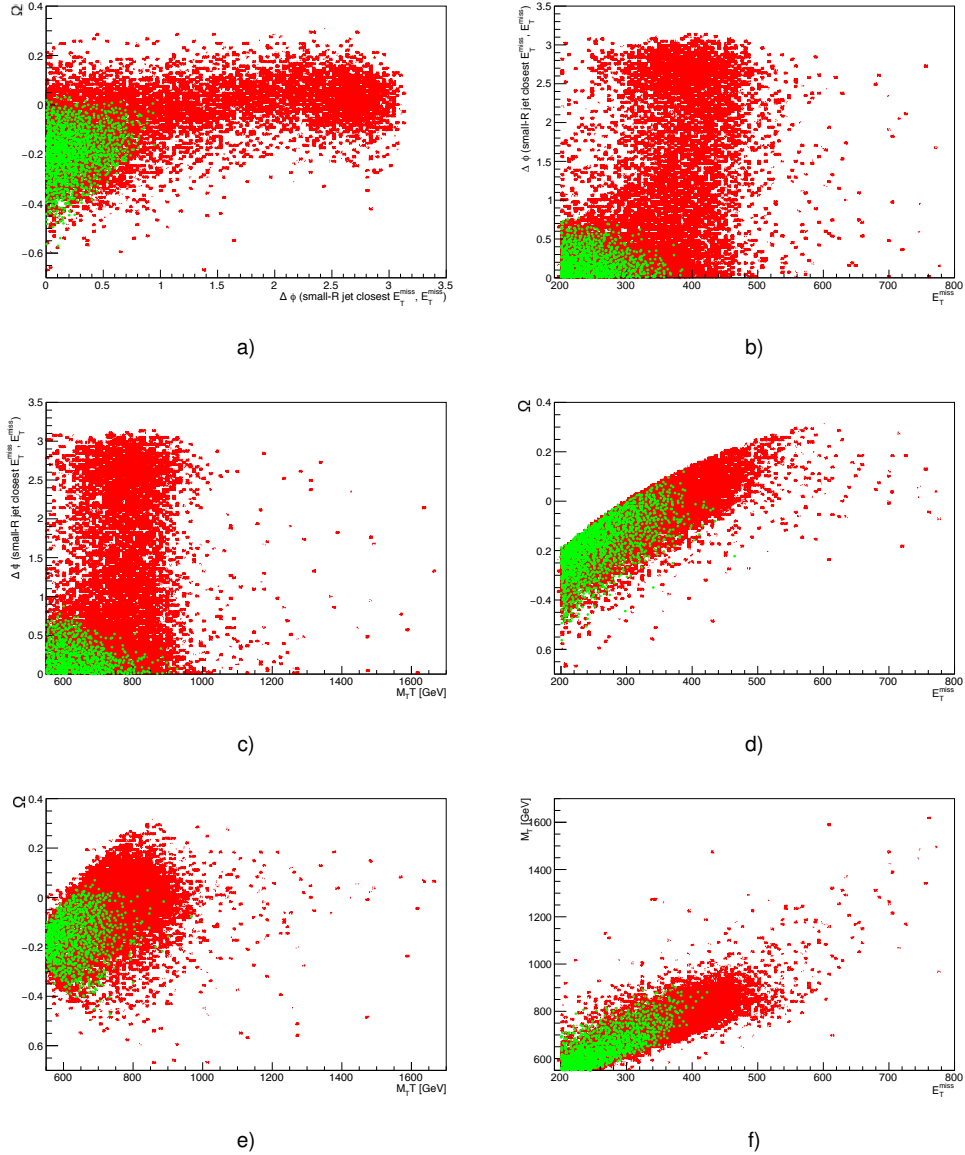
Figure 4.9: Scatter Plots showing the existence or lack thereof statistical correlations between several variables of interest: between $\Delta\phi(smallR\ jet\ \not{E}_T; \not{E}_T)$ and Ω (a)), $\not{E}_T$ b) and the mains discriminant variable, c), between Ω and $\not{E}_T$ (d)) and the transverse mass (e)), and lastly between $\not{E}_T$ and the transverse mass (f)). All distributions at basic selection level, assuming a top-tagging WP of 80%. The red regions represent signal processes and the green ones correspond to $t\bar{t}$ processes.
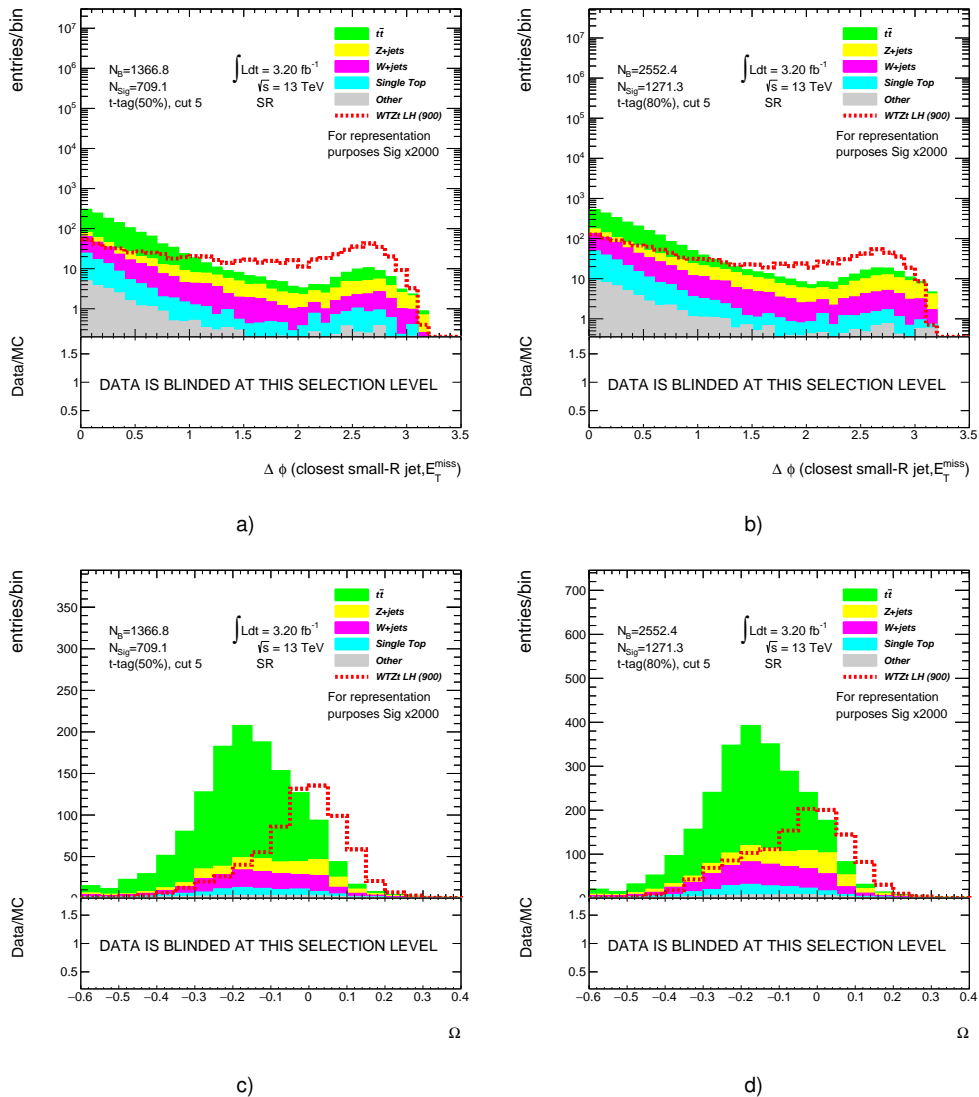
Figure 4.10: The distribution of the azimuthal angle between the small-R jet closest to $\not{E}_T$ and $\not{E}_T$, right after the top-tagging requirement and of Ω, for either 50, a) and c), or 80% efficiency, b) and d).

much lower $\not{E}_T$), and $\Delta\phi(smallR\ jet;\ \not{E}_T)$ (smaller angular distances expected in $t\bar{t}$ as most likely $\not{E}_T$ and the closest small-R calorimeter jet are both products of a W boson decay, whereas in single T $\not{E}_T$ will come from Z boson decays, and small-R jets may either be one of the decay products of the top quark or come from the single-production mechanism itself) in order to hinder $t\bar{t}$ concentration without affecting signal considerably. The reasoning behind the choice of these two variables can be justified by contemplating the scatter plot in 4.9a). How stringent the demands on these variables need to be, will be explored in subsection 4.5, when performing limit setting. A summary
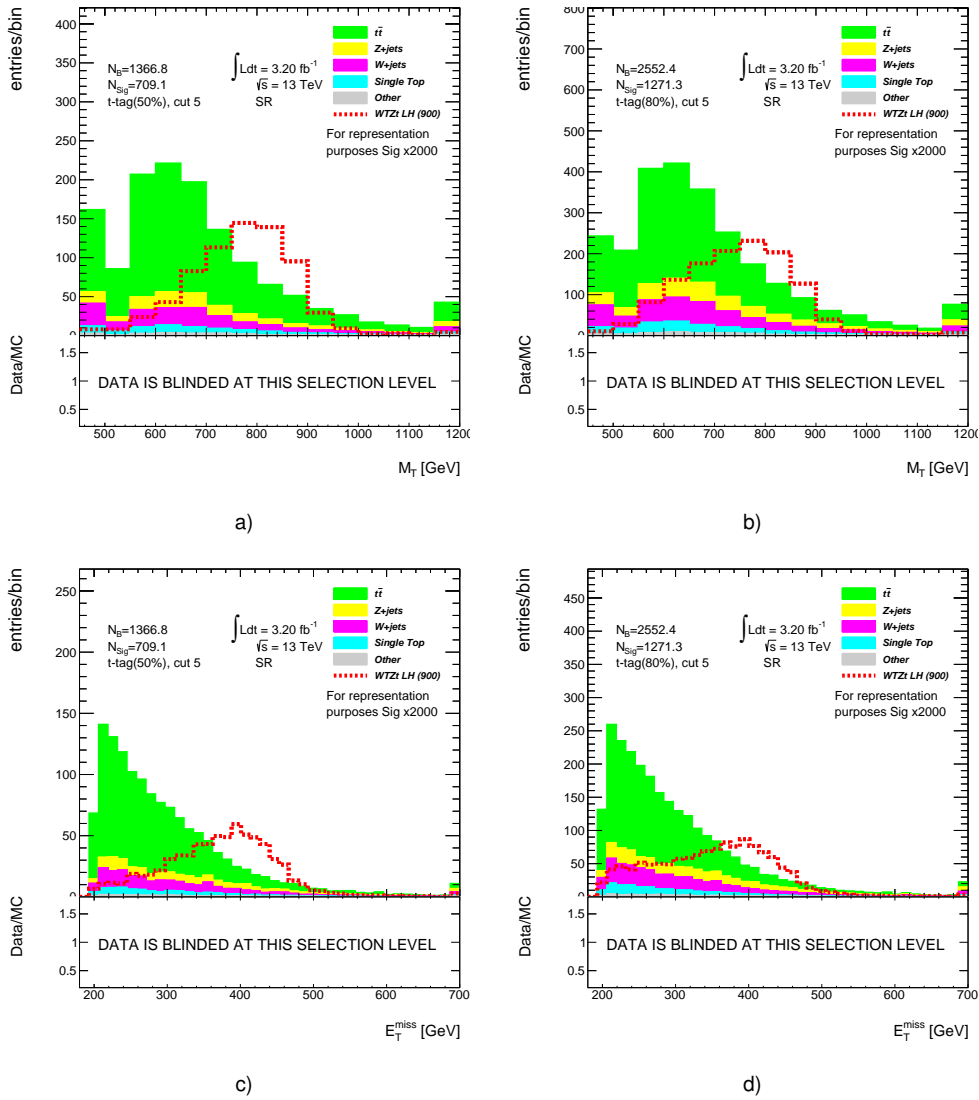
Figure 4.11: The distribution of the transverse mass of T, right after the top-tagging requirement, for either 50, a), or 80% efficiency, b); and the distribution of $\not{E}_T$ after either 50, c), or 80% top-tagging, d).

of the requirements applied on top of the basic selection is present in 4.3.

The requirement variations to be performed will involve rejecting events with $\Omega < x$, where $x \in [-0.4, 0.1]$, and with $\Delta\phi(smallR\ jet\ \not{E}_T; \not{E}_T) < y$, where $y \in [0.1, 0.7]$, in steps of 0.1, where extremal values of x and y are expected to be non-optimal. Both top-tagging WP's are to be considered, and both minimum threshold's of $\not{E}_T$ are to be used.

When it comes to upping the $\not{E}_T$ to 300 GeV, correlations with variables of interest (Ω and the discriminant variable used for limit setting, the soon-to-be defined transverse mass, as can be seen in 4.9d) and f)) attest that a higher $\not{E}_T$ might worsen the limit. The consequence of this demand on the two variables used for varying requirements can be seen in the plots of figure 4.12. However, if the Ω and the $\Delta\phi(smallR\ jet\ \not{E}_T; \not{E}_T)$ requirements fail to extricate large amounts of multijet background, the tighter demand becomes a necessity.

6	$\Delta\phi(leading\ top-tagged\ largeR\ jet, \not{E}_T) > \pi/2$
7	$\Omega > x,\ x \in [-0.4, -0.1]$
8	$\Delta\phi(smallR\ jet\ \not{E}_T; \not{E}_T) > y,\ y \in [0.1, 0.7]$
9	>=1 forward jet

Table 4.3: The four criteria applied after the basic selection.

The main discriminant variable to be used during limit setting will be the transverse mass of T, hereby defined as,

$$M_T^2 = M_{j1}^2 + 2\not{E}_T[E_{j1} - p_{Tj1} \cdot \cos(\Delta\phi)], \qquad (4.3)$$

where $j1$ is the Leading top-tagged large-R jet, M_{j1}, E_{j1} and p_{Tj1} are the Mass, Energy and transverse Momentum of $j1$, and $\Delta\phi$ is the azimuthal angle between $j1$ and $\not{E}_T$. The transverse mass is pictured in 4.11a) and 4.11b), at basic Selection level. The work done in this section was made possible by the New Physics Analysis (NPA) software package, developed in-house at LIP.

4.3.2 The Birth of a $t\bar{t}$ Control Region

The main background in this analysis is comprised of $t\bar{t}$ processes. A possibility in terms of trying to construct a $t\bar{t}$ region or even improving the previous signal region, would be to study the composition of $t\bar{t}$ and glean how much can be gained by changing lepton identification criteria.
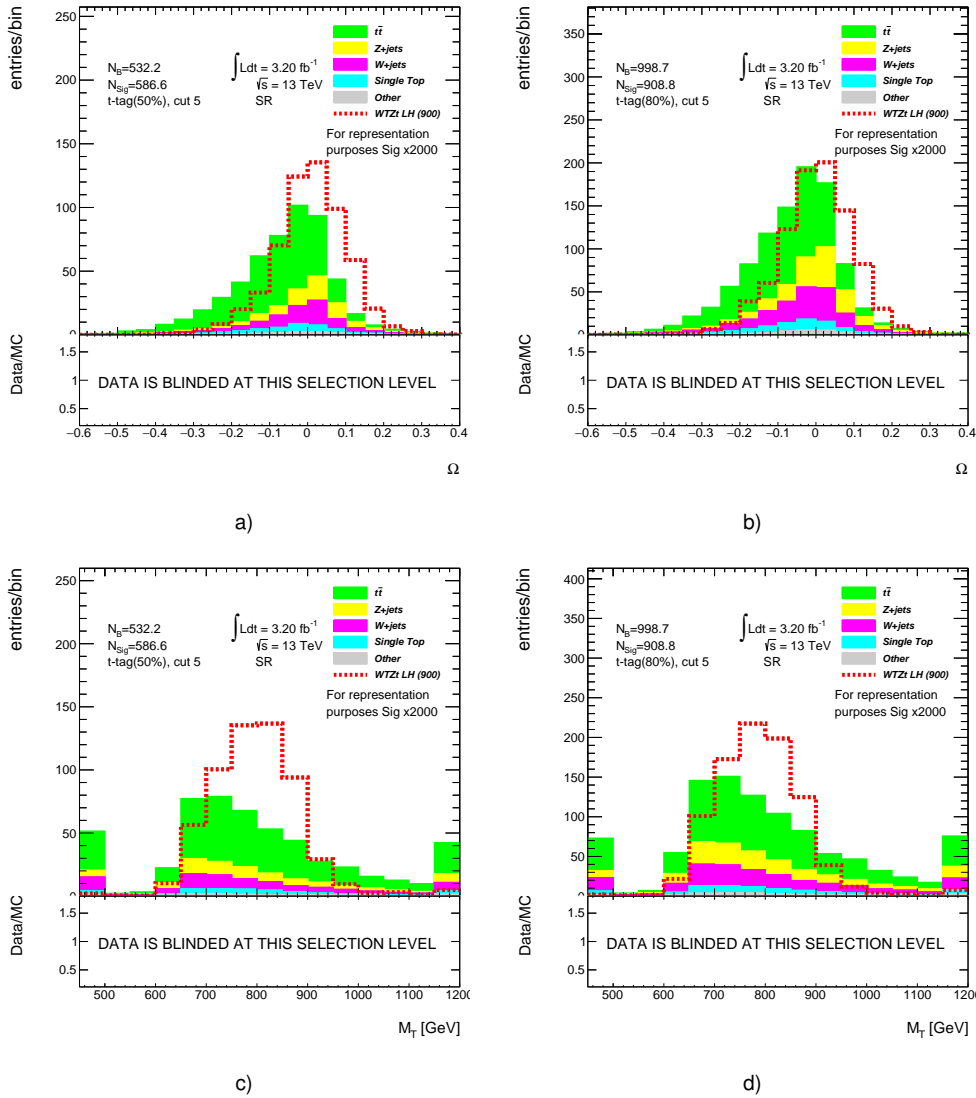
Figure 4.12: The plots for Ω and the transverse mass for a variation of the basic selection with a minimum $\not{E}_T$ of 300 GeV and top-tagging at 80% efficiency, in b) and d), or at 50% efficiency, in a) and c).

Semi-leptonic: 102069		Di-leptonic: 26687	e	μ	τ
eq:	24923	e	3800		
μq:	43392	μ	7128	2335	
τq	33754	τ	6381	4783	2260

Table 4.4: Number of semi-leptonic and di-leptonic events classified according to lepton species. Electron identification obeys the medium likelihood criteria from [64] and the loose muon identification criteria from [65].

FCUP | 64
Search for top quarks accompanied by missing energy in
hadronic topologies at the ATLAS experiment

In order to perform this study, it was necessary to process $t\bar{t}$ samples on the WLCG, with the pre-selection from section 4.1, albeit demanding exactly 0-leptons, and with the electron likelihood-based identification criteria either at medium or tight. Only semi-leptonic and di-leptonic $t\bar{t}$ samples were considered, as the all-hadronic $t\bar{t}$ sample amounts to a negligible number of events. Following successful completion of jobs, the NPA software package mentioned in the previous section was used to compute the un-weighted yields of the produced samples, looking at partonic history of each event. The main conclusion to be drawn is that since $t\bar{t}$ is mostly comprised of semi-leptonic and di-leptonic events, suggesting even after the 0-lepton requirement, suggesting misiden-tification of leptons. Lepton identification criteria do not produce a significant enough change in $t\bar{t}$ composition, as can be gleaned from comparing tables 4.4 and 4.5. As such, in the scope of this analysis, it doesn't seem like there is much to be gained from tinkering with these criteria. This type of work will have to be revisited, when combina-tion with other analysis is due.

SemiLeptonic: 100492		Di-Leptonic: 26365	e	μ	τ
eq:	24537	e	3727		
μq:	42665	μ	7057	2287	
τq	33290	τ	6330	4738	2226

Table 4.5: Number of semi-leptonic and di-leptonic events classified according to lepton species. Electron identification obeys the loose likelihood criteria from [64] and the loose muon identification criteria from [65].

After completing this study, comes the task of defining a control region for $t\bar{t}$ and prove whether or not, this background is well-modelled. Firstly, the cut pertaining to $\phi(\not{E}_T)$ can be kept for the same reasons devised at 4.3.1. When it comes to lepton multiplicity requirement, at the time of writing it is being kept at 0 leptons. In principle, a valid possibility would be to allow one or more leptons.

When it comes to the b-tagged track jet and the top-tagged large-R jet requirements one could look at the signal selection employed in 4.3.1 and at the conclusions drawn from the previous study on $t\bar{t}$ composition . Since it has been established that $t\bar{t}$ is mostly semi-leptonic, the demand of 1 top-tagged large-R jet seems logical (remember that for semi-leptonic $t\bar{t}$, one of the top quarks will decay hadronically, thus providing the three-pronged substructure the top tagging algorithm seeks, and the other will decay leptonically, thus not offering the typical boosted hadronic top topology). The presence of two b quarks from the decay of two top quarks, instead of only one, suggests re-
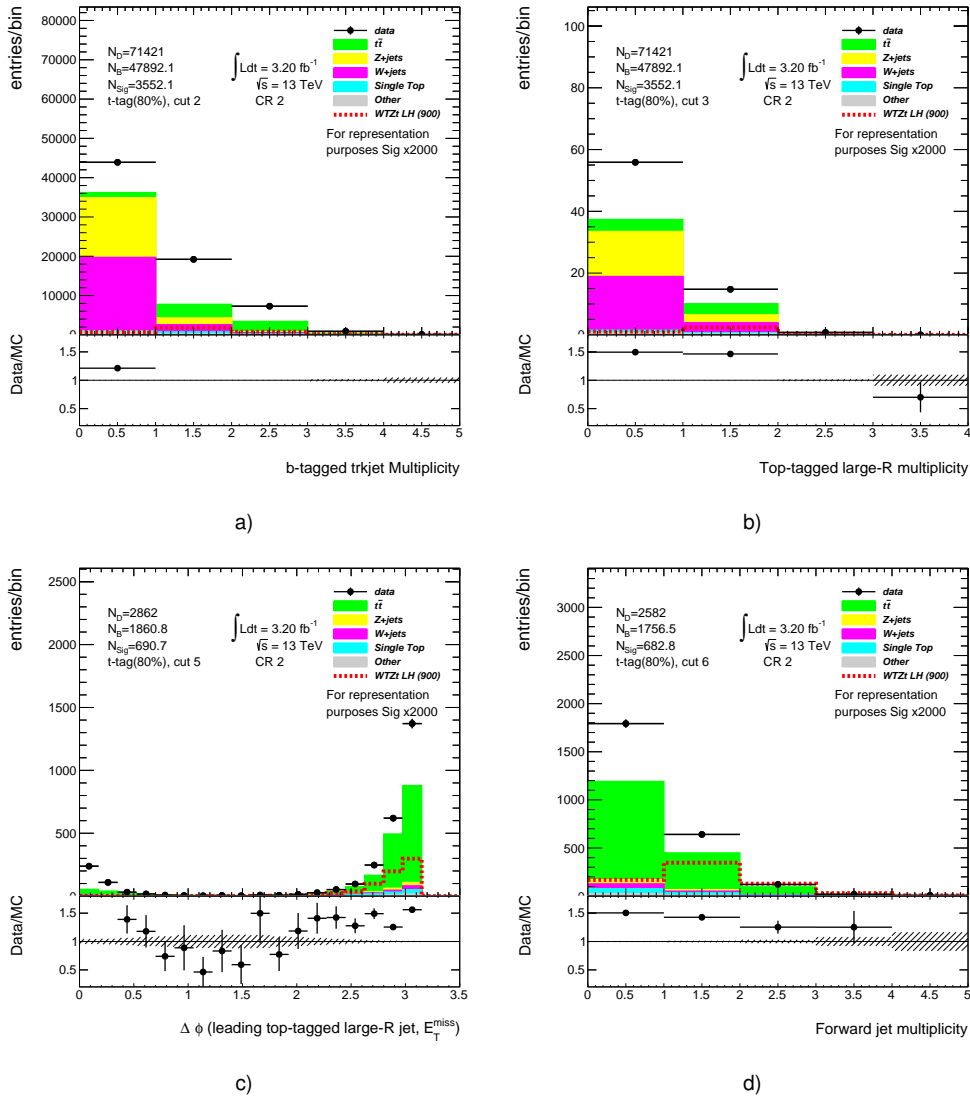
Figure 4.13: The distributions for the b-tagged track jet multiplicity right before the b-tagging requirement, a), the top-tagged large-R jet multiplicity before the top-tagging cut, at b), the azimuthal angle between the leading top-tagged large-R jet, right before it's cut upon, at c), and for the forward jet multiplicity, after the previously mentioned angular cut, at d).

questing at least two b-tagged track jets (b-tagged track jet and top-tagged large-R jet multiplicities before each requirement are displayed in 4.13a) and 4.13b)).

The azimuthal angle between the top-tagged large-R jet and $\not{E}_T$ being lower than $\pi/2$ doesn't seem to affect $t\bar{t}$ greatly and can thus be kept (see figure 4.13c)). The next two requirements ($\Omega < x$, $x \in [-0.4, 0.2]$ and $\Delta\phi(smallR\ jet\ closest\ \not{E}_T; \not{E}_T) < y$, $y \in [0.1, 0.7]$), are the mere reversal of two requirements which, in the signal region, served to preserve signal and hinder $t\bar{t}$. Do note that the optimal values of x and y will only be
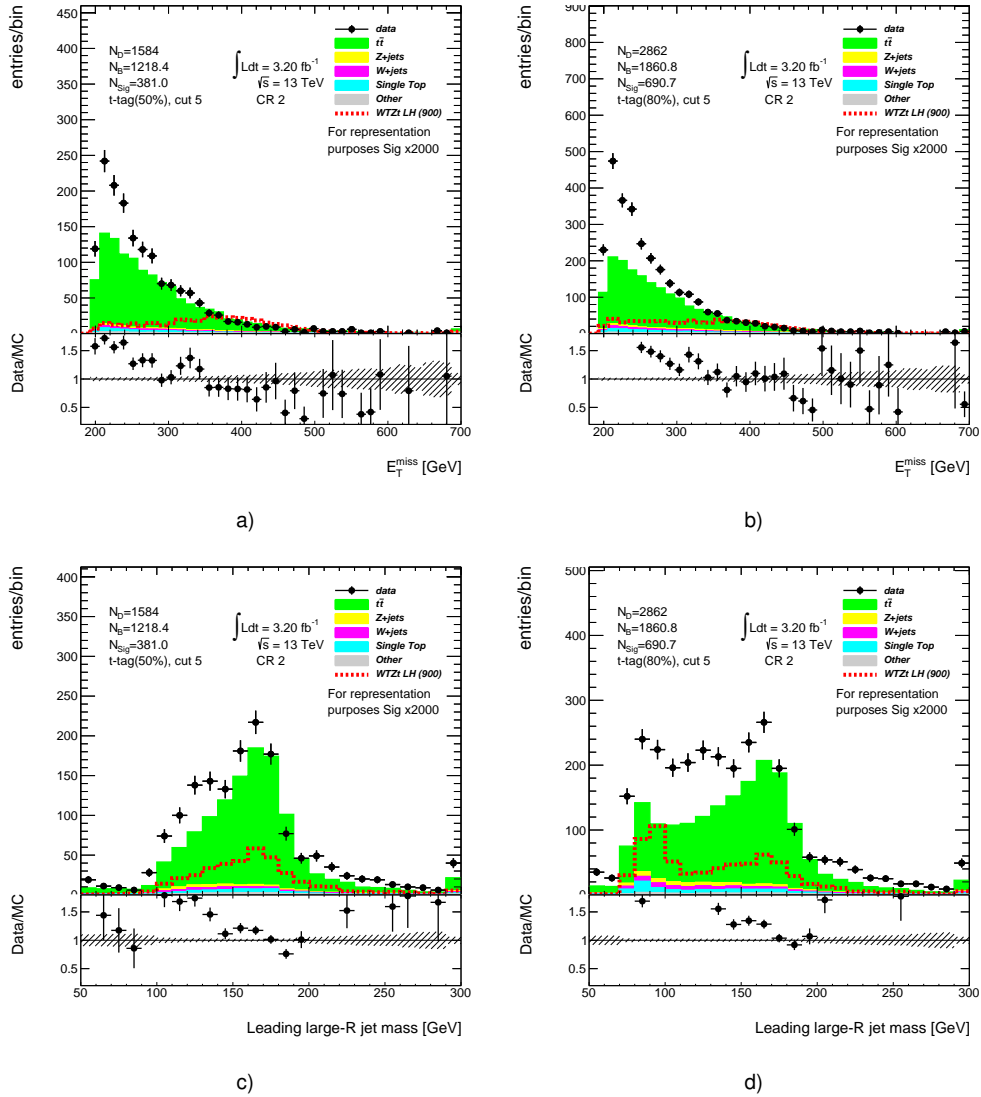
Figure 4.14: Distributions showcasing two relevant variables right before the two varying requirements are applied. The variables plotted are: $\not{E}_T$, at a) and b) and the mass of the leading large-R jet, at c) and d), for either 50% or 80% top-tagging WP's respectively.
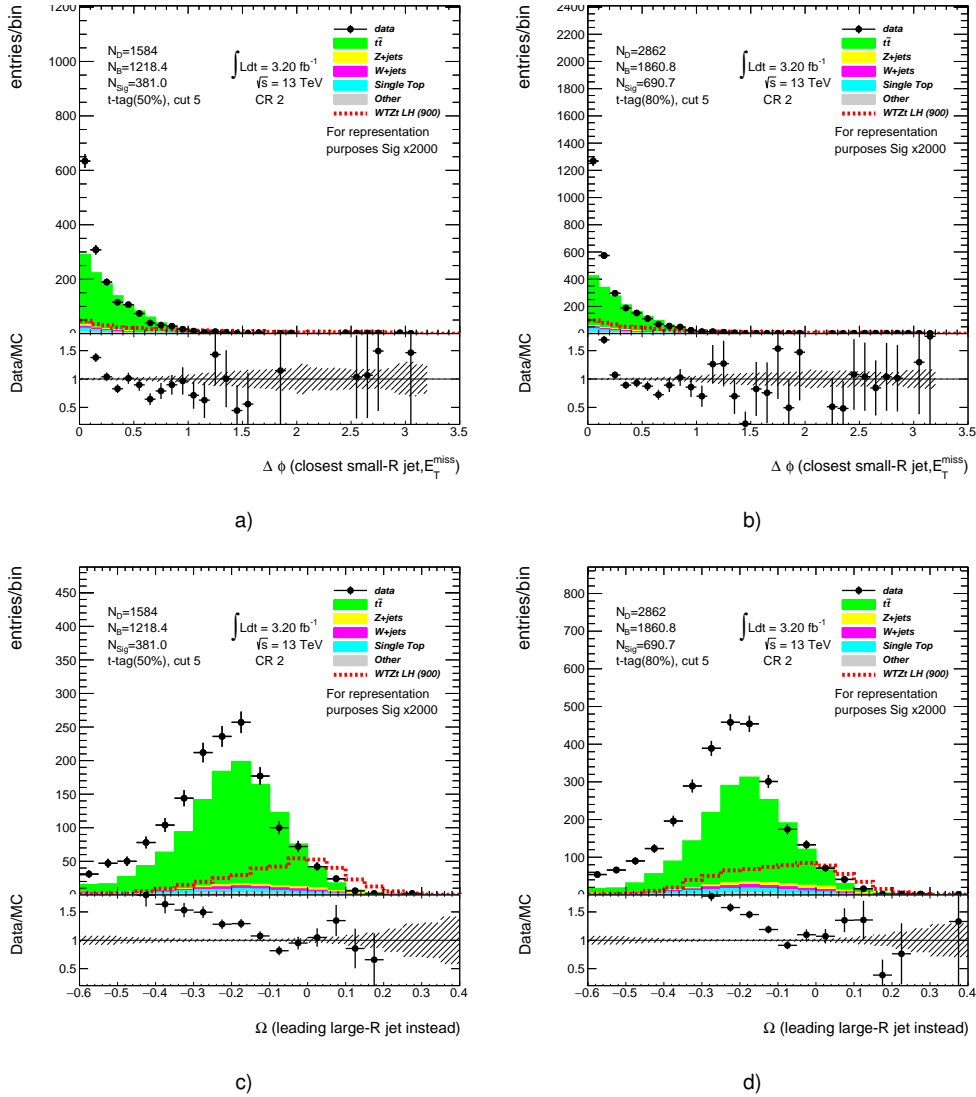
Figure 4.15: The upper panes showcase the azimuthal angle between the small-r calorimeter jet closest to $\not{E}_T$ and $\not{E}_T$ (a) and b), and the lower ones, Ω (c) and d)). Both variables obtained for either 50% (left-hand side) or 80% (right-hand side).

FCUP | 68
Search for top quarks accompanied by missing energy in
hadronic topologies at the ATLAS experiment

revealed in section 4.5. No forward jet cut will be utilised, as it would possibly imperil $t\bar{t}$ dominance (see figure 4.13d)). The yields for each top-tagging working point, before the two varying cuts can be found in table 4.6.

$t\bar{t}$ control region (50% top-tagging)	Yields $\sqrt{s} = 13$ TeV, $\int \mathcal{L} = 3.2$ fb^{-1}
WTZt LH (900)	0.19 ± 0.00
$t\bar{t}$	1082.38 ± 10.46
$Z + jets$	33.49 ± 1.11
$W + jets$	33.67 ± 0.81
Single Top	45.68 ± 1.26
Other	23.21 ± 0.54
Total bkg.	1218.41 ± 10.64
data	1584
$t\bar{t}$ control region (80% top-tagging)	Yields $\sqrt{s} = 13$ TeV, $\int \mathcal{L} = 3.2$ fb^{-1}
WTZt LH (900)	0.35 ± 0.01
$t\bar{t}$	1589.23 ± 12.62
$Z + jets$	71.42 ± 1.52
$W + jets$	73.04 ± 1.22
Single Top	92.72 ± 1.80
Other	34.39 ± 0.80
Total bkg.	1860.81 ± 12.92
data	2862

Table 4.6: Yield tables for the $t\bar{t}$ control region, right before the two varying demands.

Even without applying the last two requirements, one can already see good $t\bar{t}$ purity, albeit some signal contamination is still present. There exists reasonable Data/MC agreement around the top quark mass peak when one looks at the leading large-R jet mass, marred by disagreement present at lower masses (as can be seen from

1	0-lepton
2	Reject $\phi(\not{E}_T) \notin [0.7, 1.3]$ or $\phi(\not{E}_T) \notin [1.8, 2.2]$
3	$\not{E}_T > 200$ GeV
4	>= 2 b-tagged Track Jet (70% WP)
5	1 top-tagged Large-R Jet (80% WP)
6	$\Delta\phi(leading\ top-tagged\ largeR\ jet, \not{E}_T) > \pi/2$
7	$\Omega < x,\ x \in [-0.4, 0.2]$
8	$\Delta\phi(smallR\ jet\ closest\ \not{E}_T; \not{E}_T) < y,\ y \in [0.1, 0.7]$

Table 4.7: A prototype selection for the $t\bar{t}$ control region.

the bottom panes of 4.14). Agreement is also obtained at high values of $\not{E}_T$, high $\Delta\phi(smallR\ jet\ closest\ \not{E}_T; \not{E}_T)$ and Ω. Disagreement exists for low values of the two previously mentioned variables. This can be seen from the upper panes in 4.14 and from all distributions of 4.15. Do note that there seems to be more of a lack of agreement at the aforementioned variables when one considers the less stringent form of top-tagging (80%). Weather or not this behaviour can be explained by the multijet estimate will be revealed in the next sections.

The disagreement in the forward multiplicity seems larger at 0, when asking for 0 top tagged large-R jets, and at low $\Delta\phi(leading\ top-tagged\ largeR\ jet, \not{E}_T)$, as can be seen in 4.13c), respectively. These variables could form the basis of a multijet estimate. In order to have a method that functions both for mono-top and singly-produced T, the forward jet multiplicity will not be used to estimate multijet.

4.3.3 Data-driven multijet estimate

A background that is missing from the prior list of background samples consists of processes capable of generating several hadronic jets which have a strong possibility of emulating signal topology. Sonja Bartkowski of TU Dortmund is in charge of obtaining an estimate of this background. As the technique is still being developed, this is more a proof of concept, rather than a final estimate.

The current method is based upon the consideration of two variables with no statistical correlation and very little p_T dependency. The variables considered are the number of top-tagged jets demanded, and the azimuthal angle $\Delta\phi(leading\ largeR\ jet, \not{E}_T)$, which results in having four uncorrelated regions, one of them enriched in signal (region C, in 4.16), and then three auxiliary ones, poorer in signal contents (A, B and D

FCUP | 70
Search for top quarks accompanied by missing energy in
hadronic topologies at the ATLAS experiment
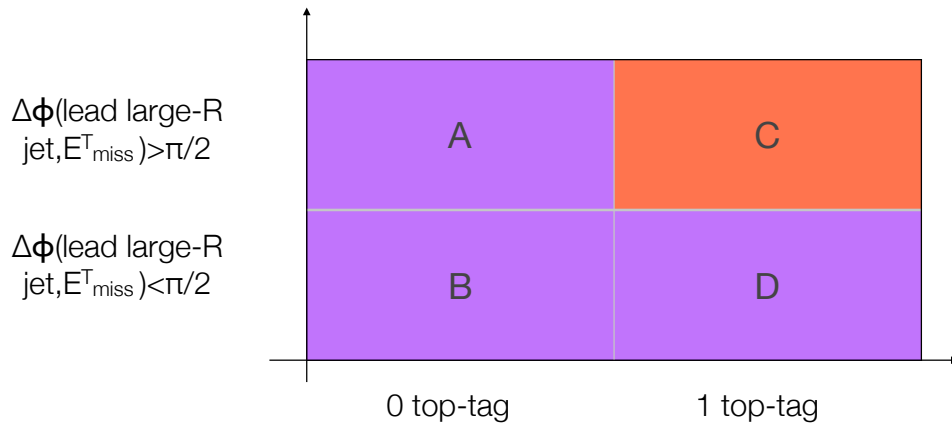
Figure 4.16: The four regions used for the multijet estimate, with region "C" being the signal region delineated previously, and the other three being auxiliary regions. All are independent amongst each other.

in 4.16), with either the angle cut reversed, with the top-tag requirement at 0, or both requirements, as indicated in 4.16.

As long as the four previous assumptions hold, then the ratio of the difference in data and background between A and D should be equal to ratio of the data/background difference between C and D. As such one can assume that,

$$C(multijet) = \frac{D(data \ - \ bkg)}{B(data \ - \ bkg)} \cdot A(data \ - \ bkg)$$

This essentially reads that shape estimation will depend on the region with only the top-tagging at 0 (region A at 4.16), while the scaling factor applied depends on the ratio between the region with the angle cut reversed (region D) and the region with both demands reversed (region B).

There is, however, a slight kink in this method: since all auxiliary regions are derived from the signal region, they all include a forward jet cut at the very end. This hampers the ability of the three auxiliary regions of having a higher purity of multijet background, which is somewhat contrarian to what was assumed above. This results in having low statistics in estimates produced for most variations. Solutions to this conundrum are still being worked on, at the time of writing. Eventually it will be necessary to design a control region enriched in multijet events, in order to offer some closure on whether or not this background is well-described by the estimate.

Do note that this method is also used to obtain an estimate of multijet for the $t\bar{t}$ control region, by replacing the signal region in 4.16 by the control region, and assuming the auxiliary regions require at least two b-tagged track-jets.
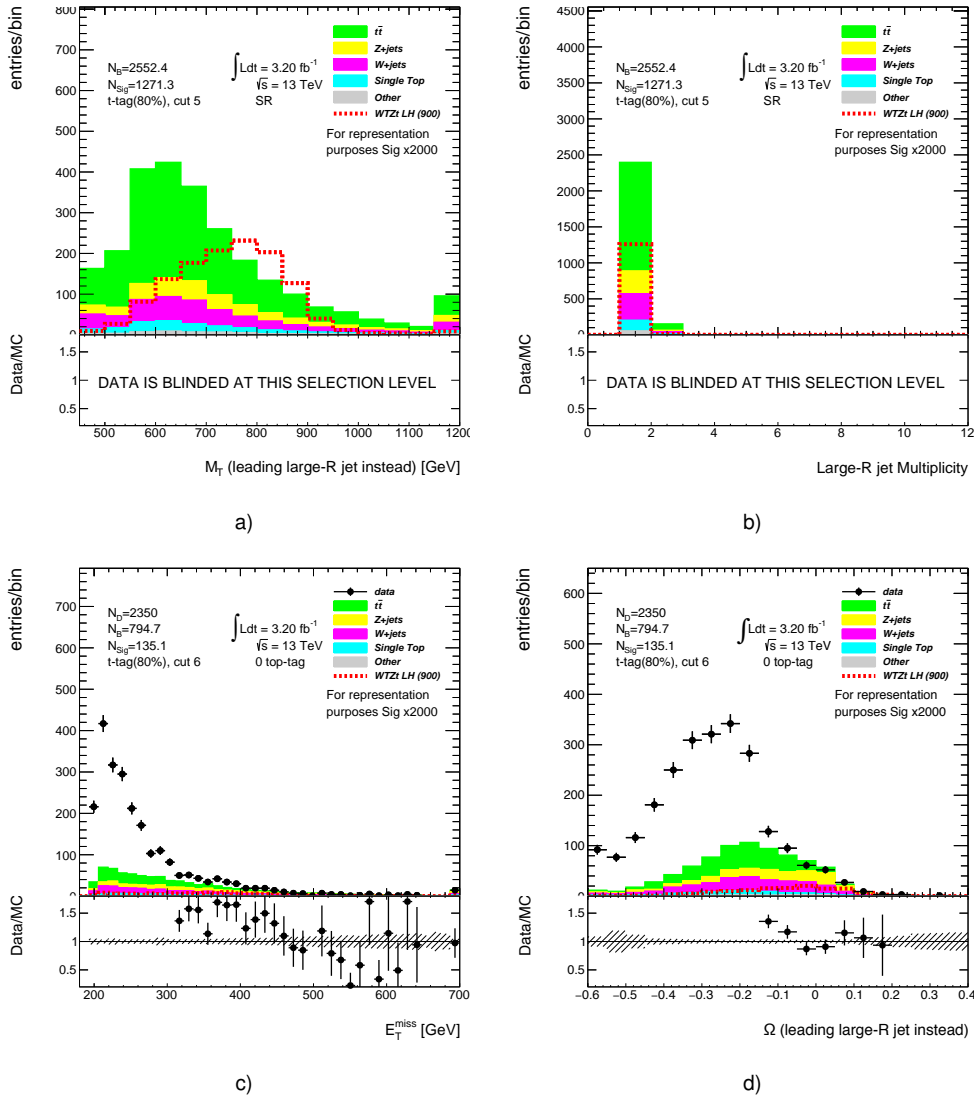
Figure 4.17: On the top-row two panes showing two variables at basic selection level: the transverse mass calculated without any top-tagging requirement on the large-R jet used in it's definition, a), and the large-R jet multiplicity, b). On the two lower panes, the $\not{E}_T$ and Ω distributions in the multijet auxiliary region with the top-tagging requirement at 0 (used for shape estimation), in c) and d) respectively.

This estimate also introduces a slight change in the previous regions (signal and $t\bar{t}$), in order to be able to apply the 0 top-tagged large-R jet requirement and actually calculate a transverse mass afterwards, one should change the definitions of the transverse mass, the asymmetry and the first azimuthal angular cut, to utilize the leading large-R jet and not the leading top-tagged large-R jet. In principle, as can be seen from the plots in 4.17 this should not be an issue.

FCUP | 72
Search for top quarks accompanied by missing energy in
hadronic topologies at the ATLAS experiment

4.4   Multijet in practice

Now let's a have a look at how the multijet estimate behaves in the signal region. From the plots in 4.18 and 4.19 a few conclusions can be drawn: the estimate seems to have a preference for lower values of Ω and $\Delta\phi(smallR\ jet\ closest\ \not{E}_T; \not{E}_T)$ which signifies that the two varying cuts will be effective at eliminating multijet, whether at 80 or 50% efficiency top-tagging. Since the multijet estimate also occupies the region of low $\not{E}$, meaning the harsher $\not{E}$ requirement will also be, as expected, effective at extricating multijet. It seems this background also peaks at lower values of the main discriminant variable (transverse mass).

Of course, it is imperitive to understand exactly how well the estimate behaves. Since the method is still under active development, no multijet control region is yet drawn, however one could look at data/background agreement in the $t\bar{t}$ control region to unveil how the method seems to perform. The plots detailling the performance of the multijet estimate when applied to the $t\bar{t}$ control region are available in 4.20 and 4.21. The method seems to work well in the $\not{E}_T$, Ω and $\Delta\phi(smallR\ jet\ closest\ \not{E}_T; \not{E}_T)$ distributions where good data/background agreement is achieved (a welcome improvement from the corresponding distributions in 4.14 and 4.15). However, the estimate does tend to misbehave in the leading large-R jet distribution, as proven by the disagreement seen in 4.20c) and 4.20d). Since the estimate is in a state of constant flux (being improved and refined on a daily basis), this might become fully understood/mitigated in the near future.

Another curious detail, is the fact that multijet seems a bit more prevalent at 80% top-tagging, both in the signal region, and in the $t\bar{t}$ control region. This could be a consequence of the 0 top-tagged auxiliary regions both having more statistic if one considers 50% (more specifically region B, as denoted in 4.16, since A is mainly used for shape estimation).

4.5   Limit setting

In the beginning of the chapter, it was mentioned that the goal of every analysis would be distinguish between the SM background only hypothesis from the signal plus background hypothesis. In more scientific terms, these can be named:

1. Null Hypothesis, H_0, indicates the possibility of having signal and background (s+b), as such being consistent with this hypothesis, would indicate discovery;
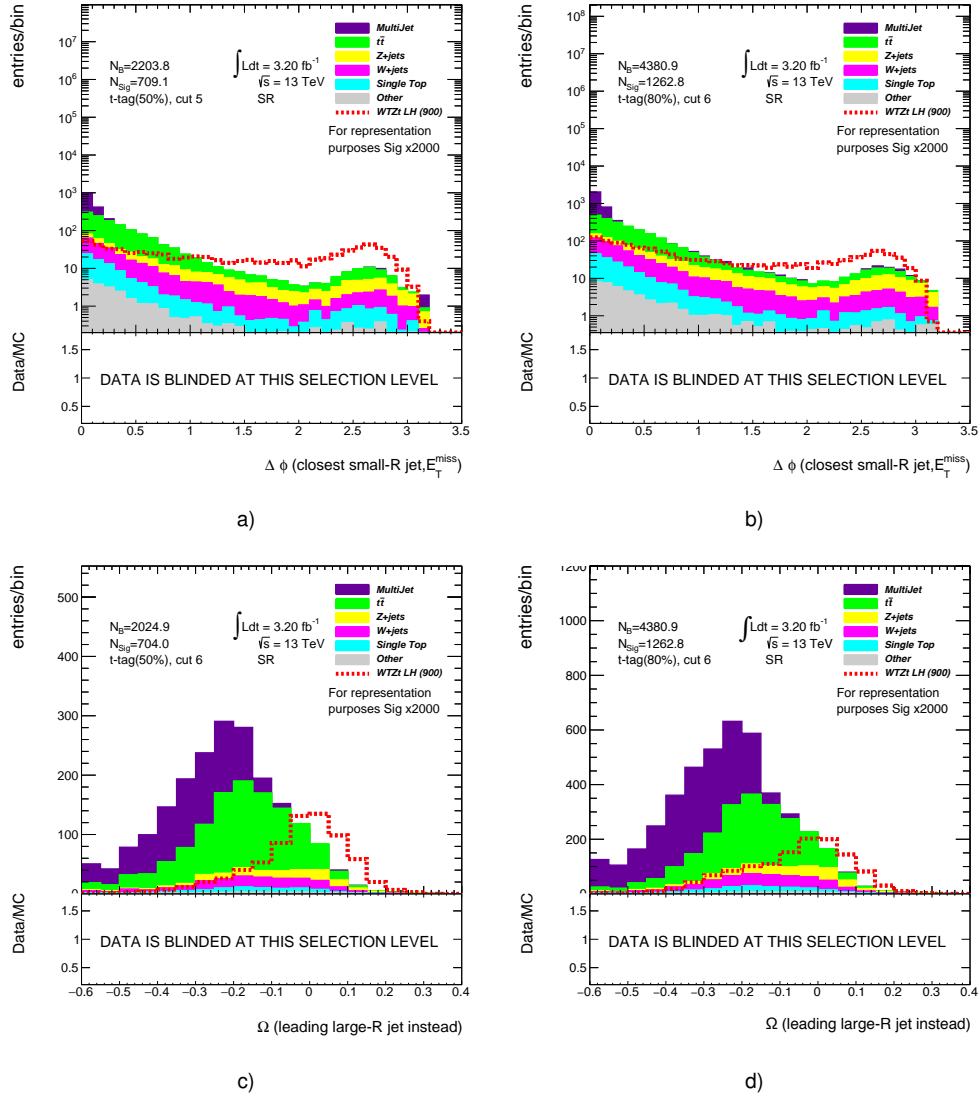
Figure 4.18: Plots pertaining to a few variables of interest: the asymmetry Ω, in a) and b),and the azimuthal angle $\Delta\phi(smallR\ jet\ closest\ \not{E}_T; \not{E}_T)$, atc) and c). All left-hand side panes correspond to a top-tagging WP of 50%, whereas all right-hand side ones correspond to 80%. All distributions are at the $\Delta\phi(leading\ top-tagged\ largeR\ jet, \not{E}_T)$ cut level.
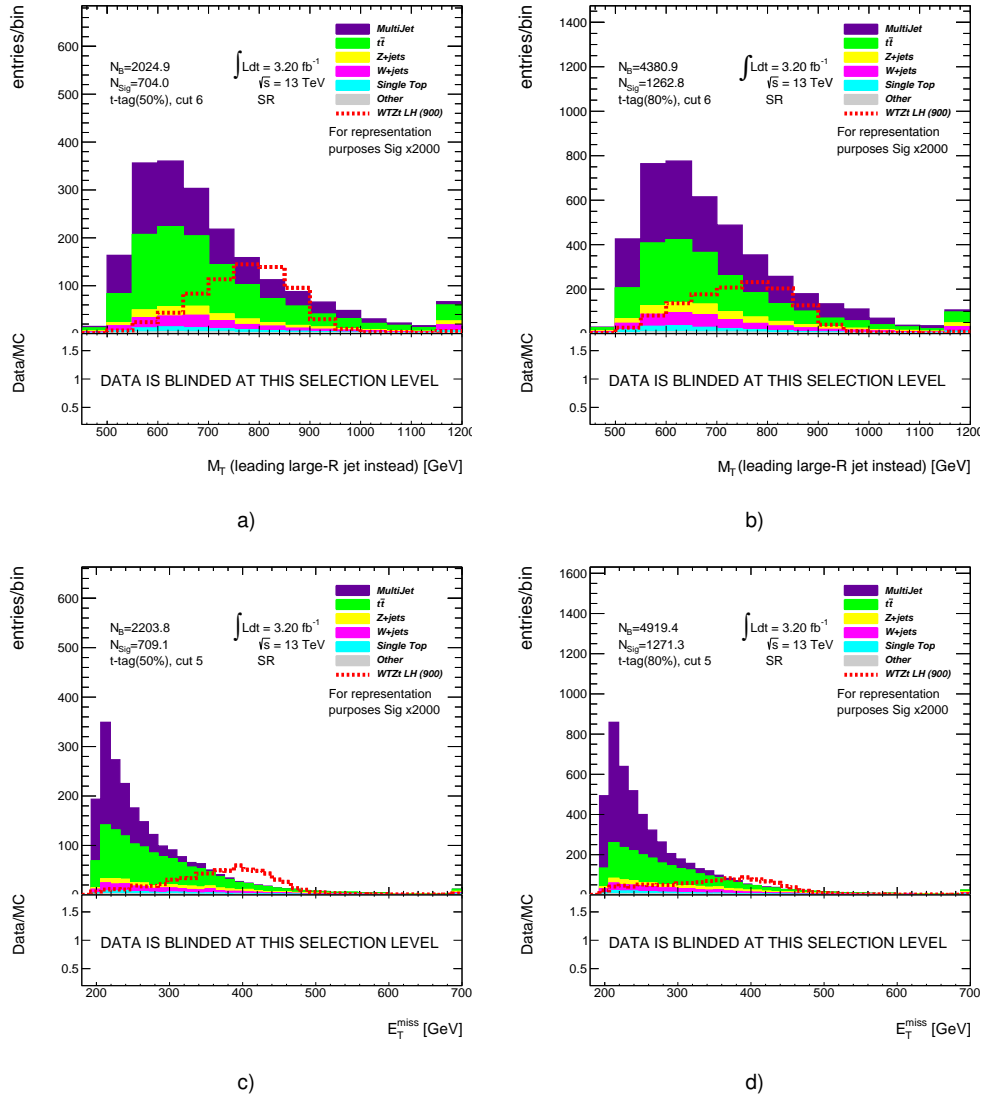
Figure 4.19: A few panes with the distributions for transverse mass, in a) and b), and $\not{E}_T$, in c) and d), for a minimum $\not{E}_T$ of 200 GeV, for 50% and 80% top-tagging efficiency, respectively. All distributions are at the $\Delta\phi(leading\ top-tagged\ largeR\ jet, \not{E}_T)$ cut level.
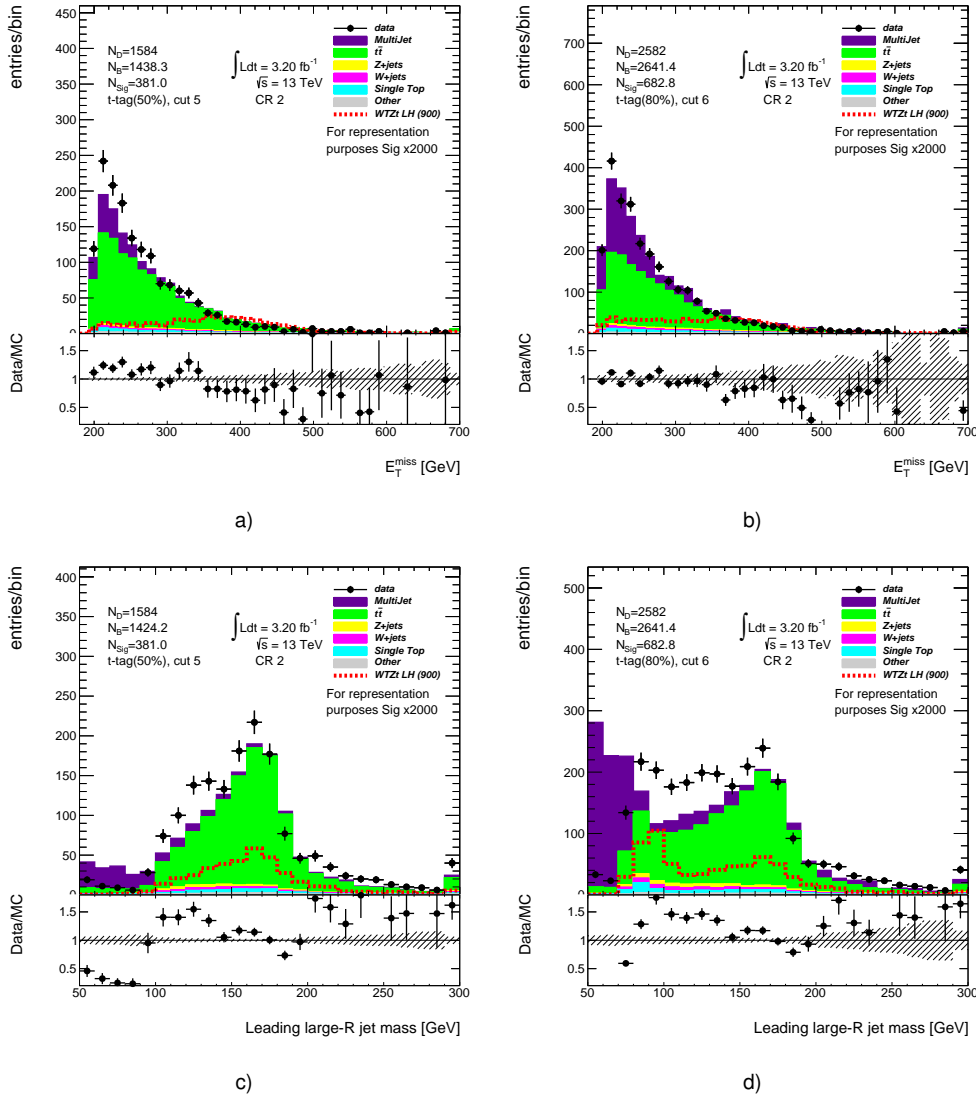
Figure 4.20: Plots showcasing a few relevant variables, such as $\not{E}_T$, in a) and b) and the leading large-R jet mass, in c) and d), for either 50% or 80% top-tagging. All plots at cut6 level (right before the two varying demands) in the $t\bar{t}$ control region.
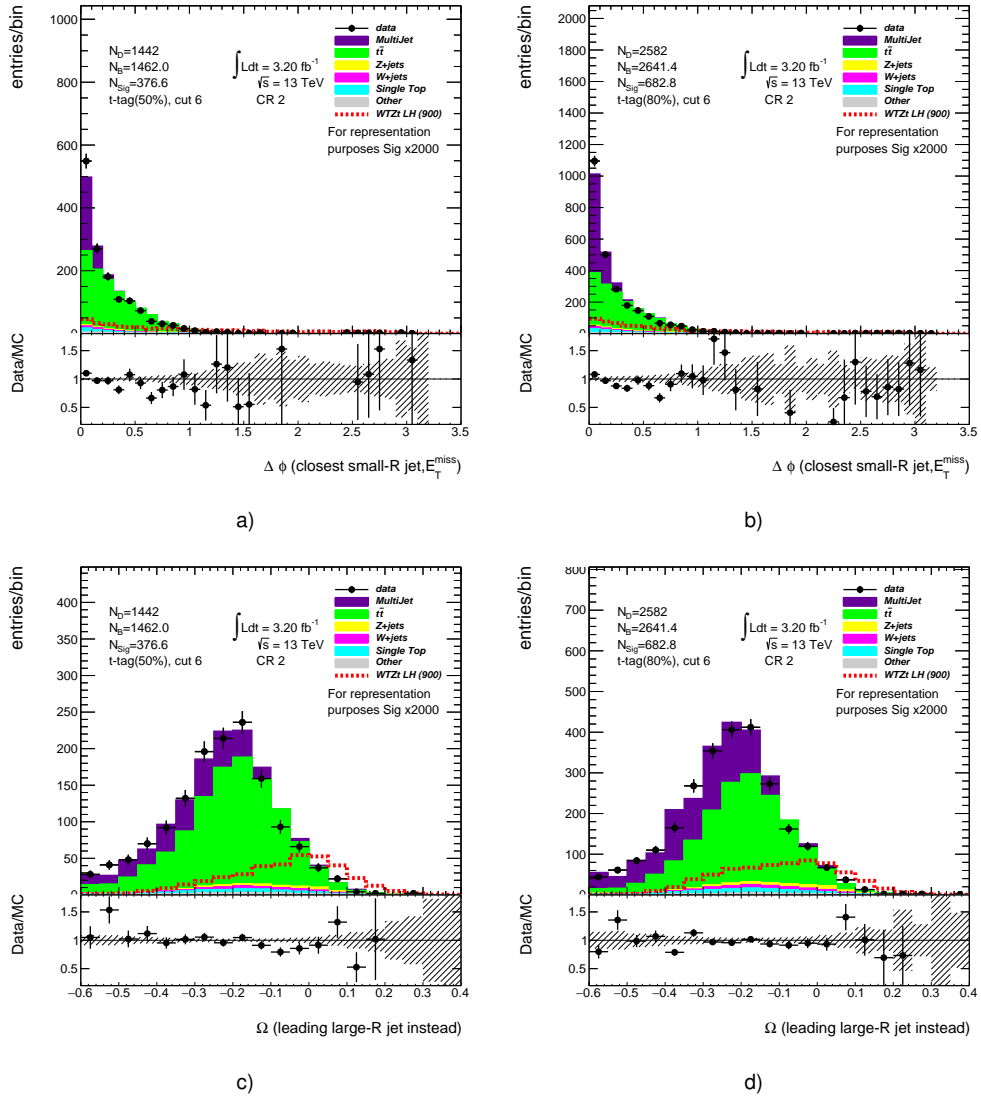
Figure 4.21: A few panes with distributions for the azimuthal angle between the small-R jet closest to $\not{E}_T$ and $\not{E}_T$, in a) and b), and the asymmetry Ω, in c) and d), for 50% and 80% top-tagging WP's, respectively. All plots at cut6 level (right before the two varying requirements) in the $t\bar{t}$ control region.

2. Alternate Hypothesis, H_1, corresponds to the presence of SM processes (b).

Accepting the Null hypothesis when the alternate one corresponds to truth, essentially means incurring in a "false positive", or Type-I error. The opposite can also happen: not admitting the presence of signal processes would result in a "false negative" (Type-II) error. In order to reveal how sensitive our analysis is to signal processes, one can calculate an upper expected exclusion limit on the cross-section for the production of the single T, assuming decay to hadronic top and invisible Z boson (BR at 100%). This will reveal, for a given acceptance of a Type-I error, α, exactly down to what cross-section, can we exclude the presence of signal events. Notice that the limit mentioned in the previous sentence is described as being expected, which means that exclusion of the null hypothesis, is evaluated taking into account only background and signal, without any observable data (blind analysis). Normally, the two possibile values of α would allow for the possibility of a false positive with 5% probability. The method used to obtain the 95% exclusion limits in particle physics is know as the CL_s (Confidence Level for signal). In order to explain what CL_s entails, let's begin by defining a p-value. Given the Null-Hypothesis, H (consistent with signal and background events, s+b), the p-value is the probability of finding if a given test statistic q_μ of a parameter μ (on which one sets a limit) than a test statistic q_{exp} consistent with the background expectation. This implies the following definition,

$$p_{s+b} = \int_{q_{exp}}^{\infty} G(q_\mu|q_{s+b})dq, \tag{4.4}$$

where $G(q_\mu|q_{s+b})$ is some hypothesis distribution. The gist of the method consists in rejecting a given signal hypothesis if,

$$p_{s+b} < \alpha, \tag{4.5}$$

where α is the Type-I error mentioned above, which is equal (by convention) to 5%. CL_{s+b} is equal to 1-α, thus 95%.

There is a small catch in using CL_{s+b}: it might occur, that whenever a small downward fluctuation of signal with respect to background happens, one will end up excluding the background only model. The way to avoid this is to normalize CL_{s+b} to background, hence,

$$CL_s = \frac{CL_{s+b}}{1 - CL_b}, \tag{4.6}$$

where, the background only CL is defined as,

$$CL_b = \int_{q_{exp}}^{\infty} G(q_\mu|q_b)dq. \tag{4.7}$$

FCUP | 78
Search for top quarks accompanied by missing energy in
hadronic topologies at the ATLAS experiment

Without further ado, the 95% CL_s^{exp} upper limit for the single left-handed T signal, produced through W boson vertex, with a mass of 900 GeV, minimum $\not{E}_T$ of 200 GeV, before and after the forward jet cut are presented in figures 4.22a) and 4.22b). Bear in mind that these are preliminary limits, as the multijet estimate is not yet complete and no systematic uncertainties are included. Since we currently do not possess any generated mono-top resonant signal (and since mono-top resonant is kinematically similar to single T, assuming of course a mass of 900 GeV for the scalar resonance, and a small negligeble mass for f_{met}, the invisible fermion), the "before-the-forward-jet-cut" scenario will act as a proxy for the time-being. The lowest exclusion limit will present us with the optimal cut values for the signal region.

For single T (after the forward jet cut), the lowest cross-section limit is present at $\Omega > -0.2$ and $\Delta\phi(smallR\ jet\ closest\ \not{E}_T; \not{E}_T) > 0.7$, and is valued at 0.33 pb, with bands of $+1\sigma = 0,46$, $-1\sigma = 0.23$, $+2\sigma = 0,67$ and $-2\sigma = 0.17$.

For mono-top (using single T before the forward jet cut), the lowest cross-section limit is present at $\Omega > -0.3$ and $\Delta\phi(smallR\ jet\ closest\ \not{E}_T; \not{E}_T) > 0.7$, being valued at 0.44, with bands of $+1\sigma = 0.67$, $-1\sigma = 0.32$, $+2\sigma = 0.93$ and $-2\sigma = 0.64$.

Comparing the prior two limits, one can see the lowest limit obtained appears after the forward jet cut. In other regions, such as for example low Ω, low $\Delta\phi(smallR\ jet\ closest\ \not{E}_T; \not{E}_T)$ the difference is even more accentuated (which signals a heightened presence of both $t\bar{t}$ and multijet backgrounds). The main conclusion to draw is that there is something to be gained by applying the forward jet cut.

	Signal Region I	Signal Region II	$t\bar{t}$ Control Region
1	0-lepton		
2	Reject $\phi(\not{E}_T) \notin [0.7, 1.3]$ or $\phi(\not{E}_T) \notin [1.8, 2.2]$		
3	$\not{E}_T > 200$ GeV		
4	1 b-tagged Track Jet (70% WP)	>= 2 b-tagged Track Jet (70% WP)	
5	1 top-tagged Large-R Jet (80% WP)		
6	$\Delta\phi(leading\ toptagged\ large-R\ jet, \not{E}_T) > \pi/2$		
7	$\Omega > -0.3$	$\Omega > -0.2$	$\Omega < -0.2$
8	$\Delta\phi(smallR\ jet\ closest\ \not{E}_T; \not{E}_T) > 0.7$		$\Delta\phi(smallR\ jet\ closest\ \not{E}_T; \not{E}_T) < 0.7$
9		>=1 forward jet	

Table 4.8: The selections for the two proposed signal regions (signal region I for mono-top, signal region II for single T) and for the $t\bar{t}$ control region;
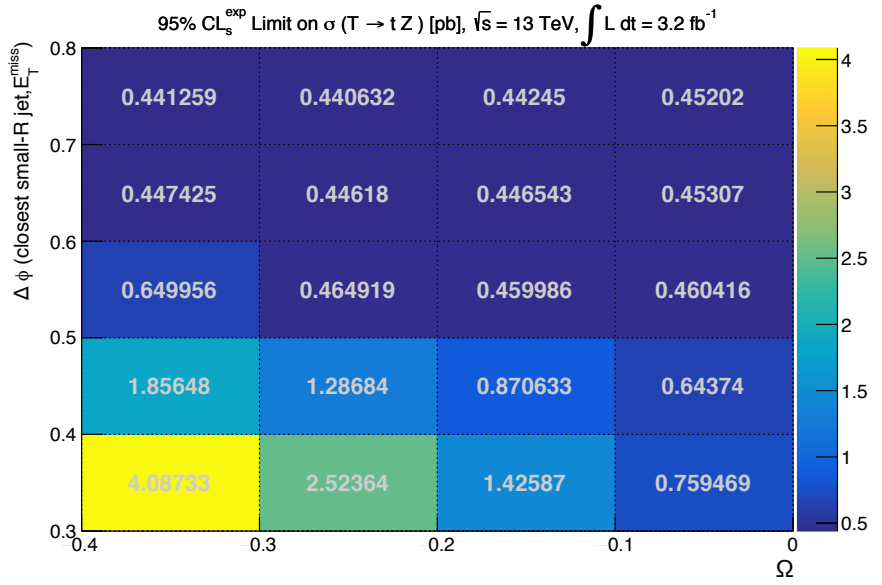
a)
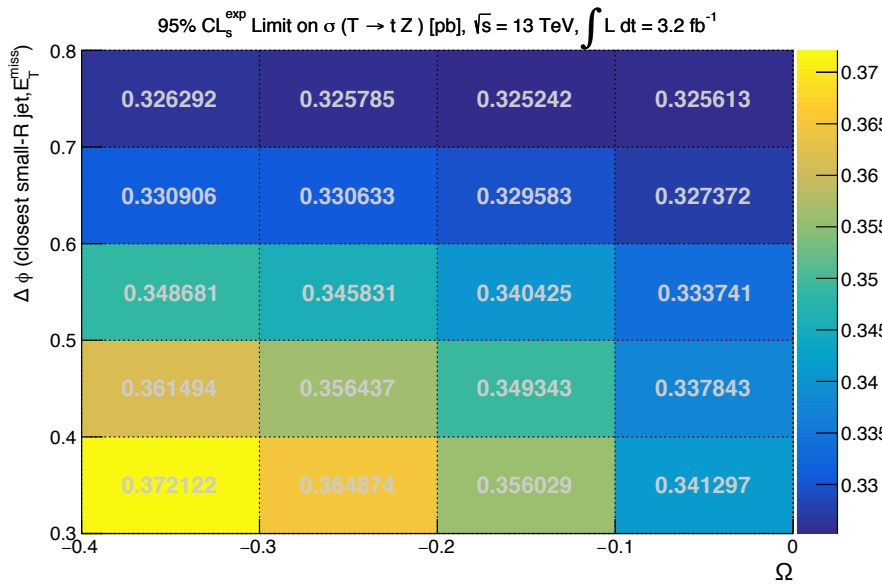
b)

Figure 4.22: The expected cross-section limits σ, using 95% C.L. for the singly produced T, through the production vertex using W boson cross-section, before ,a), and after ,b), the foward jet cut, assuming a minimum threshold $\not{E}_T$ of 200 GeV and a top-tagging WP of 80%.

The upper limits for mono-top proxy and single T with a minimum $\not{E}_T$ of 300 GeV are available at figures 4.23a) and 4.23b). Both are marginally higher than their $\not{E}_T = 200$ GeV counterparts, which indicates there isn't much of a necessity to maintain a

FCUP | 80
Search for top quarks accompanied by missing energy in
hadronic topologies at the ATLAS experiment
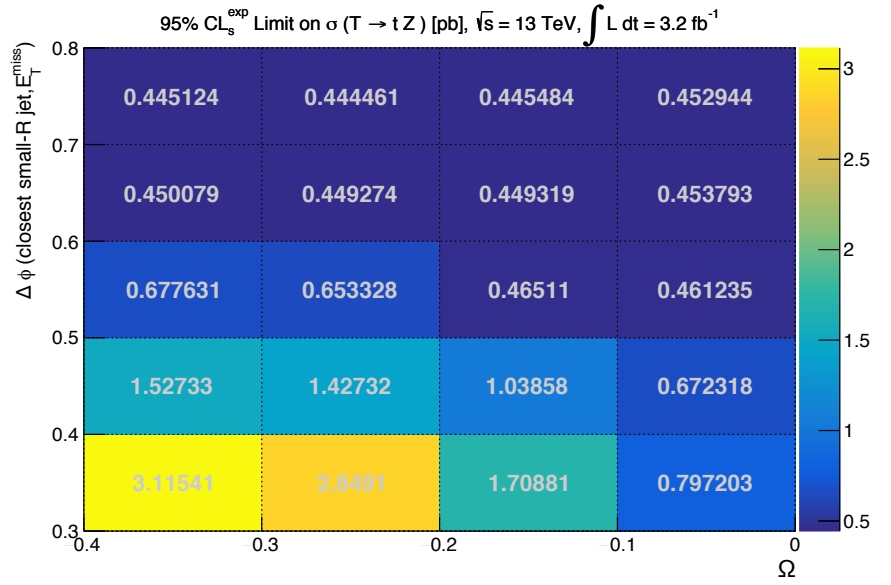
a)
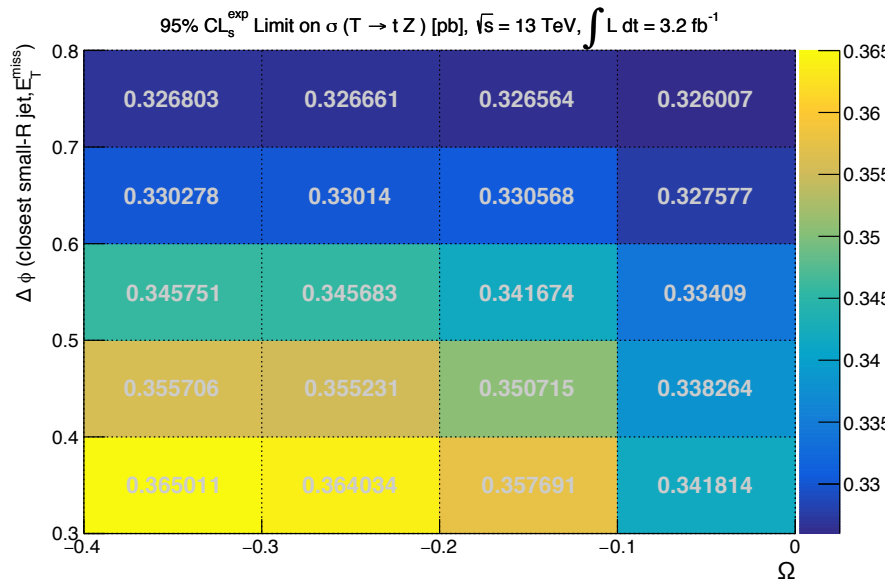
b)

Figure 4.23: The expected cross-section limits σ, using 95% C.L. for the singly produced T, through the production vertex using W boson cross-section, before ,a), and after ,b), the forward jet cut, assuming a minimum threshold $E\!\!\!/_T$ of 300 GeV and a top-tagging WP of 80%.

higher $E\!\!\!/_T$ threshold. Also interesting to observe: in extremal regions (for instance at low Ω and low $\Delta\phi(smallR\ jet\ closest\ E\!\!\!/_T; E\!\!\!/_T)$) the limits tend to be lower than with a smaller $E\!\!\!/_T$ perhaps indicating of prevalence of multijet in such region. The

FCUP | 81
Search for top quarks accompanied by missing energy in
hadronic topologies at the ATLAS experiment
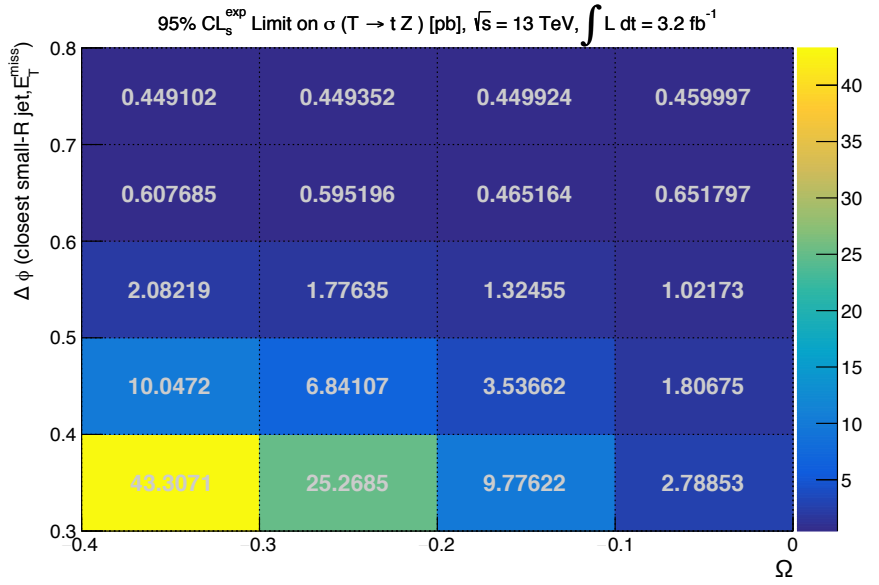
a)
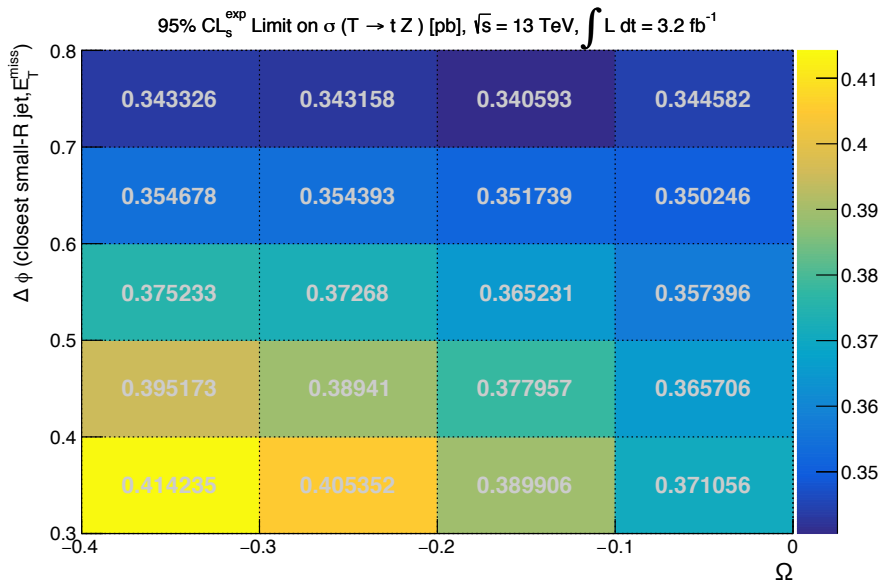
b)

Figure 4.24: The expected cross-section limits μ, using 95% C.L. for the singly produced T, through the production vertex using W boson cross-section, before ,a), and after ,b), the foward jet cut, assuming a minimum threshold $\not{E}_T$ of 200 GeV and a top-tagging WP of 50%.

limit obtained for the single T case is 0.33 pb with bands $+2\sigma = 0,67$, $+1\sigma = 0.47$, $-1\sigma = 0.24$ and $-2\sigma = 0,18$. Before the forward jet demand, the limit obtained is valued at 0.44 pb, with bands $+2\sigma = 0.94$, $+1\sigma = 0.68$, $-1\sigma = 0.32$ and $-2\sigma = 0.24$.
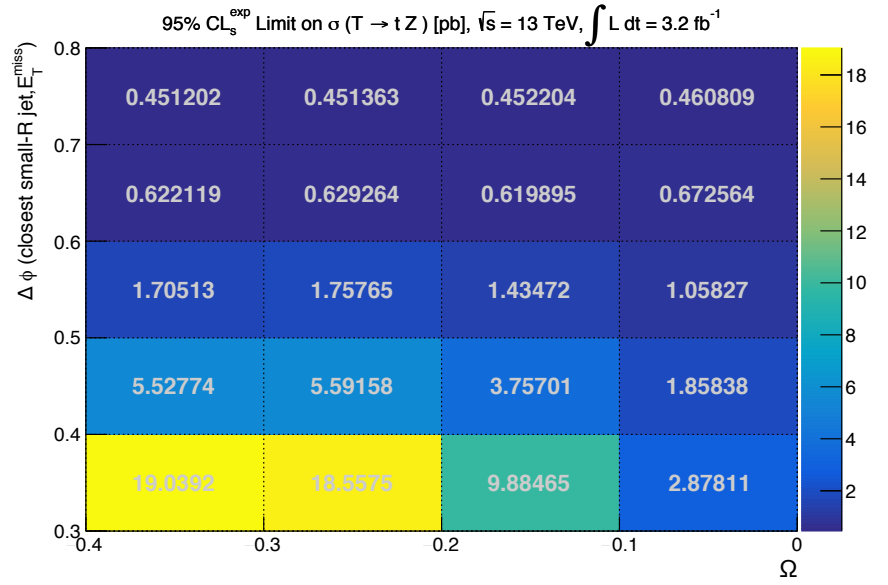
a)
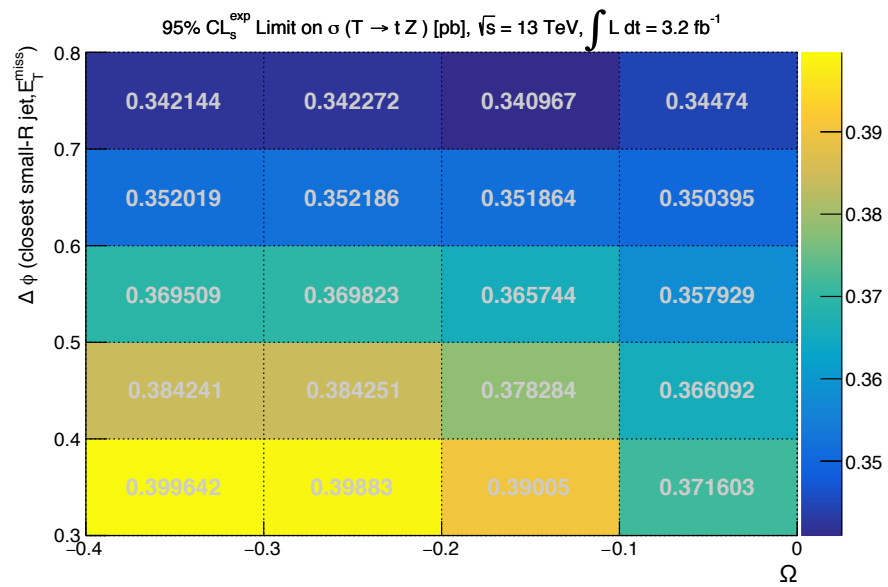
b)

Figure 4.25: The expected cross-section limits μ, using 95% C.L. for the singly-produced left-handed T signal, before ,a), and after ,b), the foward jet cut, under the assumption of a minimum threshold $\not{E}_T$ of 300 GeV and a top-tagging efficiency of 50%.

The limit setting machinery was also set into motion for the top-tagging WP of 50% with a minimum $\not{E}_T$ of 200 GeV, as can be seen in 4.24a) and 4.24b). These limits seems to be narrowly worse than their 80% counterparts, which is probably a side-
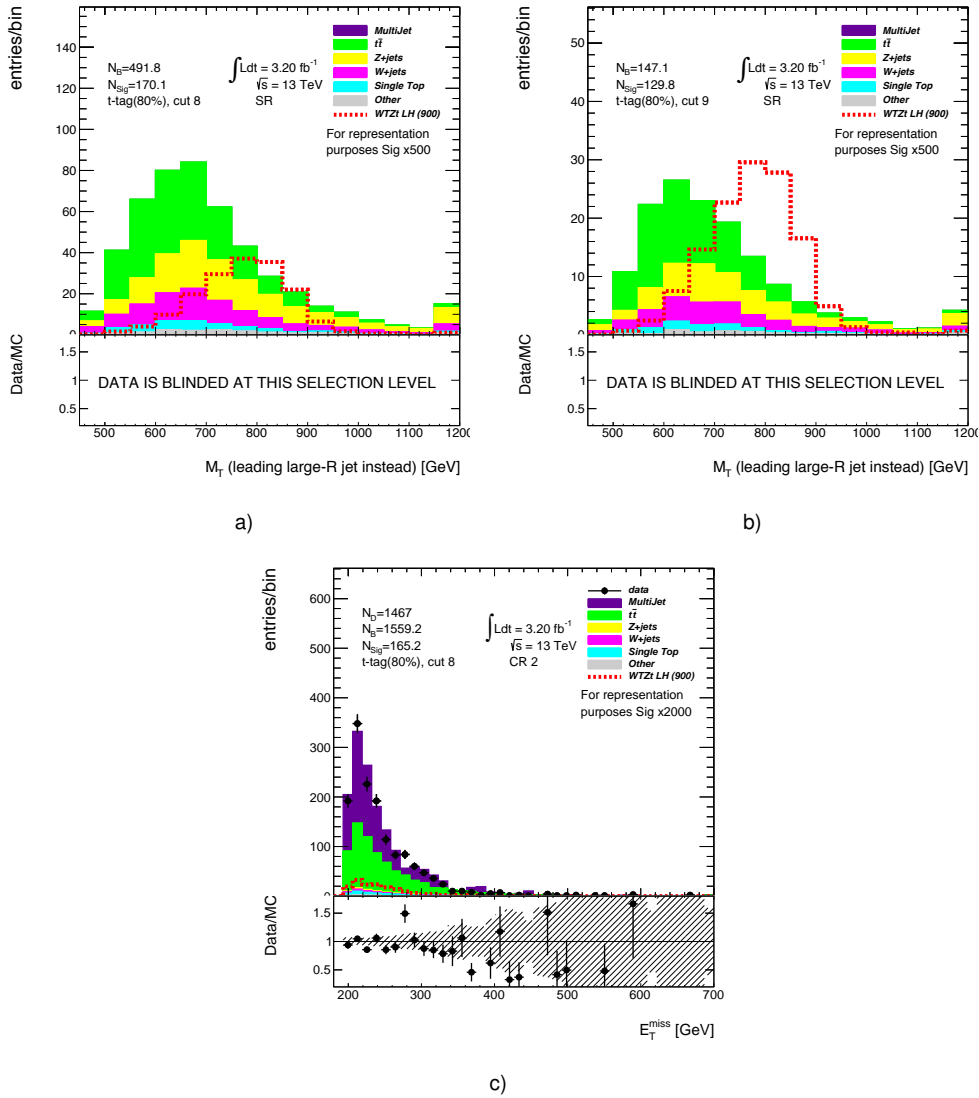
Figure 4.26: The distributions for the transverse mass in the two final signal regions, at a) and b). Also included the $\not{E}_T$ distribution for the $t\bar{t}$ control region, at c).

effect of a more stringent top-tagging resulting in lower statistics for signal itself. The single T limit in this case is 0.34 pb with bands $+2\sigma = 0.73$, $+1\sigma = 0.50$, $-1\sigma = 0.25$ and $-2\sigma = 0.18$, whereas the mono-top one is valued at 0.45 pb with bands $+2\sigma = 0.97$, $+1\sigma = 0.69$, $-1\sigma = 0.32$ and $-2\sigma = 0.24$.

And finally the last case scenario: with top-tagging operating at 50% efficiency and a minimum $\not{E}_T$ of 300 GeV can be found in 4.25b) and 4.25a). It provides the highest lower limits of the four distinct cases presented here, both before and after the forward jet request. The single T limit is valued at 0.34, with bands $+2\sigma = 0.73$, $+1\sigma = 0.50$,

$-1\sigma = 0.25$ and $-2\sigma = 0.18$. For mono-top proxy, the cross-section limit is set at 0.45 pb, $+2\sigma = 0.98$, $+1\sigma = 0.70$, $-1\sigma = 0.33$ and $-2\sigma = 0.24$.

We thus end up with two signal regions (one acting as a proxy for mono-top, the other for T) based on the most optimal requirements at Ω and $\Delta\phi(smallR\ jet\ closest\ \not{E}_T; \not{E}_T)$ with a minimum threshold of $\not{E}_T$ of 200 GeV and a top-tagging efficiency of 80%. The transverse mass for each proposed signal region can be pictured in figures 4.26a) and 4.26b). By inverting the two varying requirements of the single T signal region (in addition to the two b-tagged track jet requirement) one ends up with a $t\bar{t}$ control region. All regions are summarised in table 4.8. The proposed $t\bar{t}$ control region offers reasonable data/background agreement, but suffers from multijet contamination, as can be seen in figure 4.26c). A solution to this problem is still being investigated. Yield tables for the three regions can be found in tables 4.9 and 4.10.

Signal region I (80% top-tagging)	Yields $\sqrt{s} = 13$ TeV, $\int \mathcal{L}dt = 3.2$ fb^{-1}
WTZt LH (900)	0.34 ± 0.01
$t\bar{t}$	214.35 ± 4.57
MultiJet	0.00 ± 0.00
$Z + jets$	146.05 ± 2.09
$W + jets$	89.34 ± 1.69
Single Top	25.71 ± 0.94
Other	16.36 ± 0.88
Total bkg.	491.81 ± 5.45
Signal region II (80% top-tagging)	Yields $\sqrt{s} = 13$ TeV, $\int \mathcal{L}dt = 3.2$ fb^{-1}
WTZt LH (900)	0.26 ± 0.00
$t\bar{t}$	69.47 ± 2.59
MultiJet	0.00 ± 0.00
$Z + jets$	40.07 ± 1.27
$W + jets$	25.28 ± 0.83
Single Top	8.01 ± 0.53
Other	4.31 ± 0.42
Total bkg.	147.13 ± 3.08

Table 4.9: Yield tables for the last cut of each of the proposed signal regions (the first one is a proposal for a mono-top signal region, the second one for singly produced T).

$t\bar{t}$ control region (80% top-tagging)	Yields $\sqrt{s} = 13$ TeV, $\int \mathcal{L} = 3.2$ fb^{-1}
WTZt LH (900)	0.08 ± 0.00
$t\bar{t}$	677.23 ± 8.29
MultiJet	794.50 ± 41.81
$Z + jets$	15.82 ± 1.06
$W + jets$	22.32 ± 0.79
Single Top	37.89 ± 1.15
Other	11.48 ± 0.36
Total bkg.	1559.23 ± 42.66
data	1467

Table 4.10: Yield table for the last cut of the $t\bar{t}$ control region.

Chapter 5

Conclusion

A search for heavy top partners that decay into Z boson (which will, in turn, decay into a pair of neutrinos) and a hadronically decaying top quark, and for scalar resonances that decay into an invisible fermion and a hadronically decaying top quarks, was devised. This study was developed from scratch, in collaboration with Dortmund TU. Two signal regions were delineated: one for the single T model, and one for the mono-top resonant model. A control region enriched in $t\bar{t}$ processes was also drawn, wherein good agreement between data and simulated samples exists in certain variables. The $t\bar{t}$ control region suffers from multijet contamination. A solution is currently being investigated.

It is not yet possible to establish a comparison with existing resonant mono-top limits as prior analysis in ATLAS choose a mass for the scalar resonance S of 500 GeV, and then perform a limit setting for a range of f_{met} masses. For CMS, the resonant model hasn't been considered yet. Since we do not yet possess any simulated mono-top resonant signal, the single T signal without any forward jet cut applied is used to obtain a "proxy" limit, as there are no other significant kinematic differences between the two models.The proxy expected limit predicted by this analysis for mono-top resonant thus far is 0.44 pb. Meanwhile, the production of mono-top resonant samples is, at the time of writing, ongoing, and in the near future a limit for these samples will be derived.

On the ATLAS side, during run-1, at $\sqrt{s} = 8$ TeV, for singly-produced T of mass 900 GeV decaying into Zt, clocks in at $\sigma[pb] \times BR(T \rightarrow Zt) = 0.18$ pb (see figure 5.1a)), which, if divided by the branching ratio for the Zt decay (at the limit of high masses, BR ratios for the $SU(2)$ T singlet decays obey the following relationship: 2:1:1, bW:tZ:tH, unless otherwise explicitly stated) yields a lowest upper limit of $0.18/0.25$ pb $= 0.72$ pb [41].

When it comes to a limit obtained with 2015 data, one could look at some of the

m_T [GeV]	$\sigma(pp \to Tbq) \times BR(T \to Zt)$ [fb]	
	Exp. Limit (95% CL)	Obs. Limit (95% CL)
400	1110	830
450	610	515
500	475	425
550	475	365
600	380	310
650	275	205
700	295	190
750	235	155
800	220	155
850	210	140
900	180	125
950	200	125
1000	155	95
1050	145	90

Mass	Obs.	Expected				
[TeV]		-2σ	-1σ	nom.	$+1\sigma$	$+2\sigma$
0.4	5.75	1.87	2.46	3.84	6.86	16.09
0.5	0.89	0.47	0.67	1.00	1.61	2.72
0.6	0.38	0.20	0.29	0.39	0.58	0.86
0.7	0.22	0.13	0.18	0.26	0.39	0.58
0.8	0.23	0.10	0.17	0.23	0.31	0.42
0.9	0.18	0.07	0.09	0.13	0.21	0.34
1.0	0.19	0.05	0.07	0.11	0.17	0.28
1.1	0.19	0.05	0.07	0.10	0.17	0.26
1.2	0.12	0.04	0.05	0.08	0.13	0.24

a) b)

Figure 5.1: Tables from the analysis showcasing the expected and observed upper limits at each mass point, either considering the Zt decay (left-hand side) or the Wb decay (right-hand side) from two distinct $\sqrt{s} = 8$ TeV ATLAS searches. On the right-hand side not only expected limits are present, but also the side-bands at $\pm 1\sigma$ and $\pm 2\sigma$. Taken from [41] and [42], respectively.

results put out by CMS at $\sqrt{s} = 13$ TeV. In the analysis which highlights the decay $T \to Zt$ [48], the expected limit is around $0.6/0.25 = 2.4$ pb (again, since the cited paper assumes the small coupling approximation, the BR's tend to 2:1:1, bW:tZ:tH, which is why the limit is divided by 0.25) as can be seen from 5.1b).

No comparison in terms of coupling parameters and mixing angles is done, as that would require translating parameters to and fro different models (plus no mass scan is yet performed). As such only a comparison based on the experimental variable (the cross-section) is performed. The preliminary exclusion limit obtained in this thesis (0.32 pb for a BR of 100% for the decay $T \to tZ$) is less stringent than the previously mentioned $\sqrt{s} = 13$ TeV expected limits from CMS. However, our limit is bound to change in the near future, as development of the multijet estimate is ongoing.

Several things are still to be done, such as completing work in the multijet estimate, devising a control region rich in multijet, diminishing multijet's role in the $t\bar{t}$ control region, taking a look at statistical and systematic uncertainties, optimizing binning for limit setting, obtaining an observed limit (this requires eventual unblinding, which can only occur after approval from the ATLAS collaboration), and thus claim either exclusion or discovery. It would also be interesting to explore what can be gained (in terms of limits) by moving from a cut-based analysis into a multivariate one. It is of major interest to repeat this analysis with 2016 data (higher total integrated luminosity).

Bibliography

[1] S. L. Glashow. Partial symmetries of weak interactions. *Nucl. Phys. 22 (1961), 579-588*, 1961.

[2] Y. Nambu M. Y. Han. Three-triplet with double SU(3) symmetry. *Phys. Rev. 139, B1006*, 1965.

[3] O. W. Greenberg. Spin and unitary-spin independence in a paraquark model of baryons and mesons. *Phys. Rev. Lett. 13, 598*, 1964.

[4] F. Wilczek D. Gross. Ultraviolet behavior of non-abelian gauge theories. *Phys. Rev. Lett. 30, 1343*, 1973.

[5] H. D. Politzer. Reliable perturbative results for strong interactions. *Phys. Rev. Lett. 30, 1346*, 1973.

[6] P. W. Higgs. Broken symmetries and the masses of gauge bosons. *Phy. Rev. Lett. 13, 321-323*, (1964).

[7] T. W. B. Kibble G. S. Guralnik, C. R. Hagen. Global conservation laws and massless particles. *Phys. Rev. Lett. 13, 585-587*, 1964.

[8] R. Brout F. Englert. Broken symmetries and the mass of gauge vector mesons. *Phys. Rev. Lett. 13, 321-323*, 1964.

[9] S. Weinberg. A model of leptons. *Phys. Rev. Lett. 19, 1264-1266*, 1967.

[10] J. Goldstone. Field theories with "superconductor" solutions. *Il Nuovo Cimento, 19, 154*, 1961.

[11] CDF Collaboration. Observation of top quark production $p\bar{p}$ collisions with the collider detector at fermilab. *Phys. Rev. Lett. 74, 2626*, 1995.

[12] DØ Collaboration. Search for high mass top quark production on $p\bar{p}$ collision at $\sqrt{s} = 1.8$ TeV. *Phys. Rev. Lett. 74, 2422*, 1995.

[13] DONUT Collaboration. Observation of tau neutrino intercations. *Phys.Lett.B504:218-224,2001*, 2000.

[14] CMS Collaboration ATLAS Collaboration. Combined measurement of the higgs boson mass in $p\bar{p}$ collisions at $\sqrt{s}$=7 and 8 TeV with the ATLAS and CMS experiments. *Phys. Rev. Lett. 114, 191803*, 2015.

[15] D. Binosi L. Theußl. Jaxodraw. http://jaxodraw.sourceforge.net.

[16] M. J. Bowick F. del Aguila. The possibility of new fermions with $\delta I = 0$ mass. *Nucl. Phys. B224 107*, 1983.

[17] J. Santiago F. del Aguila, M. Perez-Victoria. Effective description of quark mixing. *Phys. Lett. B492 98*, 1983.

[18] M. Perez-Victoria F. del Aguila and J. Santiago. Observable contributions of new exotic quarks to quark mixing. *JHEP 09 011*, 2000.

[19] J. A. Aguilar-Saavedra, R. Benbrik, S. Heinemeyer, and M. Perez-Victoria. A handbook of vector-like quarks. mixing and single production. *Phys. Rev. D 88, 094010 (2013)*, 2013.

[20] M. Bruchkremer, G. Cacciapaglia, and L. Panizzi A. Deandrea. Model independent framework for searches of top partners. *CP3-13-22, LYCEN 2013-03, SHEP-13-10*, 2013.

[21] B. Bellazzini, C. Csáki, and J. Serra. Composite higgses. *10.1140/epjc/s10052-014-2766-x*, 2014.

[22] P. Lodone. Vector-like quarks in a composite higgs model. *JHEP 0812:029,2008*, 2008.

[23] Arkani-Hamed N., Cohen A. G., Katz E., and Nelson A. The littlest higgs. *JHEP 0207 (2002) 034*, 2002.

[24] Han T., Logan E., and McElrath B. Wang L. Phenomenology of the little higgs model. *Phys. Rev. D 67, 095004*, 2003.

[25] S. P. Martin and J. D. Wells. Implications of gauge-mediated supersymmetry with vector-like quarks and a 125 GeV higgs boson. *CERN-TH-2012-147*, 2012.

[26] L. Maiani S. Glashow, J. Iliopoulos. Weak interactions with lepton-hadron symmetry. *Phys. Rev. D 2, 1285*, 1970.

[27] M. Cooke. Private comunication.

[28] J. A. Aguilar-Saavedra. Protos. http://jaguilar.web.cern.ch/jaguilar/protos/.

[29] ATLAS Collaboration. Search for production of vector-like quark pairs of four top quarks in the lepton-plus-jets final state in pp collisions at $\sqrt{s} = 8$ TeV with the ATLAS detector. *JHEP 08 105*, 2015.

[30] M. Backovic, T. Flacke, J. Kim, and S. Lee. Search strategies for TeV scale fermionic top partners with charge 2/3. *CP3-15-21*, 2015.

[31] Fabio Maltoni Jeremy Andrea, Benjamin Fuks. Monotops at the lhc. *Phys. Rev. D 84, 074025*, 2011.

[32] I. Boucheneb, G. Cacciapaglia, A. Deandrea, and B. Fuks. Revisiting monotop production at the LHC. *JHEP01 (2015) 017*, 2015.

[33] ATLAS Collaboration. Search for invisible particles produced in association with single-top quarks in proton-proton collisions at $\sqrt{s} = 8$ TeV with the atlas detector. *Eur. Phys. J. C (2015) 75:79*, 2015.

[34] R. Barbier, C. Berat, M. Besancon, M. Chemtob, and A. Deandrea et al. R-parity violating supersymmetry. *Phys. Respt. 420 (2005) 1-202*, 2005.

[35] S. Barr. A new symmetry breaking pattern for SO(10) and proton decay. *Phys. Lett. B112 no. 3 (1982) 219-22*, 1982.

[36] S. V. Demidov, D. S. Gorbunov, and D. V. Kirpichnikov. Collider signatures of hylogenesis. *Phys. Rev. D 91, 035005 (2015)*, 2015.

[37] B. C. Allanach, S. Grab, and H. E. Harber. Supersymmetric monojets at the Large Hadron Collider. *JHEP 1101 (2011) 138*, 2011.

[38] A. Kumar, J. N. Ng, A. Spray, and P. T. Winslow. Tracking down the top quark forward-backward asymmetry with monotops. *Phys. Rev. D 88, 075012 (2013)*, 2013.

[39] F. del Aguila and J. A. Aguilar-Saavedra L. Ametller. Zt and gamma t production via top flavour changing neutral couplings at the Fermilab Tevatron. *Phys.Lett. B462 (1999) 310–318*, 1999.

FCUP | 92
Search for top quarks accompanied by missing energy in
hadronic topologies at the ATLAS experiment

[40] ATLAS Collaboration. Exotics public results. https://twiki.cern.ch/twiki/bin/view/AtlasPublic/ExoticsPublicResults.

[41] ATLAS Collaboration. Search for pair and single production of new heavy quarks that decay to a Z boson and a third-generation quark in pp collisions at $\sqrt{s} = 8$ TeV with the ATLAS detector. *JHEP 11 (2014) 104*, 2014.

[42] ATLAS Collaboration. Search for single production of vector-like quarks decaying into Wb in pp collisions at $\sqrt{s} = 8$ TeV with the ATLAS detector. *CERN-PH-EP-2015-319*, 2016.

[43] ATLAS Collaboration. Search for single production of a vector-like quark via a heavy gluon in the $4b$ final state with the ATLAS detector in pp collisions at $\sqrt{s} = 8$ TeV. *CERN-PH-EP-2015-321*, 2016.

[44] ATLAS Collaboration. Search for the production of single vector-like and excited quarks in the Wt final state in pp collisions at $\sqrt{s} = 8$ TeV with the ATLAS detector. *JHEP02(2016)110*, 2016.

[45] CMS Collaboration. CMS Beyond 2 Generation Public Results. https://twiki.cern.ch/twiki/bin/view/CMSPublic/PhysicsResultsB2G.

[46] CMS Collaboration. Search for vector-like charge 2/3 T quarks in proton-proton collisions at $\sqrt{s} = 8t$ TeV. *Phys. Rev. D 93 012003*, 2016.

[47] CMS Collaboration. Search for pair-produced vectorlike B quarks in proton-proton collisions at $\sqrt{s} = 8$ TeV. *Phys. Rev. D 93, 112009*, 2016.

[48] CMS Collaboration. Search for single production of vector-like quarks decaying into final states with a Z boson and a top or a bottom quark. CMS-PAS-B2G-16-001.

[49] CMS Collaboration. Search for singly-produced vector-like quarks decaying into a W boson and a bottom quark using the single lepton final state. CMS PAS B2G-16-006.

[50] CMS Collaboration. Search for monotop signatures in proton-proton collisions at $\sqrt{s} = 8$ TeV. *Phys. Rev. Lett. 114, 101801*, 2015.

[51] CMS Collaboration. Search for dark matter in association with a boosted top quark in the all hadronic final state. CMS-PAS-EXO-16-017.

[52] ATLAS Collaboration. ATLAS Luminosity Public Results.
https://twiki.cern.ch/twiki/bin/view/AtlasPublic/LuminosityPublicResultsRun2.

[53] ATLAS Collaboration. ATLAS insertable b-layer technical design report. Technical
report, CERN, 2010.

[54] International Masterclasses. Atlas detector. https://kjende.web.cern.ch/kjende/en/atlas.htm.

[55] The ATLAS Collaboration. The ATLAS Experiment at the CERN Large Hadron
Collider. *Journal of Instrumentation*, 3(08):S08003, 2008.

[56] Moritz Backes, editor. *The ATLAS Trigger System - Ready for Run-2*. CERN, ATL-
DAQ-PROC-2015-041, 2015.

[57] Arantxa Ruiz Martínez, editor. *The Run-2 ATLAS Trigger System*. CERN, ATL-
DAQ-PROC-2016-003, 2016.

[58] ATLAS Collaboration. ATLAS level-1 trigger: Technical design report. ATLAS-
TDR-12, CERN, 1998.

[59] ATLAS Collaboration. ATLAS High-Level Trigger, Data Acquisition and Controls.
ATLAS-TDR-016, CERN, 2002.

[60] WLCG Data Transfers and Activities (WDT) Project. Worldwide LHC Computing
Grid. http://wlcg.web.cern.ch.

[61] The LCG Editorial Board. LHC computing grid: Technical design report. Technical
report, CERN, 2005.

[62] G. Soyez M. Cacciari, G. Salam. The anti-kt clustering algorithm. *JHEP
0804:063,2008*, 2008.

[63] L. Wang D. Krohn, J. Thaler. Jet trimming. *JHEP 1002:084,2010*, 2009.

[64] ATLAS Collaboration. Electron efficiency measurements with the ATLAS detector
using the 2015 LHC proton-proton collision data. *ATLAS-CONF-2016-024*, 2016.

[65] ATLAS Collaboration. Muon reconstruction performance of the ATLAS detector in
proton-proton collision data at $\sqrt{s} = 13$ TeV. *Eur. Phys. J. C (2016) 76:292*, 2016.

[66] ATLAS Collaboration. Missing energy trigger public results.
https://twiki.cern.ch/twiki/bin/view/AtlasPublic/MissingEtTriggerPublicResults.

FCUP | 94
Search for top quarks accompanied by missing energy in
hadronic topologies at the ATLAS experiment

[67] K.Hamilton et al. S. Alioli. Powheg-box. http://powhegbox.mib.infn.it.

[68] T. Sjöstrand et al. Pythia. http://home.thep.lu.se/ torbjorn/Pythia.html.

[69] S. Hoeche et al. Sherpa. https://sherpa.hepforge.org/trac/wiki.

[70] J. Alwall et al. Madgraph. https://launchpad.net/mg5amcnlo.

[71] J. Belm et al. Herwig event generator. https://herwig.hepforge.org.

[72] ATLAS Collaboration. Flavor tagging with track jets in boosted topologies with the ATLAS detector. *ATL-PHYS-PUB-2014-013*, 2014.

[73] ATLAS Collaboration. Expected performance of the ATLAS b-tagging algorithms in Run-2. *ATL-PHYS-PUB-2015-022*, 2016.

[74] ATLAS Collaboration. Boosted hadronic top identification at ATLAS for early 13 TeV data. *ATL-PHYS-PUB-2015-053*, 2015.

[75] ATLAS Collaboration. Identification of high transverse momentum top quarks in pp collisions at $s = 8$ TeV with the ATLAS detector. *JHEP 06 093*, 2016.